Applications of Adjoint Modelling in Chemical Composition: Studies of Tropospheric Ozone at Middle and High Northern Latitudes

by

Thomas William Walker

A thesis submitted in conformity with the requirements
for the degree of Doctor of Philosophy
Graduate Department of Physics
University of Toronto

Abstract

Applications of Adjoint Modelling in Chemical Composition: Studies of Tropospheric Ozone at Middle and High Northern Latitudes

Thomas William Walker

Doctor of Philosophy

Graduate Department of Physics

University of Toronto

2014

Ozone is integral to tropospheric chemistry, and understanding the processes controlling its distribution is important in climate and air pollution contexts. The GEOS-Chem global chemical transport model and its adjoint are used to interpret the impacts of midlatitude precursor emissions and atmospheric transport on the tropospheric ozone distribution at middle and high northern latitudes.

In the Arctic, the model reproduces seasonal cycles of peroxyacetyl nitrate (PAN) and ozone measured at the surface, and observed ozone abundances in the summer free troposphere. Source attribution analysis suggests that local photochemical production, ≤ 0.25 ppbv/day, driven by PAN decomposition, accounts for more than 50% of ozone in the summertime Arctic boundary layer. In the mid-troposphere, photochemical production accounts for 30–40% of ozone, while ozone transported from midlatitudes contributes 25–35%. Adjoint sensitivity studies link summertime ozone production to anthropogenic, biomass burning, soil, and lightning emissions between 50°N–70°N. Over Alert, Nunavut, the sensitivity of mid-tropospheric ozone to lightning emissions sometimes exceeds that to anthropogenic emissions.

Over the eastern U.S., numerous models overestimate ozone in the summertime boundary layer. An inversion analysis, using the GEOS-Chem four-dimensional variational data assimilation system, optimizes emissions of NO_x and isoprene. Inversion

results suggest the model bias cannot be explained by discrepancies in these precursor emissions. A separate inversion optimizes rates of key chemical reactions including ozone deposition rates, which are parameterized and particularly uncertain. The inversion suggests a factor of 2–3 increase in deposition rates in the northeastern U.S., decreasing the ozone bias from 17.5 ppbv to 6.0 ppbv. This analysis, however, is sensitive to the model boundary layer mixing scheme.

Several inversion analyses are conducted to estimate lightning NO_x emissions over North America in August 2006, using ozonesonde data. The high-resolution nested version of GEOS-Chem is used to better capture variability in the ozonesonde data. The analyses suggest North American lightning NO_x totals between 0.076–0.204 Tg N. A major challenge is that the vertical distribution of the lightning source is not optimized, but the results suggest a bias in the vertical distribution. Reliably optimizing the three-dimensional distribution of lightning NO_x emissions requires more information than the ozonesonde dataset contains.

Acknowledgements

The completion of this doctoral thesis, while a single name appears on the cover, represents the culmination of years of effort and support from a great number of individuals and agencies. In particular, the author is thankful for the guidance and support of his supervisor, Dylan. The author is also greatly indebted to his wife Val, who was always there to offer gentle support. Thanks go out to current and former members of the Atmospheric Physics and Composition Modelling Group at the University of Toronto, whose helpful feedback and discussions helped form salient portions of this work. Research collaborators from various other institutions also deserve thanks for sharing their data, code, and expertise.

This work was supported by funding from the Natural Sciences and Engineering Research Council of Canada, the Ontario Graduate Scholarship program, the Walter C. Sumner Foundation, and the Canadian Foundation for Climate and Atmospheric Sciences. Support from the Centre for Global Change Science at the University of Toronto supported the author's participation in field work during the ARCIONS campaign.

The author recognizes the support of the numerous agencies worldwide who contribute to the World Ozone and Ultraviolet Radiation Data Centre (WOUDC). Ozonesonde data not included in the IONS-06 campaign were retrieved from the WOUDC archive at http://www.woudc.org/.

The author also acknowledges the strong support of the European Commission, Airbus, and the Airlines (Lufthansa, Austrian, and Air France) who have carried the MOZAIC equipment free of charge and have performed the maintenance since 1994. MOZAIC is presently funded by INSU-CNRS (France), Meteo-France, and Forschungszentrum (FZJ, Julich, Germany). The MOZAIC database is supported by ETHER (CNES and INSU-CNRS).

Finally, the author thanks the Canadian Space Agency for permitting the publication of intellectual property pertaining to the SOAR concept study.

Contents

List of Tables

List of Figures

Chapter 1

Introduction

1.1 Ozone as an Air Pollutant and a Greenhouse Gas

Ozone near the surface is a harmful air pollutant which affects human health in both acute [*Thurston and Ito*, 2001] and chronic doses [*Jerrett et al.*, 2009], and also has adverse effects on vegetation [*Krupa and Manning*, 1988]. Despite efforts in industrialized nations to reduce emissions of the gases that form ozone, many people live in locations where surface ozone concentrations exceed recommended levels [*U.S. Environmental Protection Agency*, 2012]. The complexity of the chemical and physical processes that contribute to ozone formation and transport in the atmosphere complicate pollution reduction through emissions controls [*Hakami et al.*, 2006].

In addition to its role in air quality, ozone is intricately related to the climate system. Ozone is the third most important greenhouse gas in terms of the change in radiative forcing since the preindustrial epoch [*Solomon et al.*, 2007]. Figure 1.1 shows the change in simulated tropospheric ozone abundance since the preindustrial epoch and the consequent change in radiative forcing as calculated by *Mickley et al.* [2004]. They estimated that there have been significant changes in ozone, and consequently radiative forcing, in the northern extratropics since the preindustrial as a result of fossil fuel emissions. There

have also been smaller changes in radiative forcing in the tropics as a result of biomass burning. *Mickley et al.* [2004] estimated a particularly large change in ozone radiative forcing in the Arctic in summer as a result of the effects of shortwave forcing over ice in the region. Climate change also feeds back on ozone concentrations, as warmer temperatures lead to higher biogenic emissions and greater ozone production [*Katragkou et al.*, 2011]. Climate-induced changes in the frequency and duration of stagnant high-pressure systems that favour enhanced ozone production are another potential reason that ozone concentrations at the surface are projected to increase under warmer future climate conditions [*Hauglustaine et al.*, 2005; *Weaver et al.*, 2009]. Increases in surface ozone in future climate regimes could lead to amplified health hazards for humans [*Bell et al.*, 2007; *West et al.*, 2007] and damage to vegetation [*Ashmore*, 2005].

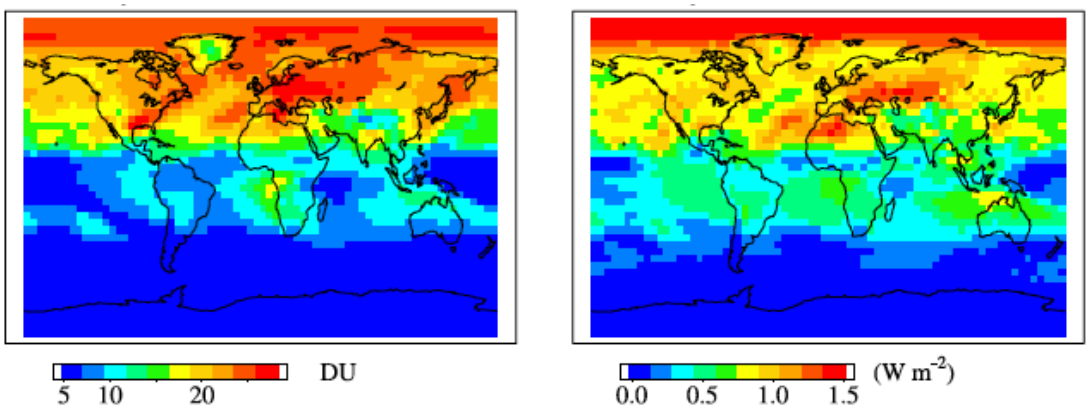

Figure 1.1: Estimated change in column abundance of tropospheric ozone averaged from June–August since preindustrial times (left), in Dobson Units, and the consequent change in instantaneous radiative forcing at the tropopause (right), in W/m^2. Figure from *Mickley et al.* [2004].

Ozone concentrations typically increase monotonically with altitude in the troposphere and peak in the stratosphere, where the majority of the ozone resides. This configuration led early researchers to the view that much of the ozone in the troposphere

originated in the stratosphere, and was transported down into the troposphere. Work in the 1970's (*Crutzen* [1979], and references therein) altered this paradigm, arguing that chemical production and loss in the troposphere exceed the stratospheric influx, and so are critical to the proper understanding of ozone as a pollutant. It is currently estimated that the stratospheric input of ozone represents about 10% of the total source of tropospheric ozone, with in situ chemical production being the dominant source.

Owing to the balance of in situ chemical production and loss, the tropospheric ozone distribution displays inhomogeneity in both time and space. Further, the ozone distribution is subject to variations in precursor emissions, atmospheric transport, and the oxidative capacity of the troposphere. A better understanding of the processes contributing to changes and trends in tropospheric ozone is needed to mitigate this pollutant's effects under both current and future climate regimes. Table 1.1 demonstrates the large spread in global mean estimates of the effects of chemistry and dry deposition on ozone. The net chemical production, which represents the balance of a large source and a large sink, varies by more than a factor of four across models. Similarly, the global mean loss of ozone by dry deposition to the surface varies by a factor of two. In this context, improvements in the representation in models of the processes controlling tropospheric ozone are critical.

Figure 1.2 shows the degree of uncertainty possible in an individual model's ability to capture the distribution of tropospheric ozone, with an underestimate of 30% in the free troposphere in the unconstrained model, and an overestimate of the same magnitude near the surface. The large ozone underestimate in the midlatitude free troposphere in Figure 1.2 is believed to be caused by the model's distribution of lightning emissions [*Parrington et al.*, 2008]. This figure brings together a number of the key concepts that are addressed in this thesis. The analysis in Chapter 4 focuses on better estimating the sink of surface ozone associated with dry deposition to reduce the model bias in surface ozone. Chapter 5 attempts to constrain the distribution of lightning NO_x emissions over

North America using ozonesonde measurements in a high-resolution inversion. The impact of these midlatitude processes (such as lightning NO_x) and anthropogenic precursor emissions on tropospheric ozone in the Arctic is also examined, in Chapter 3.

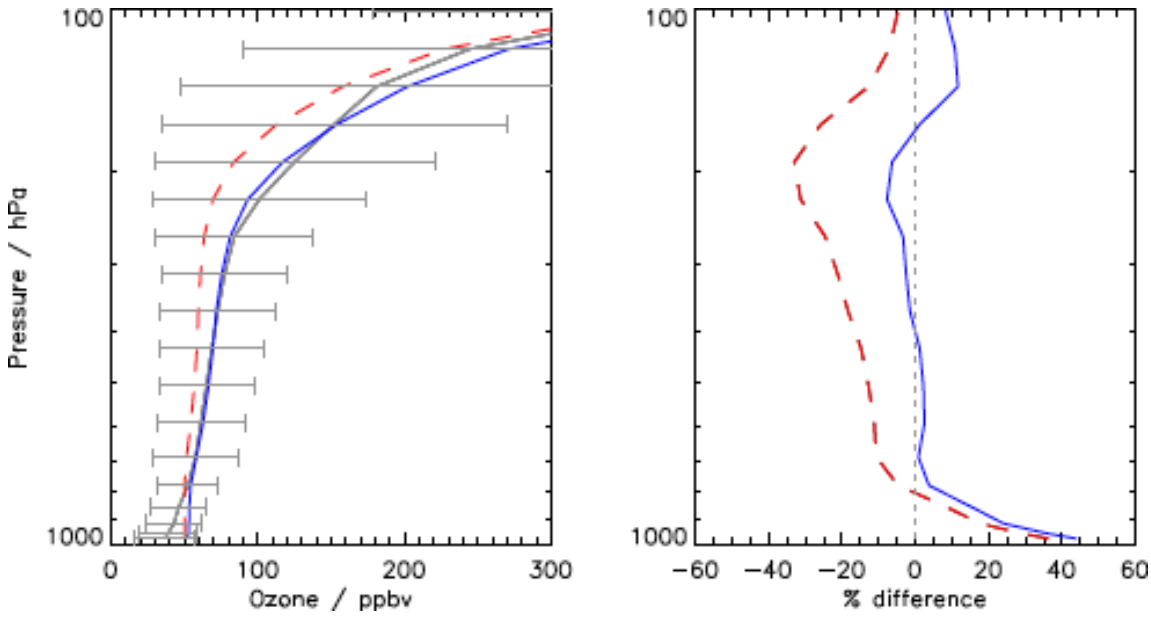

Figure 1.2: Comparison of mean ozone profiles over North America from the GEOS-Chem model with (blue solid line) and without (red dashed line) assimilation of Tropospheric Emissions Spectrometer (TES) ozone data. Model values are compared to the mean ozonesonde measurements from the 2006 INTEX Ozonesonde Network Study (IONS-06) campaign (thick grey solid line) with their standard deviations. The percentage differences (model − ozonesonde) with respect to the ozonesonde data are shown on the right. Figure adapted from *Parrington et al.* [2008].

Table 1.1: Global budgets of tropospheric ozone (in Tg/yr). Shown are simulation results for stratosphere-troposphere exchange (STE), the balance of chemical production and loss (Ch. P-L), and dry deposition to the surface (Dry Dep.). The total tropospheric burden of O_3 in Tg as well as its mean lifetime in days are also shown. The abbreviation NR indicates a result that was not reported. Adapted from *Solomon et al.* [2007].

Model	STE	Ch. P-L	Dry Dep.	Burden [Tg]	Lifetime [d]
TM3[a]	+570	+140	−710	350	33
GEOS-Chem[b]	+470	+600	−1070	320	22
CHASER[c]	+593	+397	−990	322	25
MOZART-2[d]	+340	+510	−860	360	23
MATCH-MPIC[e]	+540	+270	−820	290	21
GISS[f]	+417	NR	−1470	349	NR
LMDz-INCA[g]	+523	+568	−1090	296	28
UMD-CTM[h]	+480	NR	−1290	340	NR
IMPACT[i]	+660	NR	−830	NR	NR
SUNY/UiO GCCM[j]	+600	NR	−1100	376	NR
STOCHEM[k]	+395	+560	−950	273	19
FRSGC/UCI[l]	+520	+240	−760	283	22
LMDz-INCA[m]	+715	+546	−1261	303	28

[a] *Lelieveld and Dentener* [2000]

[b] *Bey et al.* [2001]

[c] *Sudo et al.* [2002]

[d] *Horowitz et al.* [2003]

[e] *Von Kuhlmann et al.* [2003]

[f] *Shindell et al.* [2003]

[g] *Hauglustaine et al.* [2004]

[h] *Park et al.* [2004]

[i] *Rotman et al.* [2004]

[j] *Wang et al.* [2004]

[k] *Stevenson et al.* [2004]

[l] *Wild et al.* [2004]

[m] *Folberth et al.* [2006]

1.2 Chemistry of Ozone Formation and Removal in the Troposphere

The abundance of ozone (O_3) in the troposphere is governed by a balance between chemical production and loss, inputs from the stratosphere, and losses at the surface. These terms are roughly balanced at the global scale, but regional differences can cause significant variation in tropospheric ozone concentrations. In situ photochemical production and loss represent the largest terms in the overall budget, although they largely offset one another on the global scale [*Lelieveld and Dentener*, 2000].

Ozone is produced during the oxidation of volatile organic compounds (VOCs) in the presence of nitrogen oxides (NO_x=NO+NO_2) [*Crutzen*, 1979]. For a general organic radical R (which could be, for instance, H or CH_3), oxidation is initiated by the reaction with OH, resulting in the production of a peroxy radical (RO_2):

$$RH + OH \longrightarrow R + H_2O \quad \text{(R 1.1)}$$

$$R + O_2 + M \longrightarrow RO_2 + M \cdot \quad \text{(R 1.2)}$$

The peroxy radical reacts with other radical species in the atmosphere. Reaction with other peroxy radicals produces a peroxide (ROOH). Most peroxides will readily dissolve in water and can be removed from the atmosphere in that manner, or they can photolyze and regenerate OH and a carbonyl compound (R$^{'}$CHO; the prime designates that this functional group may differ from the previously-used R). This sequence of reactions does not produce ozone. For example, reaction with the perhydroxyl radical (HO_2) leads to:

$$RO_2 + HO_2 \longrightarrow ROOH + O_2 \quad \text{(R 1.3)}$$

$$ROOH + h\nu \longrightarrow RO + OH \quad \text{(R 1.4)}$$

$$RO + O_2 \longrightarrow R^{'}CHO + HO_2 \cdot \quad \text{(R 1.5)}$$

However, in the presence of NO_x an alternate oxidation pathway is possible:

$$RO_2 + NO \longrightarrow RO + NO_2 \qquad (R\,1.6)$$

$$NO_2 + h\nu \xrightarrow{O_2} NO + O_3\,. \qquad (R\,1.7)$$

The RO radical is subsequently oxidized into a carbonyl compound by Reaction R 1.5. Ozone is produced when NO_2 is photolyzed and converted back into NO. It happens that Reaction R 1.6, and in particular the reaction of NO with HO_2,

$$HO_2 + NO \longrightarrow OH + NO_2, \qquad (R\,1.8)$$

is very efficient, so that the presence of a small amount of NO_x is sufficient to trigger this ozone production pathway [*Crutzen*, 1979]. Furthermore, the ozone-producing cycle of R 1.6, R 1.5, R 1.8, R 1.1, and R 1.2 together with photolysis of NO_2 (R 1.7) does not consume NO_x, as is shown schematically in Figure 1.3. Given a supply of VOCs, ozone production is catalyzed by NO_x.

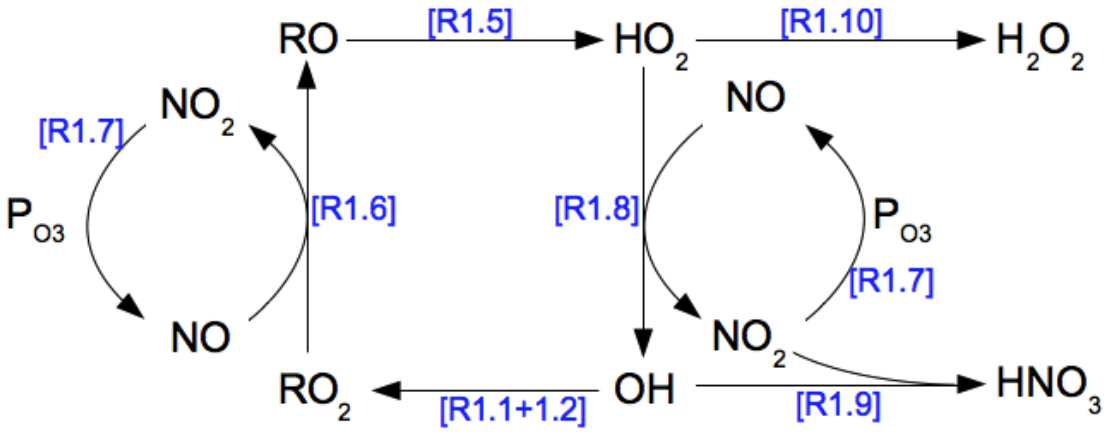

Figure 1.3: Reactions governing ozone production in the troposphere. P_{O_3} indicates production of ozone. Modified from *Jacob* [1999].

The catalytic cycle of ozone production terminates with the consumption of HO_x and NO_x radicals, for example:

$$NO_2 + OH + M \longrightarrow HNO_3 + M \quad \text{(R 1.9)}$$

$$HO_2 + HO_2 \longrightarrow H_2O_2 + O_2 \cdot \quad \text{(R 1.10)}$$

A more thorough discussion of nitric acid and other chemical reservoirs of NO_x appears in Chapter 3. The rate-limiting step in the cycle described above arises from competition for the NO radical between peroxy radicals (R 1.6 and R 1.8) and ozone,

$$O_3 + NO \longrightarrow NO_2 + O_2, \quad \text{(R 1.11)}$$

the latter of which, together with R 1.7, has no net effect. Ozone production can be expressed as

$$P_{O_3} = k_{R\,1.6}[RO_2][NO] + k_{R\,1.8}[HO_2][NO] = 2k_{R\,1.8}[HO_2][NO], \quad (1.1)$$

where efficient propagation through the reaction cycle R 1.6, R 1.5, R 1.8, R 1.1, and R 1.2 is assumed, such that $k_{R\,1.6}[RO_2][NO] \approx k_{R\,1.8}[HO_2][NO]$. There is rapid cycling between HO_2 and OH, so if we define the HO_x family (HO_x=HO_2+OH), the production of HO_x can be expressed as the sum of the two termination reactions [*Jacob*, 1999]:

$$P_{HO_x} = k_{R\,1.9}[NO_2][OH][M] + k_{R\,1.10}[HO_2]^2. \quad (1.2)$$

Depending on the availability of NO_x, one or the other termination reaction will dominate. In a regime with plenty of NO_x, as is the case in most urban environments, Reaction R 1.9 will dominate and the ozone production rate can be expressed:

$$P_{O_3} = \frac{2k_{R\,1.1}P_{HO_x}[RH]}{k_{R\,1.9}[NO_2][M]}. \quad (1.3)$$

If NO_x is not as readily available, as occurs in much of the remote atmosphere, Reaction R 1.9 will proceed slowly, Reaction R 1.10 will dominate the termination of the oxidation cycle, and the ozone production rate can be written as:

$$P_{O_3} = 2k_{R\,1.8}\left(\frac{P_{HO_x}}{k_{R\,1.10}}\right)^{1/2}[NO]. \tag{1.4}$$

The photochemical production of ozone in the troposphere is inversely proportional to the amount of NO_2 in a high-NO_x regime, and directly proportional to the amount of NO in a low-NO_x regime. This complex dependence of ozone production on precursor availability requires a thorough knowledge of the distribution of emission, transport, and loss of these precursors.

1.2.1 Emissions of Gaseous Precursors

The production rate of ozone depends non-linearly on the availability of NO_x. Additionally, NO_x itself has a strong association with non-accidental mortality [*Brook et al.*, 2007]. Knowledge of the sources, distribution, and fate of NO_x in the troposphere is therefore of interest. NO_x is released during the combustion of fossil fuels or living biomass, as well as through natural processes such as lightning or microbial activity in soils. Table 1.2 shows global annual estimates for various NO_x emissions sources. Here, sources labelled "anthropogenic" include fossil fuel burning at the surface, while emissions from aircraft that are mainly in the upper troposphere are treated separately.

Anthropogenic sources of NO_x have resulted in about a five-fold increase in total emissions since pre-industrial times [*van Aardenne et al.*, 2001]. Consequently, there has been a significant increase in tropospheric ozone abundances due to anthropogenic NO_x emissions [*Lelieveld and Dentener*, 2000].

Volatile organic compounds are also needed for ozone production. VOCs are often emitted coincidentally with NO_x, as they are also produced by combustion. VOCs are

Table 1.2: Estimates of global annual NO_x sources.

Source	Emissions [Tg N/yr]	Reference
Aircraft	0.5	*Wang et al.* [1998]
Anthropogenic	90.6	*Olivier and Berdowski* [2001]
Biomass burning	9.9	*van der Werf et al.* [2010]
Biofuels	2.2	*Yevich and Logan* [2003]
Lightning	5	*Schumann and Huntrieser* [2007]
Soils	10.7	*Hudman et al.* [2012]

also released naturally by vegetation, which can drive ozone production even where combustion sources are small [*Guenther et al.*, 2006].

Anthropogenic Emissions

Reactive nitrogen oxides are produced by a wide range of human activities: fossil fuel combustion for power and transportation, and industrial processes such as steel sintering and cement mixing [*Zhang et al.*, 2007]. The amount of NO_x released to the atmosphere has increased drastically since the pre-industrial epoch, and considerable positive trends still exist over developing regions [*Richter et al.*, 2005]. Contrarily, developed regions where emissions controls have been implemented show negative trends in recent years [*U.S. Environmental Protection Agency*, 2012; *Tørseth et al.*, 2012].

Inventories of emissions from anthropogenic sources are compiled from detailed databases of fuel consumption on national, regional, or individual site scales. A typical approach is to scale the amount of fuel consumed by a particular activity by an emission factor specific to that activity, then aggregate these into a gridded product [*Olivier and Berdowski*, 2001; *Zhang et al.*, 2007]. A number of inventories are available at global [*Benkovitz et al.*, 1996; *Olivier and Berdowski*, 2001] and regional [*Vestreng and Klein*, 2002; *Streets et al.*, 2003, 2006; *Kuhns et al.*, 2005] scales.

Due to the relatively short lifetime of NO_x in the lower troposphere (on the order of a day), there exists a strong relationship between NO_x emissions at the surface and the nearby concentrations of NO_x [*Martin et al.*, 2003a]. Furthermore, the partitioning of NO_x between NO_2 and NO in the lower troposphere, where NO_x concentrations are highest, favours NO_2. These factors have allowed space-based observations of NO_2 columns to be used in the estimation of surface NO_x emissions [*Martin et al.*, 2002a, 2003a; *Richter et al.*, 2005; *Lin et al.*, 2010; *Wang et al.*, 2012].

Using fuel consumption statistics for estimating the emissions inventories (so-called "bottom-up" approach) requires considerable effort to compile, and the release of the statistics can lag behind actual conditions by a number of years, which can be a problem in regions of rapid change. Also, these inventories can have substantial uncertainty in the statistics and emission factors used in their derivation. The satellite-based approach ("top-down"), which employs atmospheric observations to infer emissions estimates, presents a different set of challenges. For example, NO_2 columns retrieved from space-based platforms must be validated, and despite advances in instrument resolution, the instrument has a finite pixel size that may be obscured by clouds or may contain significant inhomogeneity [*Boersma et al.*, 2009; *Lamsal et al.*, 2010]. Further, problems can arise if assumptions in the retrieval calculation are not satisfied in the situation in which the retrieved columns are being used. Uncertainties in the NO_x sinks in the model employed in the top-down inversion can accommodate a range of results for emissions [*Stavrakou et al.*, 2013]. In some cases, the calculated trends in anthropogenic NO_x emissions differ depending on whether a "bottom-up" or "top-down" method is used to calculate the emissions [*Zhang et al.*, 2007; *Konovalov et al.*, 2010].

Lightning NO_x Emissions

Lightning heats air rapidly, causing the dissociation of molecular nitrogen and oxygen in the lightning channel and subsequently the formation of NO [*Zel'dovich and Raizer*,

1967]. The creation of NO from lightning represents a significant source of reactive nitrogen to the upper troposphere, since most other NO_x emissions occur at the surface. Lightning emissions also represent one of the most uncertain NO_x sources, with global estimates in the range 5 ± 3 Tg N/yr [*Schumann and Huntrieser*, 2007], because of uncertainties in the spatial distribution of lightning flashes, and in the amount of NO_x released in each flash.

The global distribution of lightning NO_x emissions is difficult to ascertain due in part to the difficulty in predicting or observing the location of lightning flashes. The distribution of flashes can be observed from the ground by detecting the electromagnetic pulse produced by the lightning strokes, or by sensing the illumination from the flash from space. Employing the Optical Transient Detector (OTD) satellite instrument, *Christian et al.* [2003] constrained the global annual mean flash rate to 44 ± 5 s^{-1}. The uncertainty in the global annual mean rate is dominated by variation in the instrument's detection efficiency, but uncertainties due to undersampling become more significant on shorter temporal and spatial scales. Similarly, the detection efficiency of ground-based networks that detect the electromagnetic pulse is imperfect and may vary with location [*Lay et al.*, 2004; *Nag et al.*, 2011]. Both satellite and ground-based methods have difficulty distinguishing cloud-to-ground (CG) and intra-cloud (IC) flashes.

The vertical distribution of NO_x within a storm system is also a confounding factor in estimating the lightning source. Studies using cloud-resolving models have been used to produce estimates of the effective vertical distribution of emissions in storm outflow [*Pickering et al.*, 1998; *Ott et al.*, 2010]. The vertical distribution profiles resulting from a three-dimensional cloud-resolving model are an inverted C-shape with maximum injection in the middle troposphere, in contrast with earlier studies [*Ott et al.*, 2010]. However, further composition observations in the vicinity of thunderstorms are needed to provide conclusive validation of these profiles.

Using the global mean flash rate and mean total global lightning NO_x source cited above puts the amount of NO_x emitted per flash at roughly 250 mol N/flash. Studies of composition around individual active lightning storms [*DeCaria et al.*, 2005; *Ott et al.*, 2007; *Huntrieser et al.*, 2008, 2009, 2011] give a broad range of NO_x yields per flash, which are difficult to extrapolate globally. The yield from lightning flashes at midlatitudes may be underestimated in global models based on results from the INTEX-A aircraft campaign [*Cooper et al.*, 2007; *Hudman et al.*, 2007].

Observations of atmospheric composition from satellites have also been employed to help constrain the lightning NO_x source. *Martin et al.* [2007] and *Sauvage et al.* [2007] used observations of NO_2, ozone, and nitric acid from multiple sensors to estimate the lightning contribution to free tropospheric concentrations of these species in the tropics. These methods become more difficult to apply in regions where surface emissions are strong or where the instrument's sensitivity to the upper troposphere is weak.

Other NO_x Sources

NO_x is also emitted from soils and during biomass burning. While neither of these sources competes with emissions from fossil fuel combustion on the global mean scale, either can be regionally important. Biomass burning in particular exhibits strong variability in time and location. Soils constitute the dominant surface source of NO_x in some remote regions such as Africa's Sahel [*Jaeglé et al.*, 2005].

Soils emit various nitrogen-containing species including NO_x, generated by the action of nitrogen-fixing microbes [*Yienger and Levy*, 1995; *Wang et al.*, 1998]. The amount of NO_x emitted depends on a number of parameters — temperature, biome type, and precipitation history chief among them. Emissions may be enhanced by recent burning or by nitrogen fertilizer application, and they may be reduced by deposition to the overlying vegetative canopy. Soil NO_x emissions also exhibit a substantial pulse following rainfall [*Yienger and Levy*, 1995; *Hudman et al.*, 2012]. Emissions from soils have been

quantified using satellite observations of NO_2 columns [*Jaeglé et al.*, 2004, 2005; *Hudman et al.*, 2010].

Inventories of biomass burning emissions are compiled in a somewhat analogous way to bottom-up anthropogenic inventories. The amount of fuel is estimated based on statistics of plant mass and type, or from a vegetation model [*van der Werf et al.*, 2006, 2010]. Fire locations and area burned are estimated based on data either from national reporting agencies or from satellite observations of changes in the locations of hot spots in the infrared [*Giglio et al.*, 2006]. Finally, the amount of fuel burned over these fire locations is multiplied by an emissions factor for a number of chemical species of interest (as compiled by, for example, *Akagi et al.* [2011], or as calculated from satellite data by, for example, *Mebust et al.* [2011]) and modified for combustion completeness [*van der Werf et al.*, 2006].

Emissions of Volatile Organic Compounds

VOCs comprise a suite of hydrocarbons that exist as trace gases in the atmosphere. These provide the source of peroxy radicals that initiate NO_x-catalyzed ozone production (that is, Reaction R 1.6). VOCs are produced during combustion or volatilize directly from fuels, and emission inventories for anthropogenic and biomass sources are calculated in a similar manner to NO_x inventories [*Olivier and Berdowski*, 2001].

Emissions from living plant matter represent an additional source of VOCs. About half the mass flux emitted from biogenic sources is composed of isoprene and monoterpenes [*Guenther et al.*, 1995, 2006]. These compounds react readily with hydroxyl, ozone, and other radicals to produce a variety of oxygenated organic molecules [*Fan and Zhang*, 2004; *Paulot et al.*, 2012]. The emission of isoprene is of particular importance, and depends strongly on the plant species [*Simpson et al.*, 1999] and temperature [*Guenther et al.*, 1995].

Oxidation of biogenically emitted isoprene occurs rapidly, and high concentrations of the oxidized organic products accumulate in regions of high biogenic emissions. The oxidation chemistry of isoprene is an ongoing area of research, the details of which are beyond the scope of this discussion. However, it is notable that isoprene has a short lifetime in summer ($\sim$ 0.5 h), and that formaldehyde is among the first-generation products [*Millet et al.*, 2006]. Thus, measurements from space of formaldehyde have been employed as a constraint on isoprene emissions [*Palmer et al.*, 2003; *Millet et al.*, 2008]. These constraints are still subject to significant uncertainties.

1.2.2 Stratospheric Inputs

Concentrations of ozone in the stratosphere are much higher than those in the troposphere. Cross-tropopause mixing can lead to net transport of high-ozone air from the stratosphere into the troposphere [*Holton et al.*, 1995], substantially affecting the regional abundance of ozone in the troposphere [*Tian et al.*, 2010]. Stratosphere-troposphere exchange (STE) has been the focus of numerous studies because of this potentially large source of ozone.

Overall, estimates of the mean cross-tropopause flux lie between 400 and 1400 Tg yr^{-1} [*Tarasick and Slater*, 2008], and the amount for a given year varies with events within the lower stratosphere [*Hsu and Prather*, 2009]. STE differs markedly depending on location, and efforts have been made to establish climatologies for the flux [*Stohl*, 2001; *Bourqui*, 2006; *Tilmes et al.*, 2010]. Variability in STE driven by meteorology is the largest driver of interannual variability in tropospheric ozone [*Voulgarakis et al.*, 2010; *Hess and Zbinden*, 2013]. Many of the observed features in the extratropical upper troposphere and lower stratosphere are captured by chemistry-climate models, although improvements in resolution and tropospheric chemistry are expected to improve model performance [*Hegglin et al.*, 2010].

At middle and high latitudes, deep intrusions of stratospheric air reach into the upper or middle troposphere. Evidence of STE events can be detected at the surface [*Ordóñez et al.*, 2007; *Langford et al.*, 2012], although this is more rare. The stratosphere is also an input of reactive nitrogen to the upper troposphere, mainly as nitric acid and NO_x [*Liang et al.*, 2011].

1.2.3 Loss and Deposition Processes

Ozone may be destroyed either chemically or through deposition to the Earth's surface. Chemical destruction of ozone in the troposphere occurs either through photolysis and subsequent reaction of the excited oxygen atom with water vapour:

$$O_3 + h\nu \longrightarrow O_2 + O(^1D) \quad \text{(R 1.12)}$$

$$O(^1D) + H_2O \longrightarrow 2\,OH, \quad \text{(R 1.13)}$$

or through consumption by HO_x radicals:

$$O_3 + HO_2 \longrightarrow OH + 2\,O_2 \quad \text{(R 1.14)}$$

$$O_3 + OH \longrightarrow HO_2 + O_2\,. \quad \text{(R 1.15)}$$

The dry deposition mass flux of a gas-phase species is typically considered to be proportional to the concentration of the trace gas near the surface [*Wesely and Hicks*, 2000]. The constant of proportionality, termed the deposition velocity, depends on a number of parameters that are a function of land surface, type of vegetative cover, and local meteorology. Deposition at the surface acts on not only ozone, but on a number of the precursor species discussed here. The deposition velocity for different trace gases on a given surface varies with the solubility and diffusivity of the gas in question.

1.3 Tropospheric Ozone Distribution and Trends

Ozone in the troposphere has a mean lifetime of 20–30 days (see Table 1.1), and is therefore subject to variations in abundance over seasonal timescales, as well as interannual trends. Concentrations of tropospheric ozone tend to be largest over the northern midlatitudes where anthropogenic emissions are concentrated. Chemical ozone production increases during the summer months with increased temperatures and availability of OH. Also, downward flux from the stratosphere to midlatitudes peaks in spring. This leads to a prolonged midlatitude maximum in the free troposphere that begins during the spring and is sustained during the summer by in situ production. This spring maximum extends across the Arctic [*Monks*, 2000], although the scale of the impact of midlatitude precursor emissions is uncertain.

The importance of ozone to atmospheric chemistry, air quality, and climate has instigated research and monitoring activities worldwide. The observational record has been examined for trends in ozone in the free troposphere [*Logan*, 1999; *Oltmans et al.*, 2006], at the surface [*Vingarzan*, 2004; *Chan*, 2009; *Lefohn et al.*, 2010], and in the Arctic troposphere and stratosphere [*Tarasick et al.*, 2005; *Kivi et al.*, 2007]. Some studies employ statistical regression models to determine trends in the data [*Logan*, 1999; *Kivi et al.*, 2007], while others employ chemical transport models to infer process-specific impacts on ozone abundances, for instance the impact of changes in precursor emissions on simulated trends [*Fusco and Logan*, 2003].

Trends in the northern midlatitude free tropospheric ozone abundance were predominantly positive during the 1970's and 1980's [*Logan*, 1999]. With emission reduction programs in industrialized countries, these trends decelerated in the 1990's and in some cases reversed. For example, the ozone trend in the free troposphere over Europe in the past decade indicates a decrease [*Logan et al.*, 2012]. Changes in precursor emissions, ozone abundance in the lower stratosphere, and surface temperatures all appear to affect free tropospheric trends [*Fusco and Logan*, 2003].

Ozone produced in the troposphere may persist for up to several weeks, allowing transport on hemispheric scales. Significant effort has been devoted to distinguishing ozone from local sources from the transported background concentrations [*Wild and Akimoto*, 2001; *Fiore et al.*, 2009; *Reidmiller et al.*, 2009; *Zhang et al.*, 2011]. Trends at the surface vary by location and change with time. Over North America, trends in the past two decades are generally negative along with reductions in anthropogenic emissions [*Vingarzan*, 2004; *Lefohn et al.*, 2010]. However, sites in less populated rural areas exhibit positive trends that are attributed to rising hemispheric background concentrations, both in North America [*Chan*, 2009] and in Europe [*Cui et al.*, 2011].

In the Arctic troposphere, trends in the 1980's and early 1990's were toward lower ozone concentrations [*Tarasick et al.*, 2005; *Oltmans et al.*, 2006]. Some of the variability in the ozonesonde record can be attributed to changes in ozone concentrations in the lower stratosphere [*Kivi et al.*, 2007]. In the late 1990's, this decreasing trend reversed [*Tarasick et al.*, 2005].

The complexity intrinsic to these trend studies makes it clear that controlling ozone abundances requires more sophistication than straightforward reductions in precursor emissions. The continuity of the observational record is crucial to gauging the response to pollution control methods. Further, tools that use these observations to distinguish regions where ozone concentrations are more strongly influenced by anthropogenic activity or natural sources are particularly valuable from an informed policy perspective.

1.4 Structure of the Thesis

This work comprises three studies of ozone that span the northern middle and high latitude troposphere. The next chapter presents the observations and modelling tools that will be employed in the various studies. The three following chapters comprise the individual research studies, and a summative chapter (Chapter 6) closes the thesis.

Chapter 3 presents a study of ozone abundances in the Arctic summertime. This study aims to understand the contributing source regions and chemical pathways that influence the distribution of ozone in the Arctic free troposphere. Also, it examines the budget of ozone production and transport north of 60°N. The contents of this chapter have been published [*Walker et al.*, 2012], with the candidate as lead author. The candidate performed the modelling analyses in the published work and wrote the majority of the text, parts of which are reproduced here with the publisher's permission.

Chapter 4 describes a modelling analysis of the sensitivity of surface ozone over North America to precursor emissions, key chemical reactions, and to dry deposition. The goal of the work is to identify the processes that could account for the bias in North American surface ozone simulated by the model.

Chapter 5 shows the results from data assimilation experiments using ozonesonde observations to constrain the lightning NO_x emissions source. Global inversions are presented, but a major focus is finding the continental-scale source over North America and its effects on the free tropospheric ozone distribution. The analysis presented for the Solar Occultation for Atmospheric Research (SOAR) mission has been submitted in a report to the Canadian Space Agency [*Walker et al.*, 2009]. The candidate contributed modelling analysis of the potential impacts of measurements from SOAR on meeting its science goals.

Chapter 2

Theory and Methods

2.1 The GEOS-Chem Model

Chemical transport models (CTMs) encapsulate our understanding of the dynamical, chemical, and physical processes that determine atmospheric composition. They attempt to calculate the evolution of atmospheric concentrations of trace gases in time and space. Used in conjunction with in situ or remote sensing observations, these models provide valuable insight into the current state of the atmosphere. These versatile tools have been used to guide measurement campaigns [e.g., *Fisher et al.*, 2010], attribute pollution to distinct sources [e.g., *Fiore et al.*, 2009], and as an intercomparison platform for disparate or sparse measurements [e.g., *Zhang et al.*, 2010]. While CTMs offer powerful tools for interpreting composition measurements, a thorough knowledge of their biases and limitations is also necessary.

The GEOS-Chem CTM (http://www.geos-chem.org/) has been described and used in numerous studies of tropospheric composition [*Bey et al.*, 2001; *Fiore et al.*, 2002; *Martin et al.*, 2002b, 2003b; *Park et al.*, 2004; *Evans and Jacob*, 2005]. This model is used here to explain observations of ozone and its precursors, and also as a platform for

data assimilation. The set-up of GEOS-Chem and its application to each study will be described in the respective chapters, while an overview of common features is given here.

The GEOS-Chem chemical mechanism comprises 43 active chemical tracers, some of which are lumped from a number of chemical species (e.g., the NO_x tracer contains the sum of NO and NO_2). A full set of gas phase reactions describing the NO_x-HO_x-VOC chemistry as well as certain heterogeneous reactions [*Evans and Jacob*, 2005] is solved at each model time step to update the simulated trace gas distribution. Individual reactions may be deactivated within the mechanism to assess their impact on the simulation. Emissions and both wet and dry deposition of trace gases are also represented. The model does not explicitly account for chemistry in the stratosphere. Instead, the stratospheric source of ozone is represented by the linearized ozone (LINOZ) parameterization [*McLinden et al.*, 2000]. In the LINOZ scheme, the tendency of ozone in the stratosphere, that is, its time derivative, depends on the local ozone mixing ratio, the temperature, and the overlying column abundance of ozone. The tendency is calculated using the deviation of these three quantities from their climatological values in a first-order Taylor series.

Transport in GEOS-Chem is driven by meteorological data from the Global Modelling and Assimilation Office (GMAO), which is read into the model every 6 hours (3 hours for surface variables) [*Bey et al.*, 2001]. The trace gas distribution calculated by the CTM does not affect the meteorological variables. The GMAO meteorology fields are employed in a semi-Lagrangian advection scheme [*Lin and Rood*, 1996]. Convection is parameterized differently in the two versions of the GMAO fields employed in this document; in GEOS-4, deep [*Zhang and McFarlane*, 1995] and shallow [*Hack*, 1994] convection are treated separately, while in GEOS-5, all convection is formulated using a relaxed Arakawa-Schubert parameterization [*Moorthi and Suarez*, 1992]. Convective outflow in the upper troposphere is weaker in the relaxed Arakawa-Schubert scheme than in the GEOS-4 parameterization [*Folkins et al.*, 2006].

GEOS-Chem may be used on the global domain at either $4^\circ \times 5^\circ$ or $2^\circ \times 2.5^\circ$ resolution in the horizontal. The model may use a finer horizontal grid on a smaller domain, as will be discussed in later chapters. The vertical resolution depends to some extent on the meteorological fields being used. The GEOS-4 grid [*Bloom et al.*, 2005] has 55 levels, while the GEOS-5 grid [*Rienecker et al.*, 2008] has 72. Both, however, extend from the surface to 0.01 hPa, using a hybrid pressure-sigma grid. The vertical layers follow the terrain near to the surface, and transition to smooth layers higher in the atmosphere. The GEOS-5 grid has better resolution near the surface, with roughly 14 layers in the lowest 2 km (the GEOS-4 vertical grid has 5 layers in the lowest 2 km). The vertical layer spacing for both grids near the midlatitude tropopause is similar, at about one layer per kilometre.

The GEOS-Chem model may be run in a tagged ozone mode. In a tagged ozone simulation the ozone chemistry is linearized using production rates and loss frequencies archived from a full chemistry simulation. This allows the use of separate tracers to track odd oxygen ($O_x = O_3 + NO_2 + 2NO_3 + PAN + MPAN + PPN + 3N_2O_5 + HNO_4 + HNO_3$) produced in different user-defined source regions.

Lightning Emissions in GEOS-Chem

The lightning emissions scheme in GEOS-Chem will be scrutinized in later chapters, so an overview of the model calculation is provided here. A well-known power law relationship between the cloud-top height and flash rate in convective systems is sometimes used in global models to estimate the lightning flash distribution [*Price and Rind*, 1992], and has been validated against satellite observations in the tropics [*Price and Rind*, 1992; *Yoshida et al.*, 2009]. The parameterization assumes separated regions of charge, whose volume scales with the vertical cloud dimension. The flash rate f can be parameterized as a function of the cloud-top height h as follows:

$$f = \alpha h^{\beta}, \tag{2.1}$$

where α and β are empirically-determined constants [*Price and Rind*, 1992]. The exponent β has a value of 4.9 ± 0.3 over continents, as shown in Figure 2.1.

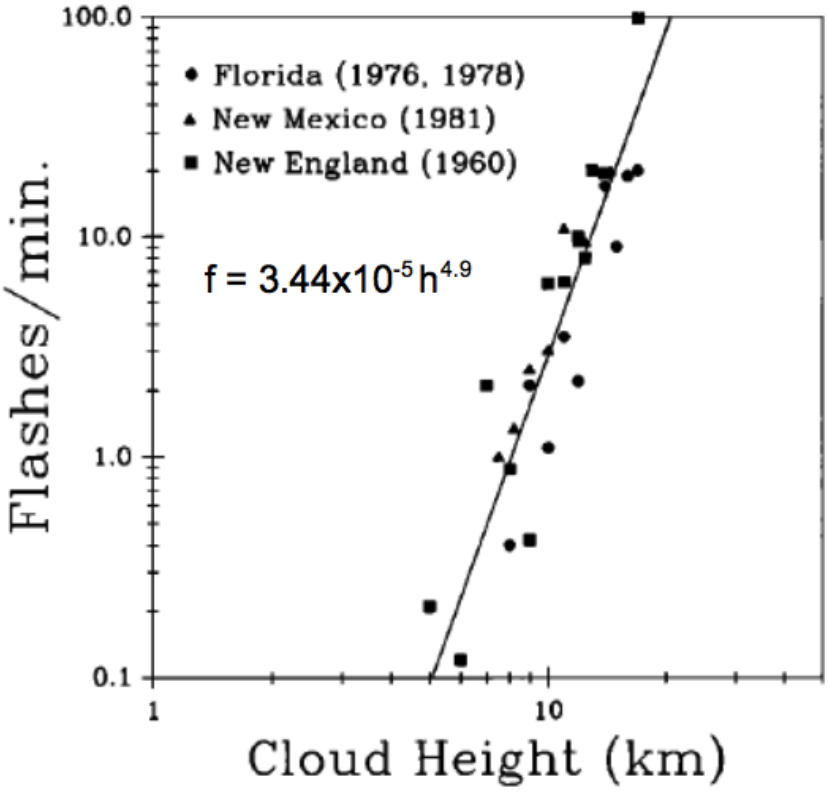

Figure 2.1: Empirical power law relationship between lightning flash rate and convective cloud top height over land at northern midlatitudes. Adapted from *Price and Rind* [1992].

Lightning is observed more often over land than over ocean. More sensible heat over land leads to stronger updrafts, and a more efficient separation of charges within storms over land. Separate sets of parameters are used in *Price and Rind* [1992] over land and over oceans on the basis of maritime observations and the weaker updrafts

observed in maritime storms. The land-ocean distinction is retained in the GEOS-Chem implementation.

The cloud-top height parameterization relies on accurate knowledge of cloud parameters in the simulation and sufficient resolution to accurately describe these parameters. Nonetheless, determining flash rates using cloud-top height seems to offer better performance than parameterizations based on other cloud properties that correlate with lightning activity, such as ice water path or updraft volume [*Barthe et al.*, 2010].

An improved method to combine the cloud-top height parameterization with satellite-based constraints has been implemented in GEOS-Chem, in addition to the Price and Rind parameterization. The flash distribution estimated in the Price and Rind scheme is rescaled by a climatology of Optical Transient Detector and Lightning Imaging Sensor (OTD-LIS) observed flashes and constrained to the mean global annual flash rate [*Sauvage et al.*, 2007; *Murray et al.*, 2012]. The flash distributions obtained by the Price and Rind method and by the OTD-LIS rescaling over North America are compared in Figure 2.2. Generally, the OTD-LIS rescaling places more flashes over the midlatitudes and over oceans than the unscaled Price and Rind scheme.

2.1.1 Nested Model with Improved Resolution

On the global domain, the GEOS-Chem CTM typically is run at a degraded resolution ($4^\circ \times 5^\circ$ or $2^\circ \times 2.5^\circ$) due to the high resource demand of high resolution global simulations. However, the model may be used at the native resolution of the GEOS-5 meteorological fields ($0.5^\circ \times 0.666^\circ$) over a limited spatial domain in a so-called "nested" simulation [*Wang et al.*, 2004; *Chen et al.*, 2009]. For a nested simulation, the model is first run on the global domain, and the chemical state is archived to provide boundary conditions to the nested domain. The nesting is unidirectional; results at the high resolution do not feed back on the chemical state of the global simulation. The vertical resolution is the same for the nested and global domains.

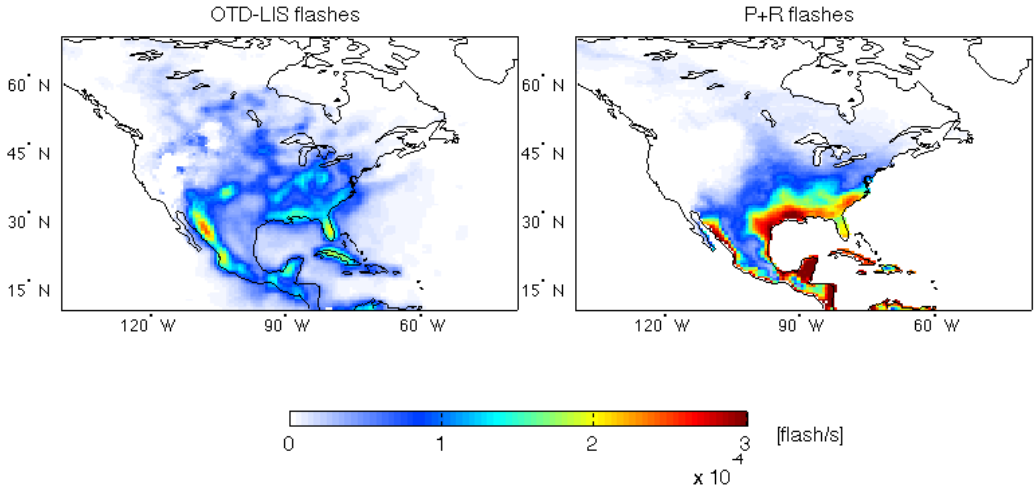

Figure 2.2: Lightning flash rates in flashes per second, estimated in GEOS-Chem at $0.5° \times 0.666°$ horizontal resolution using (left) the OTD-LIS rescaling and (right) the unscaled Price and Rind parameterization over North America in August 2006.

Simulations with higher resolution have the potential to improve the model's representativeness, especially in regions containing large horizontal concentration gradients. For example, the nested model grid cells are fine enough to distinguish between urban and suburban areas, which can represent different chemical domains [*Chen et al.*, 2009]. This has implications for the model's usefulness for air quality policy [*Zhang et al.*, 2011]. Using the high-resolution model in inversions for emissions allows the resolution of fine-scale variations [*Stavrakou and Müller*, 2006; *Kopacz et al.*, 2009] and reduces the potential for aggregation errors [*Jiang et al.*, 2011].

A comparison of simulated surface ozone over North America is shown in Figure 2.3 at both the $4° \times 5°$ and the $0.5° \times 0.666°$ resolutions. While the coarse resolution represents large-scale features and is suitable for global studies of long-range transport and

continental outflow, the coarse grid cells clearly average over small-scale heterogeneity that is important for studies of surface air quality. For example, the fine-resolution model explicitly represents high ozone concentrations along the Ohio River Valley (extending southwest from the south shore of Lake Erie). This feature is subsumed in the coarse-resolution model within a single grid cell.

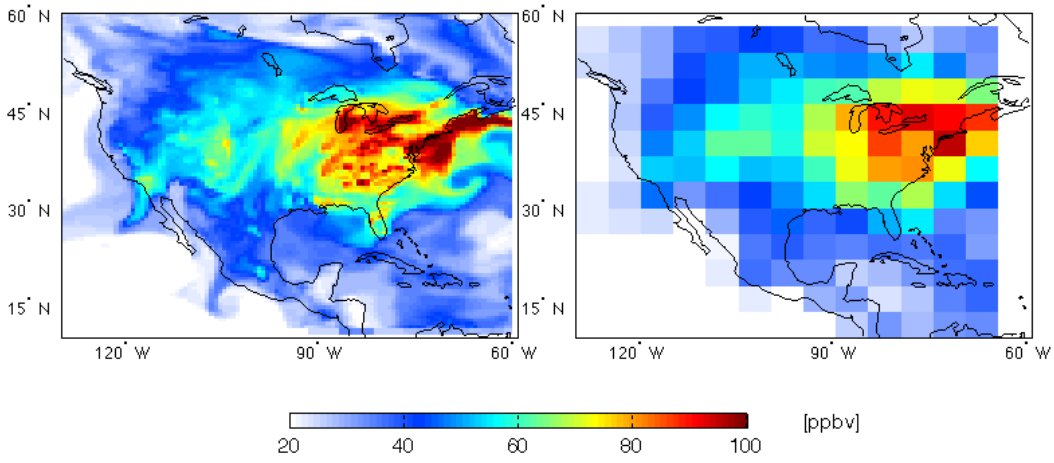

Figure 2.3: Modelled ozone on August 1, 2006 at 1800 UTC in the surface layer at the $0.5° \times 0.666°$ (left) and $4° \times 5°$ (right) resolutions.

2.2 Data Assimilation Techniques

The objective of chemical transport modelling is to simulate the state of the real atmosphere; one method to improve on the simulated state is to introduce observational constraints into the modelling framework. Data assimilation aims to combine the model estimate of the atmospheric state and observations of the state in a manner that is consistent with our understanding of the uncertainties involved in the model and observations.

Both the simulated state and the observations are characterized by finite uncertainties, and can be described by their probability density functions. Bayes' theorem gives an approach to the data assimilation problem [*Rodgers*, 2000]:

$$P(x|y) = \frac{P(y|x)P(x)}{P(y)}, \tag{2.2}$$

where $P(x)$ is the probability density function of the state variable x, and $P(x|y)$ indicates the conditional probability that x has a certain value given a particular value of the observation y. Conceptually, we begin with a model-simulated estimate of the state (described by $P(x)$). This is combined with the information from the observations (described by the probability density function of observing a particular value, $P(y)$), transformed into the model space ($P(y|x)$). The result is an improved estimate of the state that accounts for the observations ($P(x|y)$).

Often, the probability density functions considered in data assimilation problems are assumed to be Gaussian. For a vector $\mathbf{x}$ of length n, the multivariate Gaussian probability density function takes the form:

$$P(x) = \frac{1}{(2\pi)^{n/2}|\mathbf{S}_x|^{1/2}} \exp\left(-\frac{1}{2}(\mathbf{x}-\bar{\mathbf{x}})^T\mathbf{S}_x^{-1}(\mathbf{x}-\bar{\mathbf{x}})\right), \tag{2.3}$$

where $\mathbf{S}_x$ is the covariance matrix associated with $\mathbf{x}$, and $\bar{\mathbf{x}}$ is the mean value of $\mathbf{x}$. If we consider a linear model of a set of variables $\mathbf{x}$ that produces an estimate of the observed quantity $\mathbf{y}$ with an error described by ϵ,

$$\mathbf{y} = \mathbf{K}\mathbf{x} + \epsilon, \tag{2.4}$$

where $\mathbf{K}$ is the Jacobian matrix [*Rodgers*, 2000]. Assuming the distribution of errors ϵ is Gaussian gives

$$-2\ln(P(\mathbf{y}|\mathbf{x})) = (\mathbf{y}-\mathbf{K}\mathbf{x})^T\mathbf{S}_\epsilon^{-1}(\mathbf{y}-\mathbf{K}\mathbf{x}) + C_1, \tag{2.5}$$

where $\mathbf{S}_\epsilon$ is the measurement error covariance, and C_1 is a constant arising from the normalization.

Similarly, if the errors of the a priori guesses ($\mathbf{x}_a$) for the variables $\mathbf{x}$ are assumed to be Gaussian,

$$-2\ln(P(\mathbf{x})) = (\mathbf{x}-\mathbf{x}_a)^T\mathbf{S}_a^{-1}(\mathbf{x}-\mathbf{x}_a) + C_2, \tag{2.6}$$

where $\mathbf{S}_a$ is the covariance associated with deviation of the state vector from its a priori value, and C_2 is a constant.

Combining Equations (2.5) and (2.6) in Bayes' theorem gives an expression for the conditional probability of the variables $\mathbf{x}$ given the observations $\mathbf{y}$.

$$-2\ln(P(\mathbf{x}|\mathbf{y})) = (\mathbf{y}-\mathbf{K}\mathbf{x})^T\mathbf{S}_\epsilon^{-1}(\mathbf{y}-\mathbf{K}\mathbf{x}) + (\mathbf{x}-\mathbf{x}_a)^T\mathbf{S}_a^{-1}(\mathbf{x}-\mathbf{x}_a) + C_3, \tag{2.7}$$

where C_3 is a constant.

Bayes' theorem does not calculate an explicit state as the solution; rather, it describes the probability density function of possible states given the combined information from the model and observations. The full characterization of this function is difficult, so typically approaches select either the mean (as in the maximum likelihood approach) or the mode (as in the maximum a posteriori approach) as the estimate of the state. The work in this thesis adopts the latter approach, which maximizes the probability density function by minimizing Equation (2.7). A number of specific methods have been developed for calculating this representative state and its uncertainty. We will detail two such methods here: the Kalman filter and four-dimensional variational assimilation.

2.2.1 The Kalman Filter

The general data assimilation problem can be formulated with the assumption that the state of the atmosphere progresses in such a way that the evolution of the state between

successive observations can be modelled. The problem can be stated in discrete form as a combination of a prediction equation and a measurement equation, with their respective errors:

$$\mathbf{x}_t = M_t(\mathbf{x}_{t-1}) + \xi_t \tag{2.8}$$

$$\mathbf{y}_t = F_t(\mathbf{x}_t) + \epsilon_t, \tag{2.9}$$

where M_t is the non-linear model that evolves the model state $\mathbf{x}$ between successive timesteps, and ξ_t is the model prediction error, which may represent deviations due to a combination of unmodelled processes and stochastic variations in the model state. The non-linear measurement model F_t relates the model state $\mathbf{x}_t$ to the observations $\mathbf{y}_t$ and their errors ϵ_t. The linear version of the problem can be stated

$$\mathbf{x}_t = \mathbf{M}_t(\mathbf{x}_{t-1}) + \xi_t \tag{2.10}$$

$$\mathbf{y}_t = \mathbf{K}_t(\mathbf{x}_t) + \epsilon_t, \tag{2.11}$$

where $\mathbf{M}_t$ is a linearization of the non-linear model M_t, and the Jacobian $\mathbf{K}_t$ linearizes the measurement model F_t. The Kalman filter operates sequentially, so at timestep t, the prediction equation is used to generate an a priori estimate (or forecast) of the state $\mathbf{x}_{a,t}$ and its covariance $\mathbf{S}_{a,t}$:

$$\mathbf{x}_{a,t} = \mathbf{M}_t(\mathbf{x}_{t-1}) \tag{2.12}$$

$$\mathbf{S}_{a,t} = \mathbf{M}_t\mathbf{S}_{t-1}\mathbf{M}_t^T + \mathbf{S}_{\xi t}. \tag{2.13}$$

These estimates are combined with observations at time t to obtain an optimal estimate of the state and its covariance [*Rodgers*, 2000]:

$$\mathbf{G}_t = \mathbf{S}_{a,t}\mathbf{K}_t^T(\mathbf{K}_t\mathbf{S}_{a,t}\mathbf{K}_t^T + \mathbf{S}_\epsilon)^{-1} \quad (2.14)$$

$$\hat{\mathbf{x}}_t = \mathbf{x}_{a,t} + \mathbf{G}_t(\mathbf{y}_t - \mathbf{K}_t\mathbf{x}_{a,t}) \quad (2.15)$$

$$\hat{\mathbf{S}}_t = \mathbf{S}_t - \mathbf{G}_t\mathbf{K}_t\mathbf{S}_{a,t}, \quad (2.16)$$

where $\mathbf{G}_t$ is called the Kalman gain matrix. Note that calculating the gain matrix involves the inversion of a large matrix. The covariance $\hat{\mathbf{S}}_t$ must also be stored and propagated at every timestep. The size of the state space in atmospheric chemistry models is large, making the time propagation of the covariance matrix intractable.

However, variations of the Kalman filter have been adopted for chemical data assimilation [*Lamarque et al.*, 2002; *Segers et al.*, 2005; *Parrington et al.*, 2008]. More recently, ensemble Kalman filter methods have been introduced [*Tang et al.*, 2011; *Coman et al.*, 2012; *Miyazaki et al.*, 2012] that use simulations with different realizations of the observation error ϵ_t in order to produce an ensemble of forecast states from which the forecast error covariance $\mathbf{S}_{a,t}$ may be calculated. The number of ensemble members required to get good statistics depends on the particular application; for instance, *Miyazaki et al.* [2012] found that 32 members was optimal for their application. The generation of this ensemble still requires several evaluations of the forward model, a shortcoming that can be avoided using a variational approach.

2.2.2 Four-Dimensional Variational Data Assimilation

Data assimilation in a four-dimensional variational framework (4D-Var) combines prior knowledge about the background atmospheric state, knowledge of the chemical and physical processes that control the temporal evolution of that state, and observations of certain components of the state distributed over an assimilation period $[t_0, t_N]$ [*Sandu et al.*, 2005]. Each of these sources of information is imperfect and has associated uncertainties. Unlike the Kalman filter, which introduces the data into the model in a sequential

fashion, or 3D-Var, which neglects the time dependence of the observations during the assimilation period, the 4D-Var algorithm attempts to optimize the model trajectory to best fit all the data over the assimilation period. The 4D-Var algorithm is therefore considered a smoother, unlike the Kalman filter or the 3D-Var approach.

Our knowledge about the processes that govern the evolution of the atmospheric state $\mathbf{x}$ are expressed in a model M that relates the current and future states:

$$\mathbf{x}_{n+1} = M(\mathbf{x}_n, \mathbf{c}) \equiv M_n, \tag{2.17}$$

which is analogous to Equation (2.8). Here $\mathbf{c}$ represents a set of parameters that serve as inputs to the model. Given a set of parameters $\mathbf{c}$, the model operator is deterministic, so from an initial state $\mathbf{x}_0$, the complete evolution of the model state with time can be calculated through the iterative application of Equation (2.17). The model is in general imperfect, and may suffer from numerical discretization errors, representation errors in its parameterizations, or errors due to missing processes. However, it is generally assumed that these model errors are small over the course of the simulation, and thus that the model provides a strong constraint on the state evolution.

The uncertainties on the input parameters $\mathbf{c}$ and the initial condition $\mathbf{x}_0$ are known or may be estimated. Often, in order to limit the size of the inversion problem, a set of parameters (called the control parameters) are chosen as those that will be modified to find the optimal model state. We choose the optimal state as that which maximizes the a posteriori distribution of states ($P(\mathbf{x}|\mathbf{y})$) from Equation (2.7). This optimal state is determined as that which minimizes a scalar cost function J:

$$J = \frac{1}{2}\sum_{n=0}^{N}(\mathbf{x}_n - \mathbf{x}_n^{obs})^T\mathbf{S}_{obs}^{-1}(\mathbf{x}_n - \mathbf{x}_n^{obs}) + \gamma\frac{1}{2}(\mathbf{c} - \mathbf{c}_0)^T\mathbf{S}_a^{-1}(\mathbf{c} - \mathbf{c}_0), \tag{2.18}$$

where $\mathbf{x}_n^{obs}$ represents the observations of the model state distributed in time and space over the simulation domain. The covariance matrix $\mathbf{S}_{obs}$ contains the observation errors and correlations between observations. The error information weights the model-

observation differences so that more precise observations have a bigger influence. Similarly, the matrix $\mathbf{S}_a$ contains error and correlation information about the initial estimates of control parameters $\mathbf{c}_0$. The specific implementation of the covariance matrices depends on the problem being addressed, so further details are left to later chapters. γ is a regularization factor that weights the deviations from the initial parameter estimates and the deviations of the simulated and observed state [*Hakami et al.*, 2005]. The inversions in this thesis all use $\gamma = 1$. Figure 2.4 depicts a state variable $\mathbf{x}_n$ being corrected by a set of observations $\mathbf{x}_n^{obs}$ over the assimilation window $[t_0, t_N]$.

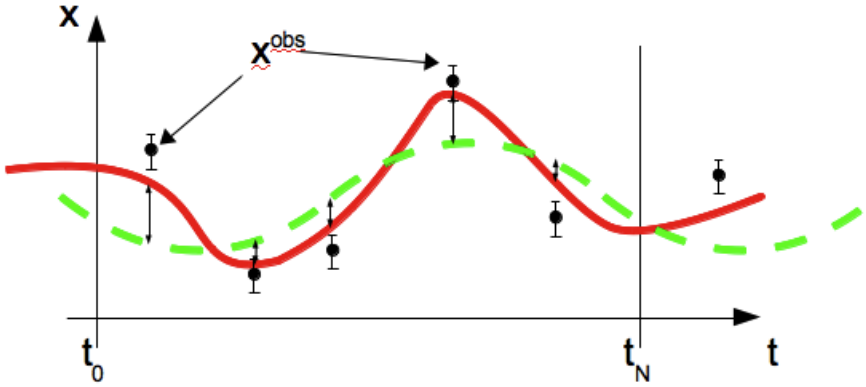

Figure 2.4: Depiction of the corrections to the model state in a 4D-Var assimilation system. The prior model state (green dashed line) is corrected using observations (black circles) during the assimilation window $[t_0, t_N]$. The corrected model state (red solid line) is the model trajectory that best fits the observations. The corrected state can be used in future iterations to further reduce the model-observation mismatch.

In order to minimize J, one needs to know how J varies given a perturbation in the model parameters:

$$\nabla J = \sum_{n=0}^{N} \mathbf{S}_{obs}^{-1} \nabla M_n^T (\mathbf{x}_n - \mathbf{x}_n^{obs}) + \gamma \mathbf{S}_a^{-1} (\mathbf{c} - \mathbf{c}_0). \tag{2.19}$$

The 4D-Var algorithm is to apply the model using an initial estimate of parameters, calculate the gradient of the cost function around that simulated state, and finally use the gradients in a minimization process that produces a new estimate of the model parameters. The gradient of J can be cumbersome to calculate using only the model M — one would need to calculate M for a perturbation of every parameter in $\mathbf{c}$ (and for every iteration of the minimization), which is intractable for atmospheric models where the number of parameters is very large. An adjoint model provides a more efficient means of calculating the gradient of J with respect to all the parameters simultaneously in a single integration.

Adjoint models have become more widely applied to problems of atmospheric composition in the past 15 years [e.g., *Elbern et al.*, 2000; *Elbern and Schmidt*, 2001; *Vautard et al.*, 2000]. An adjoint model efficiently calculates the gradient, or sensitivity, of model outputs to a range of model inputs. For atmospheric composition studies, the sensitivities may be calculated with respect to a previous concentration distribution, or to specific model parameters (e.g., emission rates). The sensitivities obtained from an adjoint model may be interpreted on their own in a receptor-based paradigm (as in *Vautard et al.* [2000]), or may be used iteratively to constrain the model in a variational data assimilation context (as in *Elbern et al.* [2000]).

The forecast model M_n relates the current state and model parameters to the future state at time step n. If we assume a linear model M_n, perturbations in either the model state or the model parameters will propagate forward into the model state according to:

$$\delta\mathbf{x}_{n+1} = \frac{\partial M}{\partial \mathbf{x}}(\mathbf{x}_n, \mathbf{c})\delta\mathbf{x}_n + \frac{\partial M}{\partial \mathbf{c}}(\mathbf{x}_n, \mathbf{c})\delta\mathbf{c}. \tag{2.20}$$

Let us take the initial conditions x_0 to be the control parameters. We wish to calculate the perturbation in the cost function δJ:

$$\delta J = \sum_{n=0}^{N} \langle \nabla_{\mathbf{x}_n} J, \delta\mathbf{x}_n \rangle, \tag{2.21}$$

where $\nabla_{\mathbf{x}_n}$ represents the directional derivative in the direction of the perturbation in $\mathbf{x}$ at time step n, and the angle brackets denote an inner product. The sum is taken over the assimilation window, because J can depend on observations during that time frame. The iterative application of the forward model M can be used to relate the perturbation to the model state $\mathbf{x}_n$ to a perturbation in the initial conditions $\mathbf{x}_0$.

$$\begin{aligned} \delta J &= \langle \nabla_{\mathbf{x}_n} J, M_{n-1} M_{n-2} \dots M_0 \delta \mathbf{x}_0 \rangle \\ &= \sum_{n=0}^{N} \langle \mathbf{M}_0^* \mathbf{M}_1^* \dots \mathbf{M}_{n-1}^* \nabla_{\mathbf{x}_n} J, \delta \mathbf{x}_0 \rangle, \end{aligned} \tag{2.22}$$

where $\mathbf{M} = \nabla M$ and the superscript * represents the adjoint of the linear model operator. Relating this to Equation (2.21), we find that

$$\nabla_{\mathbf{x}_0} J = \sum_{n=0}^{N} \mathbf{M}_0^* \mathbf{M}_1^* \dots \mathbf{M}_{n-1}^* \nabla_{\mathbf{x}_n} J. \tag{2.23}$$

The adjoint gradients may be useful on their own as indicators of sensitivity of the model state to various parameters. Two examples of the gradients calculated by an adjoint model of atmospheric composition are displayed in Figure 2.5. For this illustration, we use a cost function that is simply the mean simulated concentration of surface ozone in northwestern West Virginia (magenta box in Figure 2.5) during the afternoons in the first ten days of August 2006. The left panel shows the gradients of this cost function with respect to anthropogenic NO_x emissions. The right panel shows the gradients with respect to the ozone deposition rate.

Let us denote the gradient at a particular latitude i and longitude j by λ_{ij}. The gradients shown here and elsewhere in this thesis have been fully normalized into units of percent:

$$\lambda_{ij} = \frac{1}{J} \frac{\partial J}{\partial c_{ij}} \times 100. \tag{2.24}$$

If the model parameter c_{ij} at a particular location changes by a fractional amount ρ_{ij}, then the expected percent change in the cost function is $\rho_{ij}\lambda_{ij}$. Prevailing wind direction during the simulation was from the west, and the adjoint model has propagated the gradients in an upwind direction. A positive change (i.e., an increase) in anthropogenic NO_x emissions in southern Ohio and along the Ohio River Valley will result in an increase in surface ozone in West Virginia. Similarly, a decrease in the ozone dry deposition rate will increase surface ozone. While both gradients are calculated from the same cost function (indeed, during the same adjoint model run), the spatial distributions of the gradients differ, with the sensitivity to deposition rate being much more localized than that to emissions.

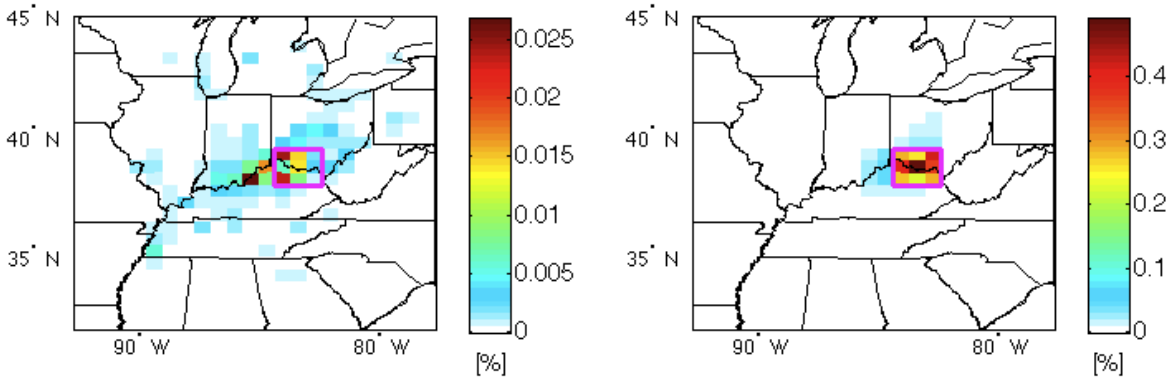

Figure 2.5: Fully normalized adjoint gradients with respect to anthropogenic NO_x emissions (left) and O_3 deposition rate (right, multiplied by -1) for a cost function equal to the mean surface ozone concentration within the magenta box between 1200-1800h local time for the first ten days of August 2006. The gradients are shown in units of percent, as described in Equation (2.24).

2.2.3 The Adjoint Model of GEOS-Chem

The initial development of the GEOS-Chem adjoint model was described in *Henze et al.* [2007]. The current adjoint version is based on GEOS-Chem version v8-02-01, and is updated in parallel to the standard GEOS-Chem model. The GEOS-Chem adjoint was developed initially for inverse modelling of aerosol precursors [*Henze et al.*, 2007, 2009], and since then has been applied for inverse modelling of CO [*Kopacz et al.*, 2009, 2010; *Jiang et al.*, 2011] and tropospheric ozone [*Zhang et al.*, 2009; *Singh et al.*, 2011; *Walker et al.*, 2012]. For the work described in Chapter 4, the adjoint was extended to account for the sensitivity with respect to reaction rates, including rates of dry deposition. The GEOS-Chem adjoint uses the L-BFGS-B algorithm [*Byrd et al.*, 1995], which is designed for bounded optimization problems using limited memory.

Many components of the GEOS-Chem adjoint model are derived using automatic differentiation algorithms [*Giering and Kaminski*, 1998; *Sandu et al.*, 2003; *Daescu et al.*, 2003]. The adjoint of the advection operator uses a continuous approach, where the same advection scheme is solved as in the forward model, but the winds are reversed — an approach favoured over discrete differentiation for the type of advection scheme employed in GEOS-Chem [*Henze et al.*, 2007; *Hakami et al.*, 2007; *Gou and Sandu*, 2011]. Specifics of the adjoint model configuration for each study will be given in the appropriate chapters.

2.3 Observations of Trace Gases in the Troposphere

Measurements of the chemical state of the atmosphere ground modelling work in reality. An overview of the various types of measurements that are studied in later chapters is given here, with specifics applicable to each study given in later chapters.

2.3.1 Measurements at the Surface

Ground-based in situ instruments are routinely used to measure trace gas concentrations, often in the context of air quality monitoring. For ozone, commercial instruments are available that measure ambient concentrations via ultraviolet absorption to within ±10% [*Sickles and Shadwick*, 2002]. Reactive nitrogen oxides are most often measured with a chemiluminescence analyzer with a molybdenum converter [*Lamsal et al.*, 2008]. These converters have some susceptibility to interferences from other reactive nitrogen species, causing overestimates of the NO_2 concentration of up to 50% [*Dunlea et al.*, 2007; *Steinbacher et al.*, 2007].

Other components of total reactive nitrogen are measured using a number of different techniques. Measurements of peroxyacetyl nitrate (PAN) using a gas chromatograph with electron capture detection have been performed in the Canadian Arctic with an overall accuracy of ±30% [*Bottenheim et al.*, 1993]. Other recent techniques rely on the components of total reactive nitrogen dissociating at different temperatures. Thermal dissociation instruments have been designed that employ chemical ionization mass spectrometry (CIMS) [*Wolfe et al.*, 2007, 2009] and laser-induced fluorescence (LIF) [*Day et al.*, 2002; *Farmer et al.*, 2006].

Measurements at the surface for air quality monitoring provide long-term records of data. There are sites established by national agencies in networks to study the spatial variations in air quality across the country, such as the United States' Air Quality System (AQS, *Chameides et al.* [1997]) or the Canadian National Air Pollution Surveillance Program (NAPS, *Curren and Dann* [2004]). Some research groups maintain a mobile air quality lab that can be deployed for supplemental observations during intensive measurement campaigns (e.g., NATIVE, described in *Martins et al.* [2012]).

Ground sites may also be outfitted to measure dry or wet deposition of trace species to the surface. For example, sites in the Clean Air Status and Trends Network (CASTNET) [*Baum-*

gardner et al., 2002; *Sickles and Shadwick*, 2002] routinely monitor deposition of ozone and nitrogen-containing compounds, in addition to their concentrations.

2.3.2 Ozonesondes

Ozonesondes are balloon-borne in situ instruments that measure a vertical profile of ozone concentration and are coupled to a radiosonde instrument that measures temperature, relative humidity, and pressure. A profile from a typical sounding extends from the surface into the middle stratosphere. Electrochemical concentration cells (ECCs) are the most common instrument on modern ozonesondes [*Komhyr*, 1969]. A mechanical pump pulls ambient air through a two-part cell containing a buffered potassium iodide solution. The cell produces a current proportional to the ozone concentration in this air [*Smit et al.*, 2007].

A network of global long-term ozonesonde data is stored by the World Ozone and Ultraviolet Data Centre (WOUDC) [*Environment Canada et al.*, 2009]. Launch frequency differs depending on the site, and the distribution of sites changes with time as national programs are funded or discontinued. The instrument preparation methods are subject to periodic intercomparisons to ensure consistency throughout the network, and when standard procedures are used, precision is better than ±(3–5)% and accuracy is better than ±(5–10)% below 30 km altitude in the absence of significant amounts of interfering gases [*Smit et al.*, 2007]. Although the instruments can report concentrations as quickly as every second (roughly every 5 m for typical rise rates), their response rate to rapid concentration changes results in an effective vertical resolution of 50–100 m [*Smit et al.*, 2007]. The WOUDC is a global resource that provides an invaluable tool for trend analyses [e.g., *Oltmans et al.*, 2006; *Kivi et al.*, 2007; *Logan et al.*, 2012], validation studies [e.g., *Nassar et al.*, 2008; *Doughty et al.*, 2011], and as climatological averages used as prior information for retrievals [e.g., *McPeters et al.*, 2007; *McPeters et al.*, 2012].

Networks of coordinated ozonesonde launches occur on a campaign basis, and can provide excellent short-term coverage. Such networks operate in the tropics (e.g., the South Hemispheric ADditional OZonesondes (SHADOZ) [*Thompson et al.*, 2003]), midlatitudes (e.g., IONS [*Thompson et al.*, 2007]), and the Arctic (e.g., the Match campaigns [*Rex et al.*, 1998]).

2.3.3 Satellite Remote Sensing

Remote sensing instruments operating from space provide observations of the chemical composition of the atmosphere with better spatiotemporal coverage than can be achieved with in situ methods. This is achieved, however, at the expense of precision and ease of interpretation. In this work, we use information from the Tropospheric Emission Spectrometer (TES) [*Beer et al.*, 2001], which is a high-resolution infrared Fourier transform spectrometer on board NASA's Aura satellite. Aura was launched in July 2004 into a Sun-synchronous polar orbit with a local equator-crossing time of 13:45 and a repeat cycle of 16 days. TES currently operates in global survey mode, taking observations every 220 km along its orbital track with an instrument field-of-view of 8 km $\times$ 5 km at the surface. The instrument observes in the nadir at wavelengths from 650–3050 cm^{-1} with an apodized spectral resolution of 0.1 cm^{-1}.

Ozone profiles are retrieved from TES radiances in the 950–1050 cm^{-1} range using an optimal estimation approach [*Bowman et al.*, 2002, 2006; *Worden et al.*, 2004]. Ozone abundances are expressed as the natural logarithm of the volume mixing ratio in the retrievals, which are performed on a 67-level vertical grid with spacing of approximately 1 km. The TES retrievals can be expressed as a linear estimate of the atmospheric state

$$\hat{\mathbf{x}} = \mathbf{x}_a + \mathbf{A}(\mathbf{x} - \mathbf{x}_a), \tag{2.25}$$

where $\mathbf{x}$ is the true atmospheric state, $\mathbf{x}_a$ is the TES a priori profile, and $\mathbf{A}$ is the averaging kernel matrix, which represents the sensitivity of the retrieval to the true state.

On average, TES ozone retrievals contain between 3 and 4 degrees of freedom for signal, fewer than 1.5 of which are contributed by the troposphere in extra-tropical retrievals. The number of degrees of freedom is equal to the trace of the averaging kernel, and is a measure of the information content of the retrieval. TES ozone retrievals have been validated with ozonesonde data [*Worden et al.*, 2007; *Nassar et al.*, 2008; *Boxe et al.*, 2010] and lidar data [*Richards et al.*, 2008] and show a 10–15% positive bias in the free troposphere.

Parrington et al. [2008] assimilated tropospheric ozone and CO profile data from TES into the GEOS-Chem model using a suboptimal sequential Kalman filter. The filter operates on a 6-hour analysis cycle, and ingests TES data along the satellite track. The bias in the TES data, as estimated by *Nassar et al.* [2008], was removed prior to assimilation. For each TES profile, an expected analysis profile $\hat{\mathbf{x}}^a$ is calculated using

$$\hat{\mathbf{x}^a} = \mathbf{x}^b + \mathbf{G}(\hat{\mathbf{x}}^{obs} - \mathbf{H}(\mathbf{x}^b)), \tag{2.26}$$

where $\mathbf{x}^b$ is the background state (the GEOS-Chem profile), $\mathbf{G}$ is the Kalman gain matrix, and $\mathbf{H}$ is the TES observation operator that maps the modelled profile into the measurement space. This calculation is performed on the natural logarithm of the mixing ratio, consistent with the TES retrievals [*Bowman et al.*, 2006]. The observation operator accounts for both the a priori profile in the TES retrieval and the vertical smoothing induced by the TES averaging kernel. It is given by the following expression, which is analogous to Equation (2.25).

$$\mathbf{H}(\mathbf{x}^b) = \mathbf{x}_a + \mathbf{A}(\mathbf{x}^b - \mathbf{x}_a). \tag{2.27}$$

The error covariance on the analysis state $\hat{\mathbf{S}}$ is calculated from the Kalman gain matrix, observation operator, and forecast error $\mathbf{S}_a$ according to

$$\hat{\mathbf{S}} = (\mathbf{I} - \mathbf{GK})\mathbf{S}_a, \tag{2.28}$$

where **I** is the identity matrix. The analysis error is transported in GEOS-Chem as a passive tracer following the approach of *Ménard et al.* [2000]. As described in *Parrington et al.* [2008], the initial forecast error is taken as 50% of the the initial forecast field and horizontal correlations in the forecast error covariance matrix are neglected. The analysis increment above 100 hPa is set to zero so as to constrain only tropospheric O_3.

In *Parrington et al.* [2008], the assimilation of TES profiles reduced model biases in the free troposphere from within 30% to within 5%, as was shown in Figure 1.2. The TES assimilation was also evaluated by *Worden et al.* [2009] over North Africa, the Middle East, and Asia. They compared the TES assimilation in GEOS-Chem with assimilated ozone data from the Microwave Limb Sounder (MLS) and the Ozone Monitoring Instrument (OMI) in the GEOS-4 data assimilation system at NASA GMAO. They found that assimilation of TES data into GEOS-Chem reduced the bias in the model relative to the OMI and MLS assimilated fields at GMAO from 6.8 ppbv to 1.4 ppbv in the upper troposphere across the region. This suggested the TES assimilation provided an improved description of tropospheric ozone in the model that is consistent with the information from the OMI and MLS satellite instruments. However, TES is more sensitive in the free troposphere than it is near the surface, so applying the Kalman filter does little to resolve model biases with respect to surface measurements [*Parrington et al.*, 2009]. Additionally, the lifetime of ozone near the surface is short ($\sim$ hours) compared to the observation frequency for a particular location from TES (16 days), which means information about surface ozone brought in by the assimilation is destroyed too quickly for the assimilation to improve the model performance at the surface.

Chapter 3

Impacts of Midlatitude Precursor Emissions and Local Photochemistry on Ozone Abundances in the Arctic

3.1 Introduction

The Arctic contains a fragile ecosystem that is sensitive to changes in climate and to transported air pollution from midlatitudes [*Law and Stohl*, 2007; *Jacobson*, 2010]. Despite the paucity of local sources of O_3 precursors such as NO_x, the Arctic troposphere at times has large concentrations of O_3, which exhibit a strong seasonality. This seasonality, including a springtime maximum in the free troposphere, is poorly understood [*Monks*, 2000; *Law and Stohl*, 2007] and reflects a combination of local production, stratospheric influence, and transport from a variety of midlatitude sources of precursors, including emissions from combustion at the surface and from lightning in the upper troposphere.

Modelling studies on transport into the Arctic have traditionally focused on passive tracers [*Eckhardt et al.*, 2003], carbon monoxide [*Klonecki et al.*, 2003; *Lamarque and Hess*, 2003; *Duncan and Bey*, 2004; *Fisher et al.*, 2010], and aerosols [*Koch and Hansen*,

2005; *Stohl*, 2006]. Recent work by *Shindell et al.* [2008] presented a multi-model analysis of ozone and other gaseous species, but focused exclusively on anthropogenic sources, and did not address biomass burning, soil, or lightning emissions. Study of the loading of the Arctic troposphere with total reactive nitrogen ($NO_y = NO_x + PAN + MPAN + PPN + NO_3 + 2N_2O_5 + HNO_4 + HNO_3$, where PAN = $CH_3C(O)OONO_2$, MPAN = $CH_2{=}C(CH_3)C(O)OONO_2$, and PPN = $CH_3CH_2C(O)OONO_2$) species and their impacts on local ozone production is also lacking [*Quinn et al.*, 2008]. Measurement campaigns such as the Tropospheric Ozone Production about the Spring Equinox (TOPSE) expreriment [*Atlas et al.*, 2003] provide comprehensive composition observations, but are limited to specific seasons. The spring maximum in high-latitude tropospheric ozone and the summertime budget of ozone production are not well understood [*Law and Stohl*, 2007] and the impact of midlatitude surface emissions on Arctic pollutant abundances is contentious, with some studies finding a large midlatitude influence at the Arctic surface [*Koch and Hansen*, 2005], and others very little [*Stohl*, 2006; *Hirdman et al.*, 2010].

Trends in the Arctic over the past decade show that tropospheric ozone is increasing [*Oltmans et al.*, 2006; *Helmig et al.*, 2007; *Kivi et al.*, 2007], although changes on decadal timescales may be related to changes in the lower stratosphere [*Tarasick et al.*, 2005], or the phase of either the North Atlantic Oscillation [*Eckhardt et al.*, 2003] or the Arctic Oscillation [*Kivi et al.*, 2007]. Particulate nitrate concentrations at the surface, which correlate with PAN concentrations in the Arctic, also exhibit an increasing trend over time [*Quinn et al.*, 2007].

Previous model studies have found that the sensitivity of the Arctic surface to midlatitude anthropogenic emissions is largest in winter and spring, with Eurasian sources being the dominant influence [*Klonecki et al.*, 2003; *Eckhardt et al.*, 2003; *Wang et al.*, 2003; *Duncan and Bey*, 2004]. More recent work by *Shindell et al.* [2008] further indicates that in the Arctic mid-troposphere, ozone abundances are most sensitive to transport from midlatitudes in spring and summer, with an important contribution from East Asia.

Transport from the stratosphere into the Arctic troposphere also peaks in spring, which can provide both ozone and NO_x to the upper troposphere [*Liang et al.*, 2009, 2011].

3.1.1 Reservoirs of Total Reactive Nitrogen

While NO_x has a short atmospheric lifetime in the lower troposphere that limits its effect on ozone production to an area near to its emissions source, partitioning into long-lived reservoirs of total reactive nitrogen such as PAN and its structural analogues (that is, other species with different alkyl groups attached to the peroxyacyl and nitrate groups) permits midlatitude NO_x emissions to effect ozone production far from their sources [*Singh*, 1987]. It is illustrative to consider the total reactive nitrogen family of compounds (NO_y) as the combination of NO_x and its reservoir species, shown schematically in Figure 3.1. The principal constituents of total reactive nitrogen are NO_x, nitric acid (HNO_3), and peroxyacyl nitrates ($CH_3C(O)OONO_2$ and its analogues).

Nitric Acid

Nitric acid is highly water soluble and chemically stable. It is formed by Reaction R 1.9, and represents a sink of NO_x. Conversion of HNO_3 back into NO_x does occur, but the return reaction is a negligibly slow sink compared with other removal processes for nitric acid, in particular its scavenging by precipitation. Thus, nitric acid does not act as a nitrogen reservoir in the sense that it can release NO_x at a later time; rather, Reaction R 1.9 is essentially a terminal sink of NO_x [*Jacob*, 1999]. The exception to this is that over snow, evidence supports snowpack photolysis regenerating NO_x from deposited HNO_3 [*Thomas et al.*, 2011], producing a NO_x source similar in strength to low-emissions soils [*Honrath et al.*, 2002]. The effect of snowpack photolysis is not treated in this study.

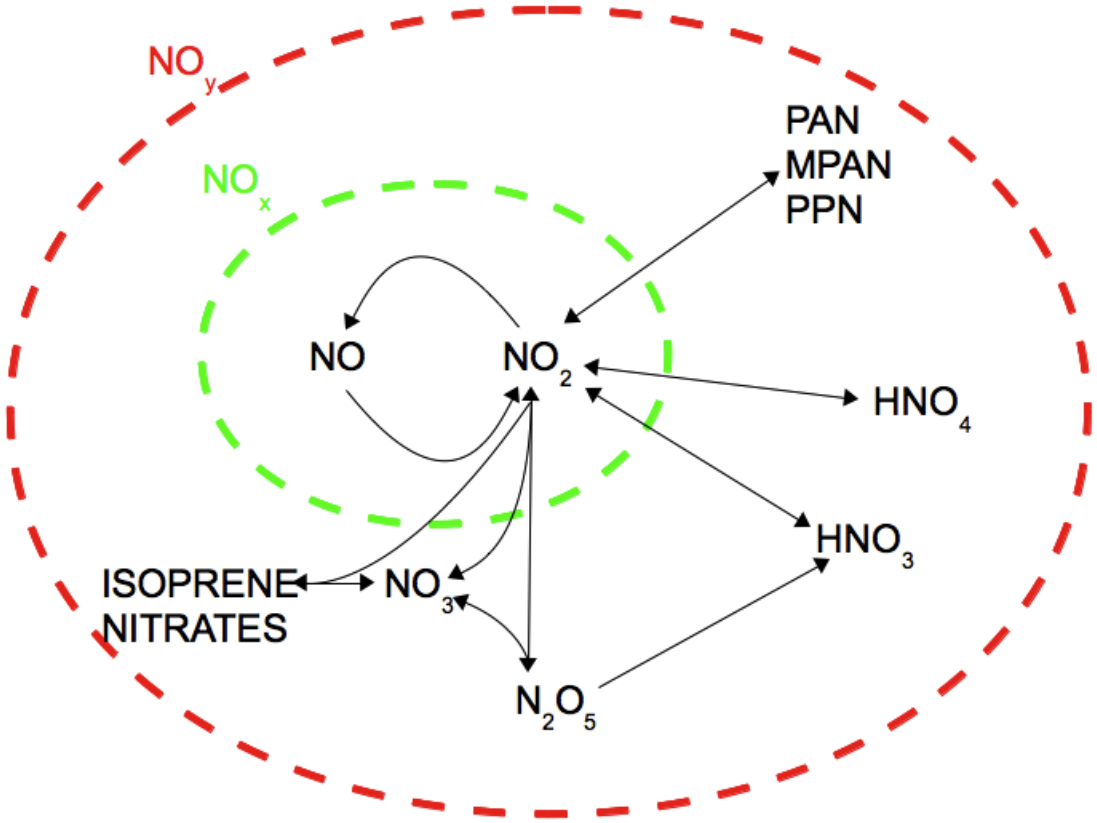

Figure 3.1: Schematic of the relationships between NO_x and the total reactive nitrogen family of compounds in the troposphere.

Peroxyacyl Nitrates

Peroxyacyl nitrates are a set of chemical analogues formed from peroxyacyl radicals in the presence of NO_x. The simplest of these can be derived from acetaldehyde (CH_3CHO):

$$CH_3CHO + OH \longrightarrow CH_3CO + H_2O \quad \text{(R 3.1)}$$

$$CH_3CO + O_2 + M \longrightarrow CH_3C(O)OO + M \quad \text{(R 3.2)}$$

$$CH_3C(O)OO + NO_2 + M \longrightarrow CH_3C(O)OONO_2 + M \cdot \quad \text{(R 3.3)}$$

The compound $CH_3C(O)OONO_2$ is PAN. Larger analogues, such as peroxypropionyl nitrate (PPN) and peroxymethacryloyl nitrate (MPAN), exist as well, with the same

structure but for the size of the alkyl chain. In a recent field campaign at midlatitudes, concentrations of the longer chain peroxyacyl nitrates were observed to reach at most 15% that of PAN [*LaFranchi et al.*, 2009].

PAN is thermally unstable at high temperatures, decomposing back into its constituent radicals, as in Reaction R 3.4:

$$CH_3C(O)OONO_2 \xrightarrow{heat} CH_3C(O)OO + NO_2 \cdot \qquad (R\,3.4)$$

At 298 K and 1 atm, the lifetime of PAN to thermal decomposition is about 35 minutes [*Tuazon et al.*, 1991]. It can also be deposited to the surface or react with another radical species, although in the latter case the products depend on the alkyl chain and where the radical attaches to the molecule [*LaFranchi et al.*, 2009].

PAN has a lifetime on the order of weeks in the cold upper troposphere, allowing it to be an effective reservoir for NO_x [*Singh*, 1987]. PAN that subsides back to the lower troposphere can then release NO_x far from its source and cause ozone production [*Moxim et al.*, 1996; *Levy et al.*, 1999], as has been observed with pollutants subsiding over the East Pacific Ocean [*Hudman et al.*, 2004; *Zhang et al.*, 2008; *Walker et al.*, 2010].

PAN can represent a large, even dominant, fraction of total reactive nitrogen. PAN itself is phytotoxic, and also has significant effects on tropospheric oxidation. Particularly, PAN dominates the NO_y budget in the Arctic [*Singh et al.*, 1992; *Bottenheim et al.*, 1993; *Talbot et al.*, 1994]. *Beine and Krojnes* [2000] found that most PAN decomposition in the Arctic occurs during the summer, and this releases a significant amount of NO_x that enhances ozone production [*Fan et al.*, 1994]. However, the effects of this decomposition on ozone production have not yet been quantified over the course of a full season.

Evidence of non-acyl peroxynitrate ($CH_3O_2NO_2$), a weakly-bound compound that acts as a reservoir at very low temperatures (<240K), was found recently in the Arctic [*Browne et al.*, 2011]. This compound was observed to modify radical partitioning in the Arctic (e.g., HO_2 to OH ratios) and reduce the amount of available NO_x. The impact

of this compound on long-range NO_x transport has not been studied, and falls outside the scope of this work.

Isoprene Nitrates

The final NO_y reservoir species we will consider is related to isoprene, which is a biogenically-emitted dialkene that oxidizes rapidly to produce a variety of organic molecules. In the presence of NO_x, these isoprene oxidation products form isoprene nitrates, which also act as a temporary reservoir for total reactive nitrogen [*Paulot et al.*, 2012]. Isoprene nitrates can transport NO_x out of the tropical boundary layer, effectively extending its lifetime, and affect the tropical upper tropospheric ozone budget [*Apel et al.*, 2012]. These compounds are of interest in regions with high biogenic emissions and significant amounts of NO_x, and will be discussed in greater detail in Chapter 4.

3.1.2 Study Outline and Goals

This study aims to understand the contributing source regions and chemical pathways that create the distribution of free tropospheric ozone and total reactive nitrogen in the Arctic. The GEOS-Chem global CTM was employed to quantify the budget of tropospheric ozone in the Arctic in summer. A specific goal was to understand the impact of long-range transport of PAN on ozone abundances in the Arctic. To address this issue, satellite observations of tropospheric ozone from TES were first used to provide an improved description of midlatitude ozone abundances in the model to better assess the fidelity of the model simulation of transport into the Arctic. The adjoint of the GEOS-Chem model was then used to characterize the sensitivity of ozone abundances in the Arctic to precursor emissions at middle and high latitudes throughout spring and summer. The study focus period is summer 2006; this period was chosen because previous studies [e.g., *Parrington et al.*, 2008; *Zhang et al.*, 2008; *Walker et al.*, 2010] have evaluated the GEOS-Chem midlatitude simulation for this period using TES data

and aircraft observations. Surface observations of PAN in the Canadian high Arctic in 2001 were also employed to evaluate the model simulation of PAN.

The determination of dominant regional influences and the processes involved in northward transport are important for effecting appropriate emissions controls and also for addressing higher-order problems, such as how the system might change as the Arctic warms, or under potential increases in shipping emissions [*Corbett et al.*, 2010]. Tropospheric ozone in the Arctic due to anthropogenic and biofuel emissions already influences surface temperatures by up to 0.4 K [*Quinn et al.*, 2008].

The following section contains a description of the observational data and modelling tools used in this study. In Section 3.3.1, observations from the TES instrument are used to assess the fidelity of the modelled transport into the Arctic. An analysis of the impact of transport of ozone from midlatitude continental source regions on the Arctic ozone budget is then presented in Section 3.3.2. In Section 3.3.3, a detailed sensitivity analysis of ozone in the Arctic to particular precursor NO_x emissions at middle and high latitudes is conducted. Finally, in Section 3.3.4, the impact of PAN transport on ozone production in the Arctic troposphere is quantified. Conclusions are presented in Section 3.4.

3.2 Observations and Modelling

3.2.1 Surface Observations

Surface observations of ozone and PAN from a high-latitude site at Alert, Nunavut, Canada (82.5°N, 62.3°W) were employed to evaluate model performance. Measurements of ozone were reported as hourly average volume mixing ratio, from a commercial instrument based on UV absorption [*Bottenheim et al.*, 2002]. PAN measurements are recorded as volume mixing ratios every half hour with a gas chromatograph instrument with electron capture detection [*Bottenheim et al.*, 1993].

Figure 3.2 shows the daily average ozone values as measured at the Alert surface station throughout 2001 (in black). Ozone accumulates during winter in the absence of photochemically-driven loss processes, reaching maximum concentrations in spring. In the spring, concentrations episodically decrease rapidly to very low values as a result of rapid ozone depletions at the surface, linked to bromine radical chemistry [*Fan and Jacob*, 1992; *Bottenheim et al.*, 2002, 2009]. In early summer, surface ozone concentrations decrease and remain low throughout the summer.

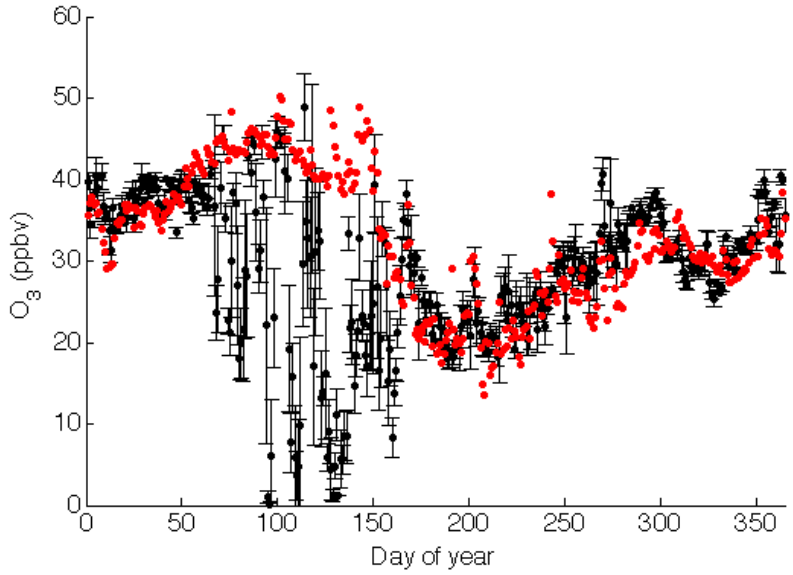

Figure 3.2: Seasonal cycle of ozone at the surface at Alert in 2001. Red symbols indicate simulated values from the GEOS-Chem baseline simulation; black symbols are daily average values of the observations. Vertical error bars represent the standard deviation in the observations over the course of the day.

3.2.2 Ozonesondes

Ozonesonde data from the WOUDC provide a source of independent observations of free tropospheric ozone. Data from high latitude sites at Eureka, Nunavut, Canada

(80.0°N, 86.4°W) and Ny-Ålesund, Norway (78.9°N, 11.9°E) from 2005 and 2006 are used to validate the simulated ozone field and gauge improvements in model performance [*Environment Canada et al.*, 2009]. Launches of ECC sondes at these sites were roughly weekly at Eureka and Ny-Ålesund, except at Eureka during the Canadian Arctic Atmospheric Chemistry Experiment (ACE) Validation Campaigns around polar sunrise [*Kerzenmacher et al.*, 2005; *Walker et al.*, 2005] and at Ny-Ålesund during stratospheric ozone loss campaigns (e.g., Match, *Rex et al.* [1998]) during winter/spring when launches were more frequent.

One representative year of observations in 2005 is shown in the top panels of Figure 3.3. Eureka launched 67 sondes and Ny-Ålesund launched 82 in 2005. The ozone values are averaged into monthly bins here. Ozone depletion near the surface appears in the Eureka sonde record in April where moderately low surface values (< 30 ppbv) persist until autumn, but in the middle and upper troposphere ozone concentrations peak in the spring. Ozone concentrations remain high at these altitudes through the summer and reach a minimum in winter.

3.2.3 GEOS-Chem Model Set-up

This study used versions v7-02-04 and v8-01-04 of GEOS-Chem to simulate Arctic ozone abundances and interpret the observations. The model is driven by assimilated meteorological fields from GEOS-4, which for global-scale simulations are degraded to the CTM horizontal resolution of $4^\circ \times 5^\circ$. Emissions of lightning NO_x are initially estimated according to *Price and Rind* [1992], with the vertical distribution prescribed by *Pickering et al.* [1998]. Anthropogenic emissions are based on the Global Emissions Inventory Activity (GEIA) [*Benkovitz et al.*, 1996] and overwritten with updated regional inventories where available [*van Donkelaar et al.*, 2008].

GEOS-Chem v8-01-04 is used for our baseline simulation and for much of the analysis presented here, whereas v7-02-04 is used for the assimilation of the TES data. GEOS-

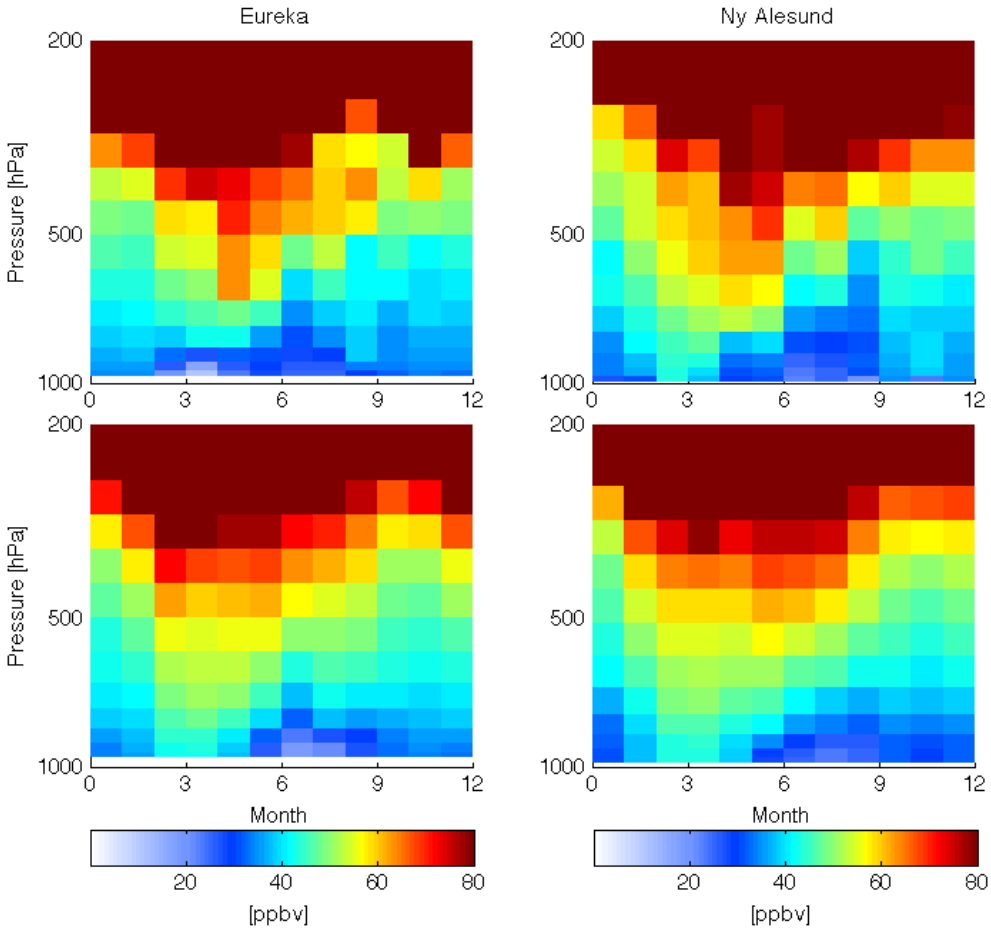

Figure 3.3: Seasonal cycle of monthly ozone profiles above Eureka (80.0°N, 86.4°W; left) and Ny-Ålesund (78.9°N, 11.9°E; right) in 2005. The upper panel shows WOUDC ozonesonde data averaged into monthly bins (67 total soundings at Eureka, 82 at Ny-Ålesund). The lower panels show the ozone values sampled at the same times and locations from the baseline simulation (v8-01-04) in GEOS-Chem.

Chem v8-01-04 corrects a problem with excessive stratosphere-troposphere exchange near the polar tropopause. The impact of this change is small in the Northern Hemisphere summer, when stratosphere-troposphere exchange has a smaller influence compared to winter or spring. GEOS-Chem v8-01-04 also incorporates a significant improvement to the global horizontal distribution of lightning NO_x emissions, in which the estimated distribution of lightning flashes is scaled to resemble that observed by OTD-LIS [*Sauvage et al.*, 2007; *Murray et al.*, 2012], which was also discussed previously in Chapter 2.

The two model versions also have significant differences in their anthropogenic and biomass burning emissions inventories. Anthropogenic emissions in v7-02-04 of GEOS-Chem use the GEIA inventory. GEIA is overwritten in the United States by the Environmental Protection Agency National Emission Inventory (EPA/NEI99), modified according to *Hudman et al.* [2007]. Global anthropogenic emissions are scaled to the simulation year or as far as 1998 according to fuel consumption statistics [*Bey et al.*, 2001]. Biomass burning emissions are monthly averages derived from a four-year climatology of remote sensing data [*Duncan et al.*, 2003]. A summary of the differences in the precursor emissions between the two models is given in Table 3.1.

In v8-01-04, global anthropogenic emissions are from the Emission Database for Global Atmospheric Research (EDGAR, v3.2, *Olivier and Berdowski* [2001]) for NO_x, CO, and SO_2. The global inventory is overwritten by regional inventories over the United States (EPA/NEI99 with modifications by *Hudman et al.* [2007]), Europe (EMEP, *Vestreng and Klein* [2002]), East Asia (Streets, *Streets et al.* [2003] and *Streets et al.* [2006]), Mexico (BRAVO, *Kuhns et al.* [2005]), and Canada (CAC, Environment Canada, see http://www.ec.gc.ca/pdb/cac/cac_home_e.cfm). Global emissions are scaled forward to the simulation year or as far as 2005 according to more recent fuel consumption statistics [*van Donkelaar et al.*, 2008]. Biomass burning emissions in v8-01-04 use the GFED2 emissions inventory [*van der Werf et al.*, 2006]. Simulations in this study use emissions

Table 3.1: Description of simulations performed with the GEOS-Chem model.

Simulation	Version	Description
Baseline	v8-01-04	Lightning NO_x emissions use regional OTD-LIS scaling. Surface emissions from EDGAR are overwritten by recent regional emission inventories (EMEP, Streets 2006, NEI99, CAC, BRAVO). Biomass burning emissions from GFED2.
Old emissions	v8-01-04	Lightning NO_x emissions use regional OTD-LIS scaling. Surface emissions from GEIA are overwritten with NEI99. Biomass burning emissions from *Duncan et al.* [2003].
No PAN	v8-01-04	Same emissions as baseline run, but with conversion between NO_x and PAN turned off.
TES assimilation	v7-02-04	Lightning NO_x emissions are not scaled to OTD-LIS. Surface emissions from GEIA are overwritten with NEI99. Biomass burning emissions from *Duncan et al.* [2003]. Assimilation of TES O_3 and CO profiles equatorward of 60° latitude.
Assimilation control	v7-02-04	Same emissions as assimilation run, but with assimilation turned off.
Tagged Ox	v8-01-04	Same emissions as baseline run.

and meteorology specific to the year the observations to which we are comparing were taken. Table 3.2 shows the total NO_x, CO, and VOC emissions for 2006.

Table 3.2: Emissions from anthropogenic source inventories used in GEOS-Chem. The 'Old emissions' and 'Baseline' rows give global total anthropogenic NO_x, CO, and VOC emissions from those simulations, including any regional inventories used. Regional inventories overwrite the global inventories as described in the text. Changes in regional emissions are shown relative to the 'Old emissions' simulation. A negative change indicates that emissions are lower in the 'Baseline' simulation. Values are derived from emissions from April 2006 applied throughout the entire year.

Inventory	Domain	NO_x [Tg N/yr]	CO [Tg C/yr]	VOC [Tg C/yr]
Old emissions (GEIA)	global	24.0	142.2	47.4
Baseline (EDGAR)	global	27.1	188.3	48.2
EPA/NEI99	USA	−1.2	−1.8	−0.3
CAC	Canada	+0.1	−0.4	−0.3
BRAVO	Mexico	−0.1	−0.4	−0.1
EMEP	Europe	+0.5	−12.4	−5.0
Streets	East Asia	+3.1	+56.7	+4.5

Version v8-01-04 of GEOS-Chem (the baseline simulation) reproduces well many of the observed features of the Arctic ozone distribution. Figure 3.2 compares a year of ozone mixing ratios at Alert in 2001 to the daily averaged modelled values. Error bars represent the standard deviation of the hourly measurements and capture the variability over the course of each day. GEOS-Chem simulates well the seasonal cycle of ozone, capturing the build-up of concentrations throughout winter as well as the summer minimum. In the spring, observations of ozone fall to low values as a result of rapid ozone loss at the surface due to the previously mentioned catalytic destruction by bromine radicals [*Fan*

and Jacob, 1992; *Bottenheim et al.*, 2002, 2009]. The version of GEOS-Chem used in this study does not include these bromine reactions in its chemical mechanism, and thus the model does not capture the low ozone values in spring. Excluding the springtime ozone observations yields a model bias relative to the ozone measurements of −1.1 ppbv (−4%). Figure 3.3 shows a comparison between the model and ozonesonde measurements above Eureka and Ny-Ålesund in 2005. Although the focus of our analysis is on summer 2006, we compare the model simulation here with ozonesonde data from Eureka and Ny-Ålesund in 2005 because the more complete data record at Ny-Ålesund in 2005 enables us to better examine the model simulation over the seasonal cycle. The model captures the free-tropospheric maximum in the spring, but the maximum occurs earlier in spring and is broader in the model. In summer, the model slightly underestimates the ozone abundances in the mid-troposphere, with mean summertime biases around 500 hPa of 11% above Eureka and 5% above Ny-Ålesund. In Section 3.3.2, the seasonal dependence of the impact of the midlatitude source regions on ozone at Eureka and Ny-Ålesund is examined.

3.2.4 Adjoint Model Set-up

The adjoint of the GEOS-Chem model was previously described in Section 2.2.3. The adjoint model is a computationally-efficient tool for calculating the gradient of model outputs to model inputs, which can be interpreted as a measure of sensitivity of said output to variations in said input. Using the GEOS-Chem adjoint model, we perform a set of adjoint simulations to probe the sensitivity of ozone concentrations above Alert to emissions of NO_x from various sources. Simulations are performed to calculate sensitivities of ozone abundances in both the lower (surface to 850 hPa) and middle (850 to 500 hPa) troposphere above Alert in the first two weeks of each month from April to August 2006. The resulting sensitivities represent the fractional change in the ozone

concentration above Alert due to a unit change in the emissions in each model grid box. Adjoint model results are presented in Section 3.3.3.

3.3 Results and Discussion

3.3.1 Evaluation of Transport of Ozone into the Arctic in GEOS-Chem

TES ozone data is assimilated into GEOS-Chem to evaluate the model simulation of ozone transport into the Arctic. The assimilation system is described in *Parrington et al.* [2008] and was reviewed in Chapter 2. It is based on version v7-02-04 of GEOS-Chem and employs a suboptimal sequential Kalman filter which ingests the TES profiles of tropospheric ozone in a 6-hour analysis cycle along the TES orbit track. TES data are assimilated during July and August 2006, equatorward of 60°N. As shown in Figure 3.4, the assimilation significantly increases the ozone abundance throughout the free troposphere in the extratropics, compared to the control run without TES assimilation (referred to as the "assimilation control"). Since the TES assimilation strongly constrains the distribution of midlatitude ozone, the meridional transport into the Arctic in the model can be validated by assimilating TES data outside the Arctic to provide a midlatitude boundary condition for ozone.

As seen in Figure 3.4, the TES assimilation shows large increases in ozone in the Arctic relative to the assimilation control run, even though no TES data were ingested into the assimilation poleward of 60°N. Figure 3.5 compares the mean vertical profiles of ozone from the baseline (green), assimilation (red), and assimilation control (blue) runs at Eureka and Ny-Ålesund from July to August. The mean model bias below 300 hPa relative to the ozonesondes is reduced from −9.9 ppbv (−18%) in the assimilation control run to −3.5 ppbv (−7%) at Eureka with the TES assimilation, and from −9.4 ppbv

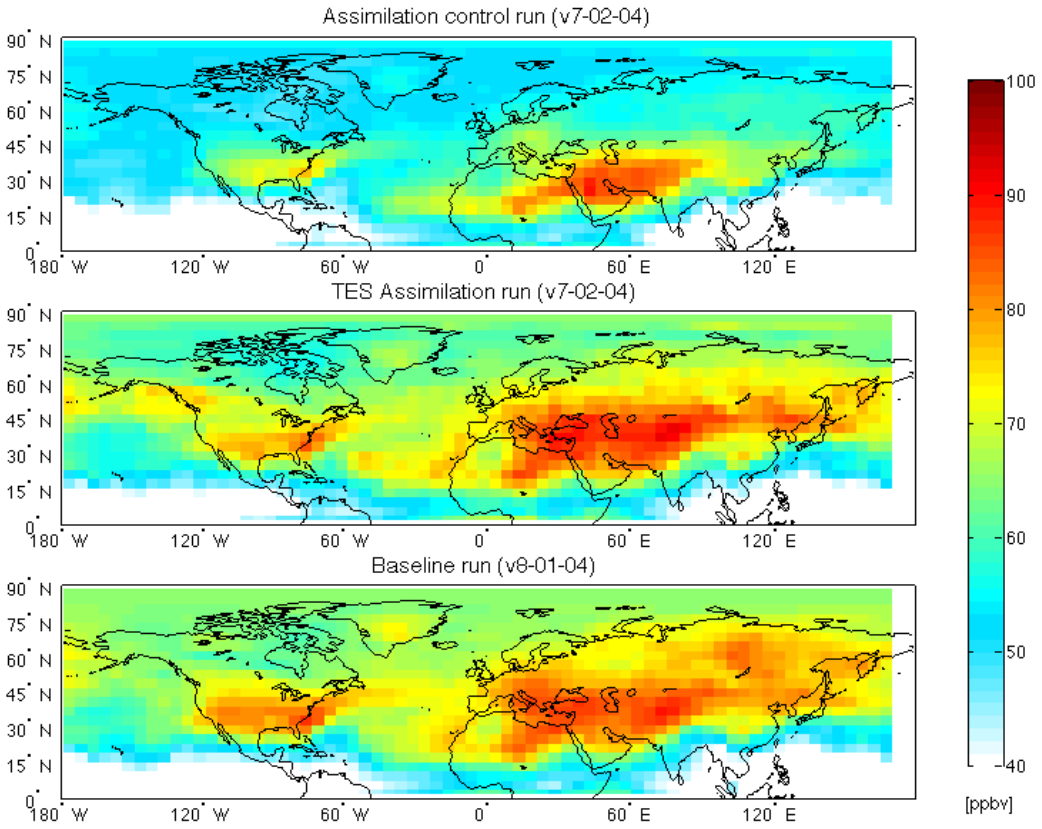

Figure 3.4: Monthly mean ozone concentrations for July 2006 in the middle troposphere (model level 9, approximately 450 hPa) for the assimilation control (top) and TES assimilation (middle) runs in v7-02-04, and for the baseline simulation in v8-01-04, without data assimilation (bottom). The difference between the top two panels shows the impact of assimilating TES ozone profiles.

(−18%) to −2.4 ppbv (−6%) at Ny-Ålesund. The concentrations near the surface at these two sites show little change with the assimilation. The agreement with the TES assimilation and the ozonesondes in the Arctic suggests that the meteorological fields driving the model (which are the same in v7-02-04 and v8-01-04) provide an unbiased description of transport into the Arctic.

Figure 3.4 also demonstrates that ozone in the baseline simulation (v8-01-04 without assimilation) compares well with the TES assimilation. In the middle troposphere of the midlatitudes, between 20°–50°N, the mean difference in ozone between the two model simulations is 0.9 ppbv. The high latitude ozone distribution in the baseline simulation is also consistent with the TES assimilation, as are the ozonesonde observations, as seen in Figure 3.5. The differences in the mean abundance of ozone in the Arctic summer between the baseline simulation and the TES assimilation are less than 5%. The agreement between the baseline simulation and the TES assimilation in the Arctic suggests that the baseline model is providing a reliable description of transport of midlatitude ozone into the Arctic. This gives us confidence that the tagged ozone analysis presented below gives a meaningful assessment of the impact of the midlatitude source regions on Arctic ozone abundances.

Parrington et al. [2008] and *Jourdain et al.* [2010] suggested that the underestimate of ozone in the assimilation control run is due mainly to an underestimate of lightning NO_x emissions in v7-02-04 of GEOS-Chem. To assess the extent to which the improvements seen in Figure 3.4 are due to the changes in the lightning NO_x source, we ran version v8-01-04 of GEOS-Chem with the same surface emissions as in v7-02-04, but kept the OTD-LIS scaling of the lightning NO_x emissions. This run is labeled "Old emissions" in Table 3.1. Table 3.3 shows that the increases in ozone in July 2006 obtained with the TES assimilation relative to the assimilation control run are comparable in the middle (400-750 hPa) and upper (above 400 hPa) troposphere to those increases obtained with the improved lightning NO_x source (the main difference between the old emissions and

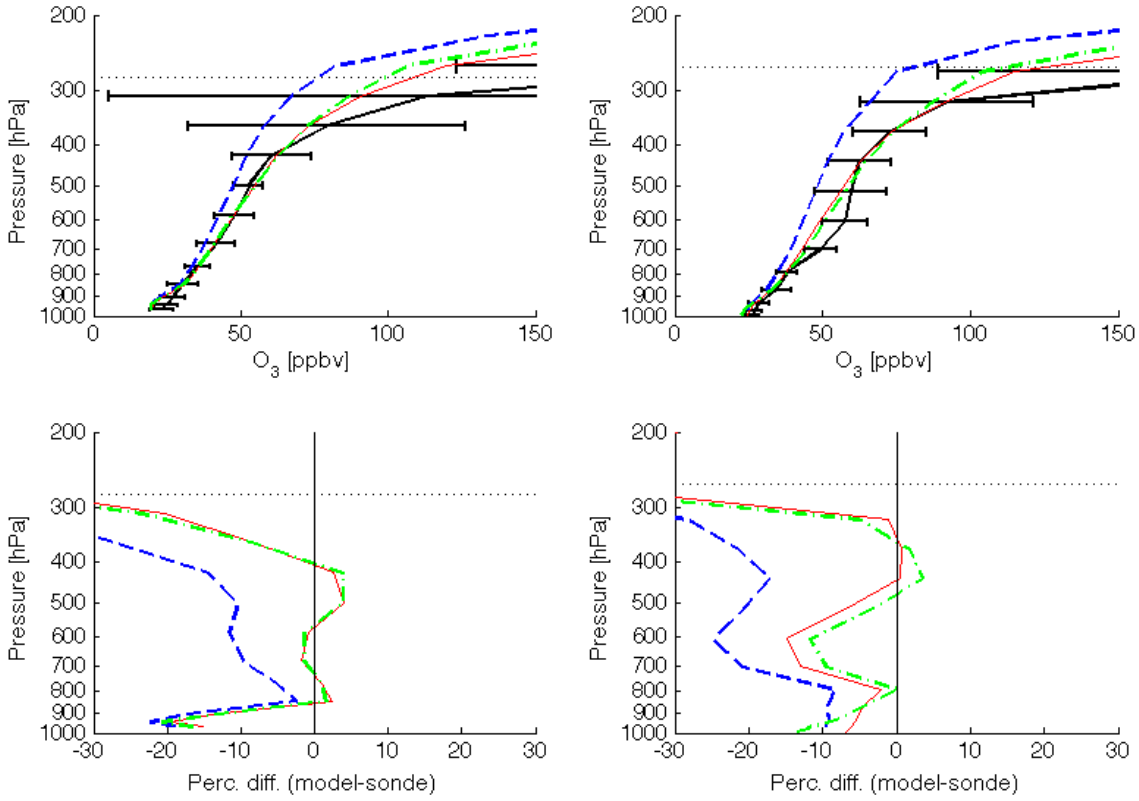

Figure 3.5: Vertical profiles of mean ozone mixing ratio for July–August 2006 above Eureka (left) and Ny-Ålesund (right). Ozonesonde observations are shown in black, with error bars showing the standard deviation of the observations. Values from GEOS-Chem v7-02-04 without assimilation are shown with a dashed blue line (assimilation control simulation). Values from the assimilation run are shown with a thin red line, and values from v8-01-04 (baseline simulation) are shown with a dash-dotted green line. The horizontal dotted black line denotes the mean tropopause pressure for this period. Percent differences are calculated with respect to the observations.

assimilation control runs). In the middle and upper troposphere, the TES assimilation increased ozone by 14% and 33%, respectively, whereas the new lightning NO_x source enhanced ozone by 19% and 33%, respectively. This suggests that in the free troposphere, the TES assimilation is indeed largely correcting the underestimate in midlatitude ozone due to the lightning precursor emissions in v7-02-04.

Table 3.3: Differences in the mean ozone concentrations in July 2006 north of 60°N in the lower (LT; surface to 750 hPa), middle (MT; 750 to 400 hPa), and upper (UT; 400 hPa to tropopause) troposphere between pairs of forward model sensitivity simulations. Percent differences are calculated with respect to the mean of the two simulations.

Simulations	Arctic LT	Arctic MT	Arctic UT
TES assim. − assim. control	1.0 ppbv, 3.5%	6.6 ppbv, 13%	21 ppbv, 28%
Old emissions − assim. control	2.0 ppbv, 6.9%	9.1 ppbv, 17%	21 ppbv, 28%
TES assim. − baseline	0.8 ppbv, 2.9%	−2.9 ppbv, −5.2%	−0.1 ppbv, −0.1%
Baseline − no PAN	1.8 ppbv, 6.5%	−1.1 ppbv, −1.9%	−3.4 ppbv, −3.9%

3.3.2 Impact of Midlatitude Continental Source Regions on Arctic Ozone

A tagged ozone analysis was conducted to quantify the contribution of ozone from midlatitude continental source regions to the budget of ozone in the Arctic. Separate tracers are used for O_x produced in the different source regions shown in Figure 3.6. The Arctic region shown in Figure 3.6 includes everything north of 60°N, including parts of northern Canada, Scandinavia, and Russia.

Figures 3.7 and 3.8 show the fractional contribution to the simulated ozone distribution above Eureka and Ny-Ålesund, respectively, from the six regions (the stratosphere,

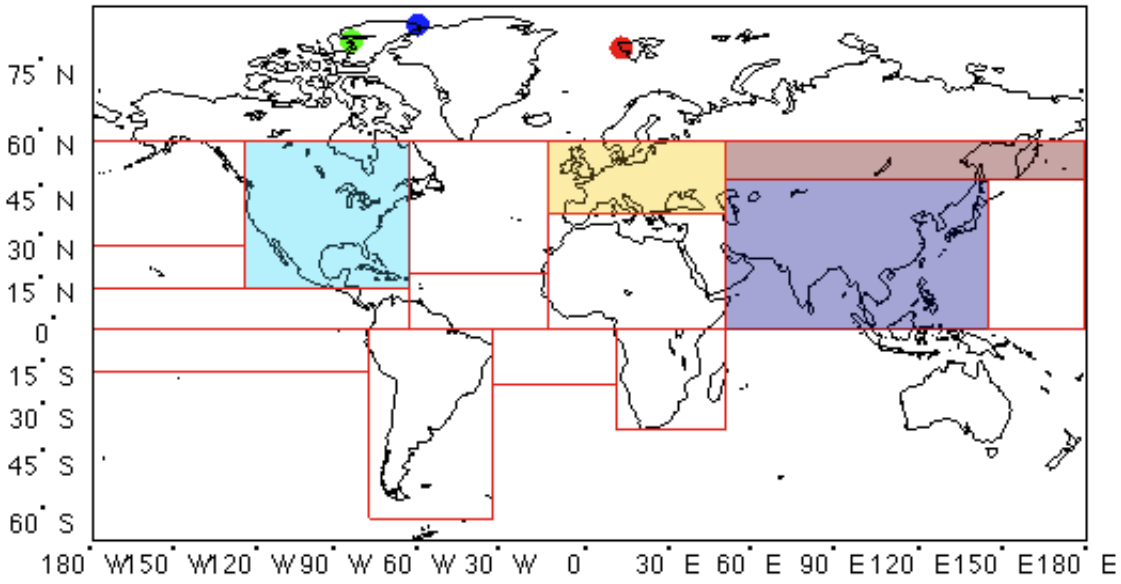

Figure 3.6: Region definitions for tagged ozone simulation. Midlatitude regions discussed in Figures 3.7 and 3.8 are coloured: Asia in purple, North America in blue, Europe in yellow, and Siberia in pink. The Arctic region is defined as everything poleward of 60°N. The red, blue, and green dots indicate the locations of Ny Ålesund, Alert, and Eureka, respectively.

Asia, Europe, North America, Siberia, and the Arctic) that represent the dominant contributions to the ozone budget. Transport from other source regions provides contributions of less than 5% and is not examined here. The corresponding total ozone distributions at these sites are shown in the bottom panels of Figure 3.3.

The stratospheric tracer has its maximum influence at Eureka in early spring, and its contribution increases with altitude. Little stratospheric influence reaches the surface in the summer and autumn, consistent with Lagrangian studies of stratospheric influence at Arctic surface sites [*Stohl*, 2006; *Hirdman et al.*, 2010]. However, analysis of long-term ozonesonde records in the Arctic show statistically significant correlations in ozone anomalies that link the lower stratosphere to the troposphere all the way to the sur-

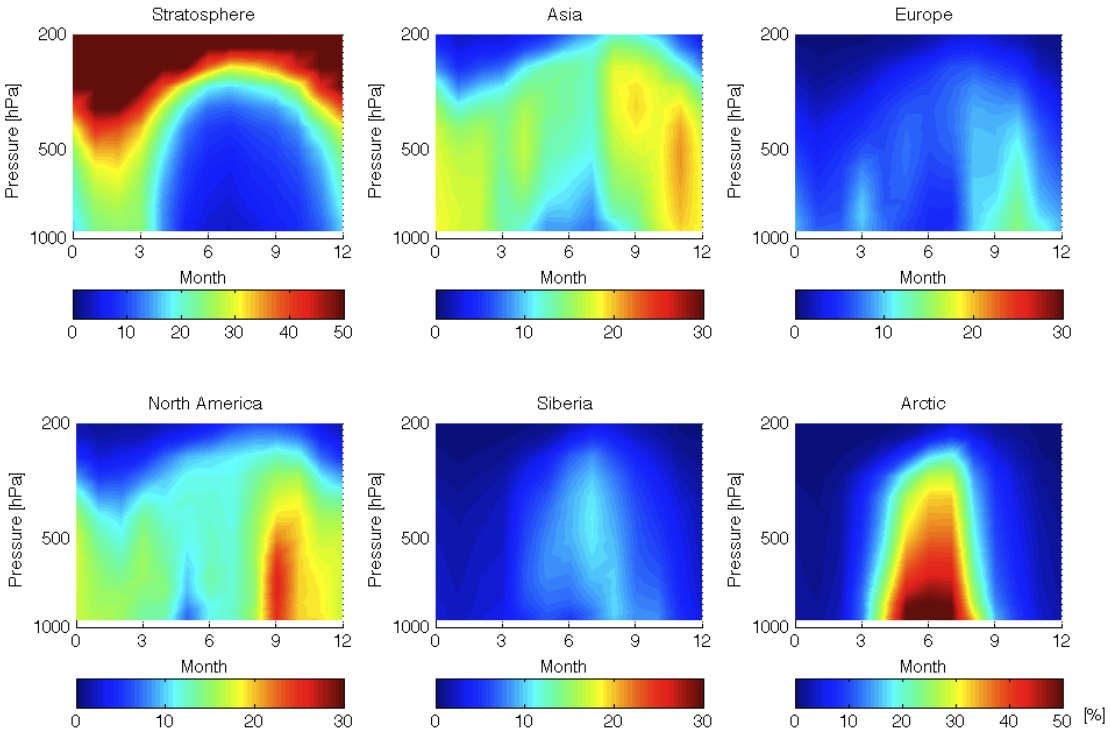

Figure 3.7: Percent contribution to ozone profile above Eureka in 2006 due to ozone produced in the stratosphere, and in the lower troposphere over Asia, Europe, North America, Siberia, and the Arctic. The contributions were estimated using the tagged ozone simulation, in which separate tracers are specified for ozone produced in each of the source regions shown in Figure 3.6.

face [*Tarasick et al.*, 2005]. It was suggested by *Terao et al.* [2008] that the correlations in the observational record could reflect variations in large-scale subsidence down into the Arctic lower troposphere.

The European, North American, and Asian relative contributions maximize in spring and fall when intercontinental transport is most active [*Stohl*, 2001; *Fiore et al.*, 2009]. In summer, transport times to the Arctic are longer, and air transported to the Arctic from midlatitudes will climb along isentropic surfaces that rise with latitude, effectively isolating the Arctic lower troposphere [*Stohl*, 2006]. As a result, only high-latitude sources in

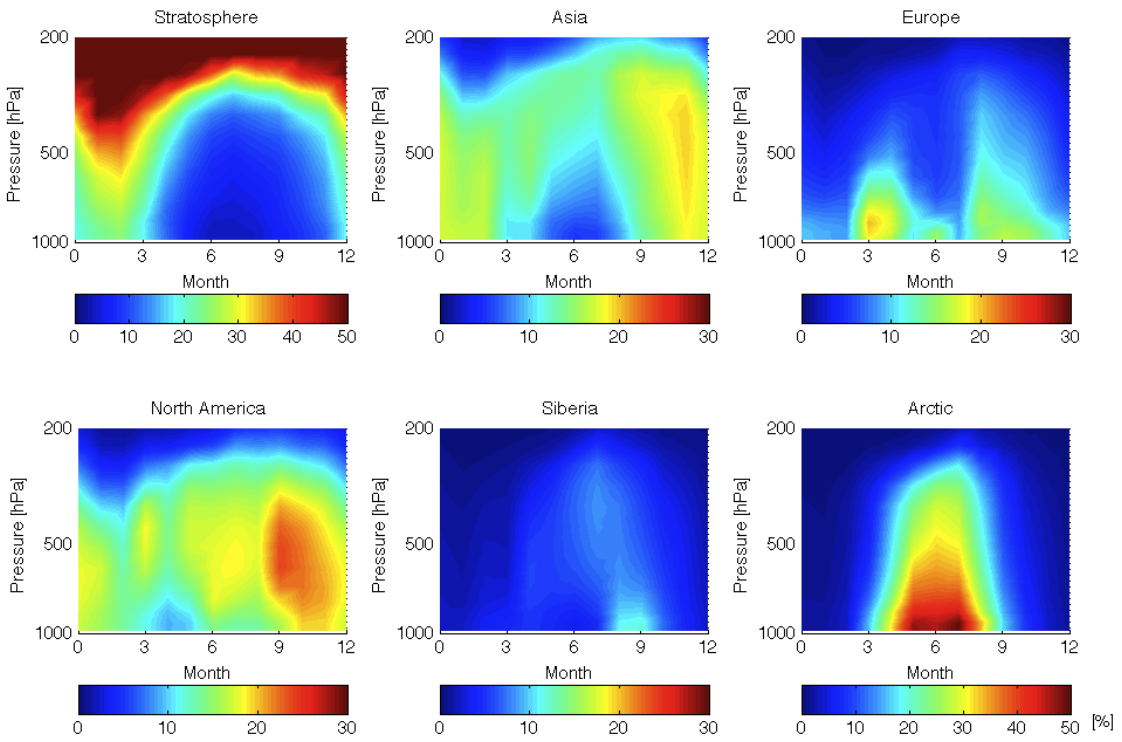

Figure 3.8: Same as Figure 3.7, only for the ozone profile above Ny-Ålesund.

regions such as Siberia, Europe, and North America are expected to have much influence on surface ozone abundances in the Arctic. Pollutants transported from lower latitudes will influence the Arctic at higher altitudes [*Eckhardt et al.*, 2003]. Consequently, we find that the Asian contribution (mainly from East Asia) in the Arctic troposphere in summer is larger in the upper troposphere. Over both Eureka and Ny-Ålesund, the Asian contribution is less than 10% throughout the troposphere, but the influence is greater over Eureka than over Ny-Ålesund. *Stohl* [2006] identified three pathways for transport to the lower Arctic troposphere: low-level lateral transport, fast low-level transport followed by ascent in the Arctic, and ascent outside the Arctic followed by lateral transport, then descent inside the Arctic. Emissions from northern source regions such as Europe and from boreal fires have access to the first pathway [*Stohl et al.*, 2007], which can be especially efficient during the positive phase of the North Atlantic Oscillation (NAO) [*Eckhardt*

et al., 2003; *Stohl et al.*, 2007]. However, the NAO was negative in the winter of 2006, so this transport may have been suppressed relative to the interannual mean [*Osborn*, 2006]. Asian pollutants begin at a higher potential temperature, and so have access mainly to the third pathway which can take 15–20 days.

In summer at Eureka (Figure 3.7) the European influence is small, less than 8% throughout the troposphere. Transport from North America and local production in the Arctic provide the dominant contributions to local ozone abundances. Over Ny-Ålesund (Figure 3.8) European sources have a much stronger influence. The North American and European sources each account for about 10–15% of the ozone abundances at the surface at Ny-Ålesund in summer, with a slightly larger contribution from Europe. The greater European influence at the surface at this site is consistent with previous studies that also found fast low-level transport from continental Europe to the Arctic [*Duncan and Bey*, 2004; *Stohl*, 2006]. However, the European contribution is confined to the lower troposphere, whereas the North American influence extends into the middle troposphere.

The distribution of midlatitude source region contributions to ozone at Arctic stations calculated here displays many similar features to a multi-model assessment of the anthropogenic impact of industrialized regions of Arctic pollutants [*Shindell et al.*, 2008]. Whereas the *Shindell et al.* [2008] assessment evaluates the response to a known perturbation to individual source regions, we track the total contribution from each region in a simulation that reproduces Arctic observations of ozone and PAN. At the surface, *Shindell et al.* [2008] find the greatest sensitivities to North American and European sources of ozone except during the summer when European sources are more significant. This is reflected in our distribution above Ny-Ålesund, where the European influence during the summer is larger than all other midlatitude source regions, peaking at 20%. In *Shindell et al.* [2008], the largest sensitivities in the Arctic upper troposphere were to Asian and North American sources, and we also observe contributions up to 20% of the total abundance from Asia in the upper troposphere above both sites.

Ozone produced within the Arctic is limited to the sunlit summer months. At Eureka and Ny-Ålesund, this local source accounts for more than 50% of the ozone in the lower troposphere and as much as 30–40% of the ozone in the middle troposphere. As mentioned above, this production is driven mainly by precursor emissions at high latitudes. Below, the adjoint of the GEOS-Chem model is used to examine in greater detail the sensitivity of this local ozone source to emissions of NO_x, a key ozone precursor.

3.3.3 Sensitivity of Arctic Ozone to NO_x Emissions

The adjoint model of GEOS-Chem is used to calculate the sensitivity of ozone in either the lower or middle troposphere above Alert to monthly mean NO_x emissions. A separate adjoint simulation is performed for the first two weeks of each month between April and August 2006. Sensitivities are calculated for every model grid box, and represent the fractional change that would occur in ozone above Alert for a fractional change in the emissions in a particular grid box. This approach rapidly provides detailed information about which types of emissions and which locations are impacting a particular site at a particular time.

Figure 3.9 shows maps of the sensitivities calculated by the adjoint model to NO_x emissions from fossil fuel combustion, biomass burning, lightning, and soils. The left panels show the sensitivity of ozone in the middle troposphere (850–500 hPa) above Alert in the first two weeks of June 2006. The panels on the right show the sensitivities of ozone at the same location in the first two weeks of July 2006. Recall from Equation 2.24 that if the sensitivity at a particular location is λ_{ij}, and the emissions at that location were changed by a fractional amount α, then the fractional change in the cost function (here, the O_x abundance in the middle troposphere above Alert) will be $\alpha\lambda_{ij}$. Because the sensitivities reflect the influence of atmospheric transport, the maps depend somewhat on the synoptic conditions during the chosen two-week simulation periods. In the first two weeks of June, North America (mainly western Canada) was the dominant source region

for NO_x emissions that influenced ozone abundances over Alert. In particular, ozone over Alert was most sensitive to anthropogenic and biomass burning emissions from northern Alberta. The greatest sensitivity to emissions in Eurasia was to anthropogenic emissions from western Russia and Scandinavia. In contrast, in the first two weeks of July, ozone abundances over Alert were most sensitive to NO_x emissions from biomass burning and lightning in central Russia. There was weaker sensitivity to NO_x emissions from soils in central Russia and from fossil fuel combustion in Scandinavia and the United Kingdom.

To better compare the relative importance of the different sources of NO_x, the zonally summed sensitivities for ozone in the lower (surface to 850 hPa) and middle (850–500 hPa) troposphere over Alert in the first two weeks of June, July, and August 2006 are shown in Figure 3.10. Ozone abundances in the lower troposphere at Alert are most sensitive to changes in NO_x emissions between 55°–70°N. Throughout summer there was strong sensitivity to fossil fuel emissions at these latitudes, with comparable sensitivity to soil emissions near 70°N. The sensitivity to biomass burning emissions peaks in July and is comparable to that for fossil fuel emissions near 60°N. The peak in biomass burning in July most likely reflects the influence of transport. Estimates of biomass burning in the northern midlatitudes for 2006 total 244 Tg C $year^{-1}$, less than the 12-year average (298 Tg C $year^{-1}$) [*van der Werf et al.*, 2010]. In the middle troposphere, ozone was most sensitive to anthropogenic NO_x emissions between 50°–60°N, but in July the sensitivity to emissions from lightning and biomass burning increased, and biomass burning emissions near 60°N had the greatest influence on the ozone abundances. By August, the greatest sensitivity in the middle troposphere was to anthropogenic emissions outside the Arctic, between 50°–55°N, and to lightning emissions within the Arctic, between 65°–70°N.

When interpreting Figures 3.9 and 3.10, it is important to note that the sensitivity analysis is only as accurate as the ozone simulation in GEOS-Chem. If our knowledge of the distribution of the ozone precursor emissions is incomplete, or if there are missing

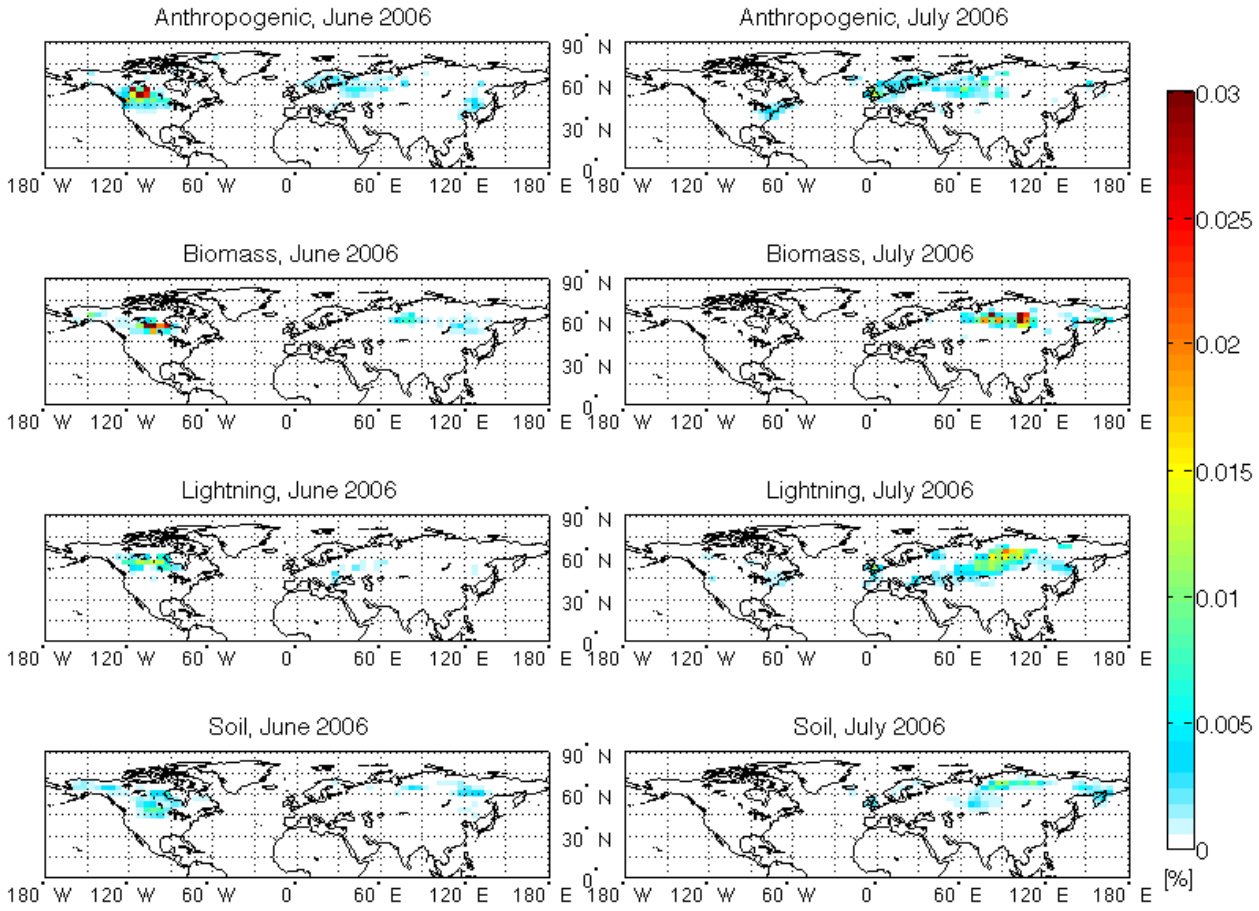

Figure 3.9: Example maps of the sensitivity of O_x concentration in the middle troposphere (850–500 hPa) above Alert to various types of NO_x emissions. From top to bottom, the panels show the sensitivity to anthropogenic, biomass burning, lightning, and soil NO_x emissions. Sensitivities are shown for the first two weeks of June (left column) and July (right column) of 2006. The colour scale indicates the fractional amount by which O_x in the middle troposphere above Alert would change in response to a perturbation in emissions at a particular location.

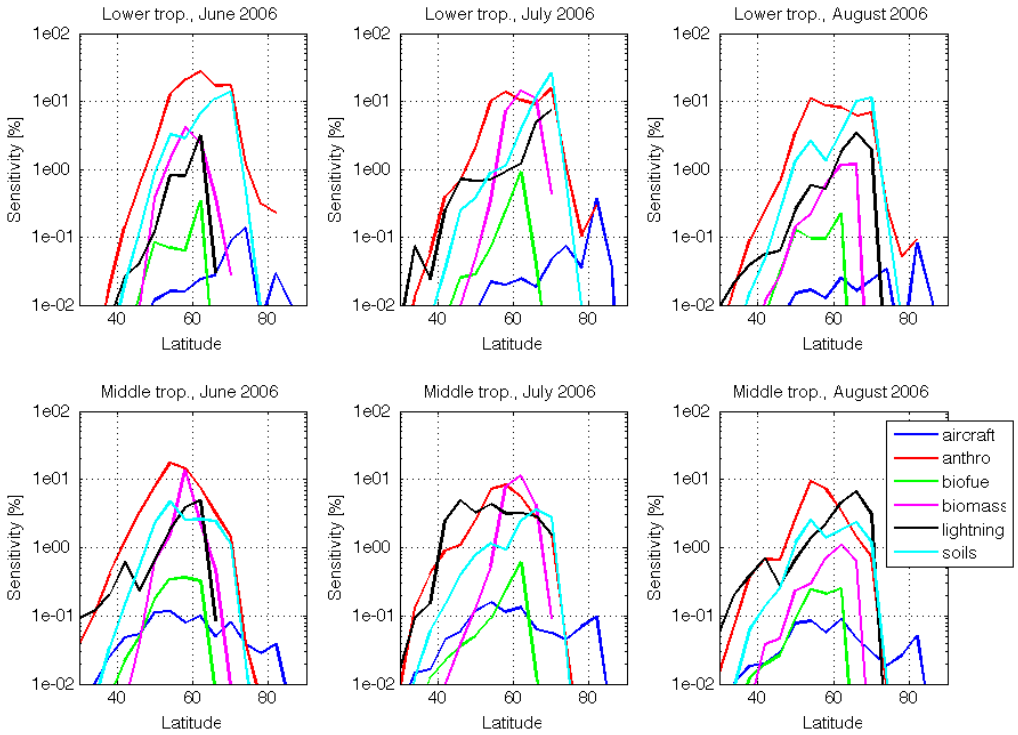

Figure 3.10: Sensitivity of O_x in percent in the lower (top row) and middle (bottom row) troposphere above Alert to various sources of NO_x precursor emissions, summed zonally. Sensitivities are shown for the first two weeks of June (left), July (middle), and August (right) of 2006.

processes in the chemical mechanism in the model, the sensitivity analysis will be biased. Also, the adjoint model relies on a linearization around the model state, and cannot calculate sensitivities with respect to emissions that do not exist in the model. However, the good agreement between the surface observations and the modelled ozone abundances at Alert (shown in Figures 3.2 and 3.3) suggests that the model is providing a reliable description of the main processes controlling the ozone distribution. Our analysis indicates that on synoptic timescales the local ozone source in the Arctic shown in Figures 3.7 and 3.8 reflects mainly the influence of anthropogenic and soil emissions of NO_x in the

Arctic, together with more variable contributions from biomass burning and lightning at high latitudes. On longer timescales, the region to which ozone at Alert is sensitive extends further equatorward, and because different source regions may be included in the region of influence, the relative importance of the different emissions types may change.

3.3.4 Impact of PAN Decomposition on Ozone Production in the Arctic

Local production of ozone in the summertime Arctic lower troposphere accounts for more than 50% of the ozone budget, but emissions of ozone precursors at high latitudes are small. The release of NO_x from the decomposition of PAN, which acts as a long-lived reservoir for NO_x, is thought to enhance ozone production in the Arctic summer [*Fan et al.*, 1994; *Beine and Krojnes*, 2000]. Long-range transport of PAN from lower latitudes, therefore, enables the displacement of the ozone-producing capacity of NO_x over long distances [*Singh*, 1987; *Singh et al.*, 1992; *Fan et al.*, 1994]. Here, the impact of NO_x from PAN decomposition on the ozone budget is examined. This impact is isolated by comparing the baseline run with a simulation of GEOS-Chem with the PAN to NO_x interconversion turned off. Turning off this reaction allows us to separate the influence of this transport pathway (by taking the difference with the baseline run) in a similar way to determining the influence of an emissions source by turning off that emissions source in the model and comparing to the baseline simulation [*Moxim et al.*, 1996; *Levy et al.*, 1999; *Walker et al.*, 2010].

The baseline simulation gives a good representation of PAN at the surface in the Arctic. Figure 3.11 shows a year of PAN daily mean mixing ratios measured at Alert in 2001 compared to the values in the baseline simulation. PAN data from this site were only available until 2001, so simulations with emissions appropriate to that year were used for this comparison. PAN concentrations are at a minimum in the summer and increase throughout the dark winter. PAN concentrations also fall precipitously from

their spring maximum to very low values that persist through the summer, which is consistent with the seasonal cycle observed in the European Arctic [*Beine and Krojnes*, 2000]. Agreement between modelled and observed PAN is good, with a mean model bias in the daily average PAN concentrations of −5.4 pptv (−5%).

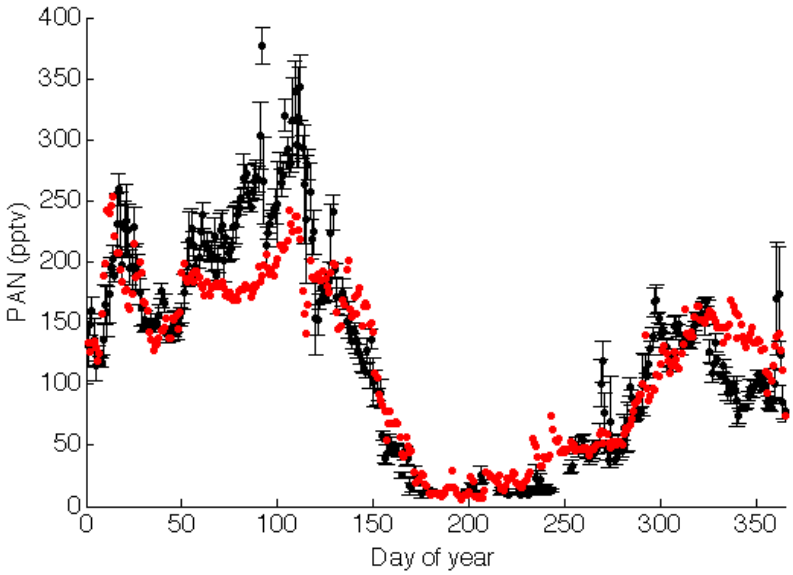

Figure 3.11: Seasonal cycle of PAN at the surface at Alert in 2001. Red symbols indicate simulated values from the GEOS-Chem baseline simulation; black symbols are daily average values of the observations. Vertical error bars represent the standard deviation in the observations over the course of the day.

A number of observations suggest that peroxyacyl nitrates (PAN + MPAN + PPN) constitute the largest fraction of total reactive nitrogen (NO_y) in the Arctic lower troposphere [*Singh*, 1987; *Bottenheim et al.*, 1993] and at higher altitudes as well [*Talbot et al.*, 1994; *Alvarado et al.*, 2010]. Qualitatively, GEOS-Chem reproduces this aspect of the NO_y budget, although recent aircraft observations suggest that the partitioning between nitric acid and PAN in GEOS-Chem is biased (e.g. *Hudman et al.* [2007]; *Walker et al.* [2010]; *Alvarado et al.* [2010]). *Hudman et al.* [2007] compared the model to air-

craft observations of PAN over North America in summer and found that the model reproduced well the data in the lower troposphere, but underestimated abundances in the upper troposphere by about 30%. *Alvarado et al.* [2010] examined NO_x and PAN abundances in boreal fire plumes and found that the model PAN accounted for as much as 45% of the NO_y in the fresh plumes, but the model overestimated the HNO_3 to PAN ratio relative to the observations, even after correcting the partitioning at the biomass burning source. *Alvarado et al.* [2010] suggested that either the simulated emissions of acetaldehyde, an important PAN precursor, are too low, that the biomass burning emissions are injected at too low an altitude in the model, or that the simulated scavenging of nitric acid is underestimated. *Millet et al.* [2010] used remote sensing constraints in GEOS-Chem to estimate a global source of acetaldehyde four times greater than is used here, but with a large uncertainty in the ocean exchange. Nitric acid is often overestimated in global models such as GEOS-Chem, and insufficient scavenging is thought to be the reason [*Bey et al.*, 2001]. However, for the purposes of this study, the ability of the model to reproduce many of the features in the year-long PAN and ozone observations at Alert lends confidence that the ozone production in the lower troposphere described here does not depend on the exact partitioning of NO_y in the upper troposphere in the model.

The top panel of Figure 3.12 shows the zonal mean net production of peroxyacyl nitrates in May 2006. While the maximum appears at midlatitudes near the surface, the production remains slightly positive in the Arctic mid-troposphere. PAN can be co-transported with other species during winter and spring [*Beine and Krojnes*, 2000], or it can be produced in the local Arctic environment from PAN precursors transported from elsewhere. The remote middle troposphere still contains ample precursors to the formation of peroxyacyl radicals, such as acetone [*Brühl et al.*, 2000; *Staudt et al.*, 2003]. An adjoint sensitivity analysis of the PAN chemistry revealed that among peroxyacyl radical precursors, the modelled PAN in the Arctic was most sensitive to acetone abun-

dances. In the model, acetaldehyde levels also persist in the Arctic middle troposphere until April, but are rapidly depleted to mean concentrations of 20 pptv by June, whereas acetone concentrations remain at a background level of about 1 ppbv throughout the summer. The simulation of acetone in this version of GEOS-Chem is known to be biased high; however, the impact of this bias on the PAN concentrations in the Arctic lower troposphere is small and a full discussion of the model acetone budget is beyond the scope of this work, but was addressed by *Fischer et al.* [2012].

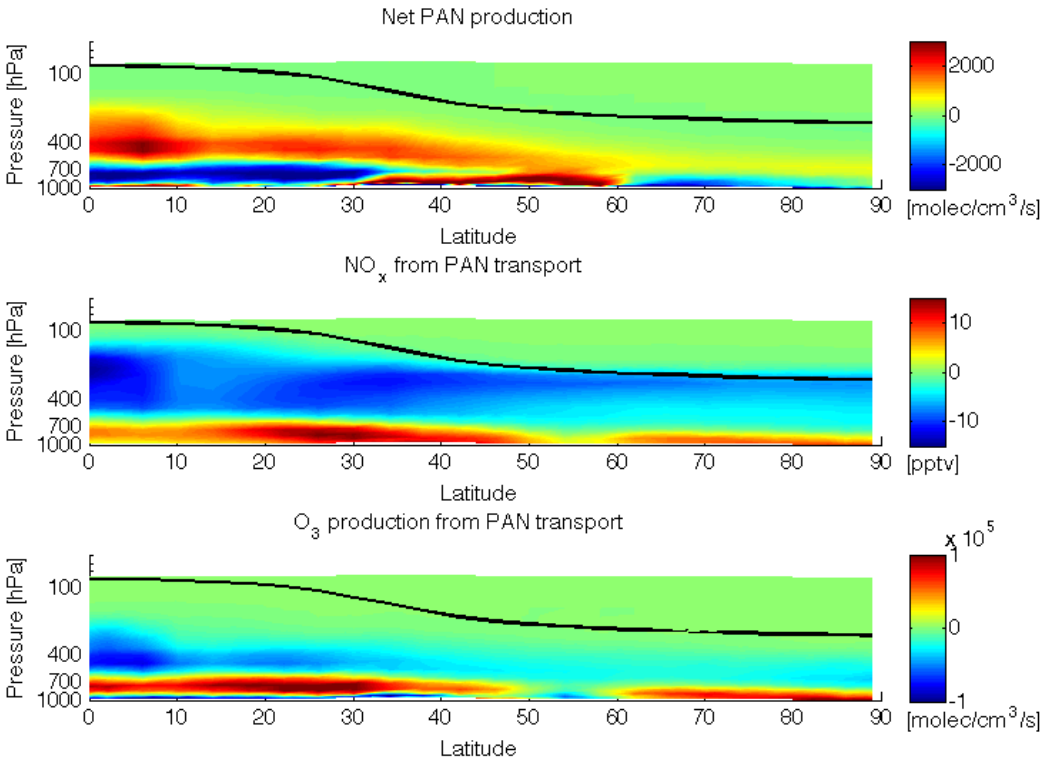

Figure 3.12: Zonal mean plots during May 2006 of net production of peroxyacyl nitrates (top), the concentration of NO_x due to transport by peroxyacyl nitrates (middle), and ozone production due to transport by peroxyacyl nitrates, deduced from the difference between baseline and "no PAN" simulations (bottom). The colour bar for net PAN production is saturated in the lower midlatitudes.

In the Arctic, the peak in PAN production at around 600 hPa coincides with the peak in organic precursor abundances. Throughout the middle and upper troposphere in the Arctic, PAN production represents a sink for NO_x (middle panel of Figure 3.12). On the other hand, the Arctic lower troposphere in May is a region of net PAN destruction, and therefore a source of NO_x and ozone as shown in the middle and bottom panels of Figure 3.12, respectively.

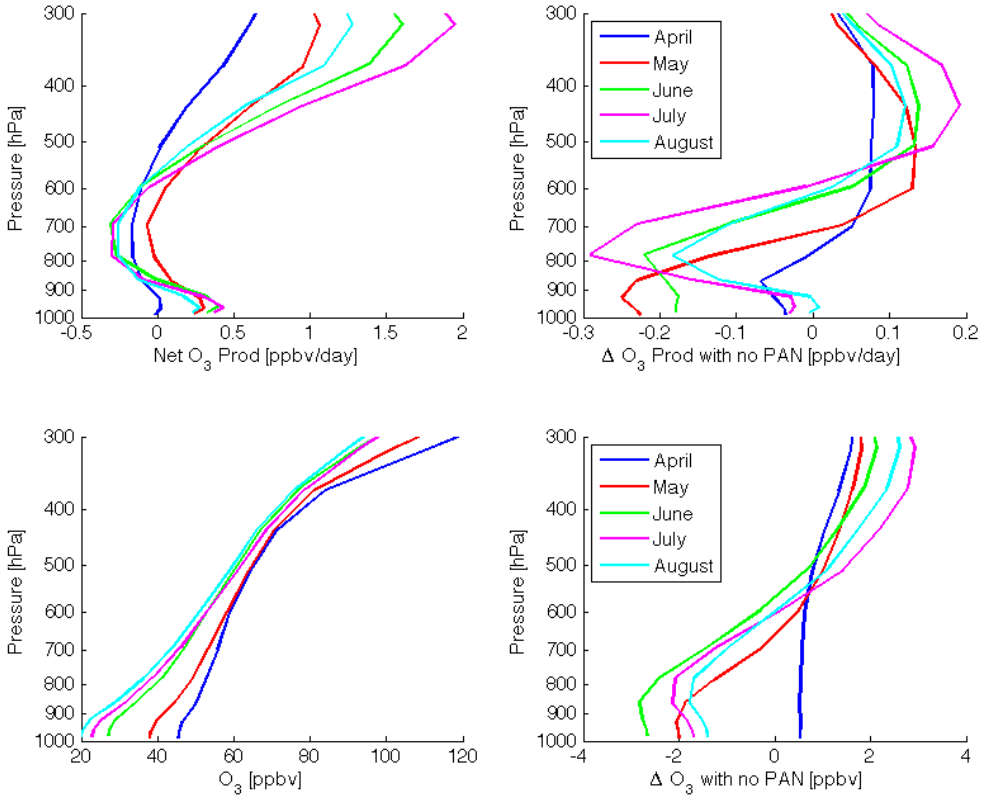

Figure 3.13: Vertical profiles of net ozone production (top two panels) and ozone concentrations (bottom two panels) averaged north of 60°N for months from April to August 2006. The left panels show the net ozone production and ozone concentrations from the baseline run, whereas the right panels show the change in the net ozone production and ozone concentrations as a result of the suppression of the PAN to NO_x interconversion.

Ozone produced by locally-released NO_x evolves through the spring and summer. The upper left panel of Figure 3.13 shows vertical profiles of net ozone production for April through August 2006 in the baseline simulation, averaged across the Arctic. Except in April, the Arctic boundary layer exhibits net production of ozone. As shown in Figure 3.14, this production is driven by surface NO_x concentrations of about 50 pptv in July. There is also net ozone production throughout spring and summer in the upper troposphere, above 500–600 hPa. In contrast, the lower troposphere between about 850–600 hPa, is a net sink for ozone. This picture of Arctic ozone production is consistent with previous studies [*Fan et al.*, 1994; *Cantrell et al.*, 2003; *Liang et al.*, 2009]. *Liang et al.* [2009] suggested that the increase in NO_x concentrations, and thus the ozone production in the upper troposphere, is driven by transport of NO_x from the stratosphere. However, as shown in Figure 3.14, emissions of NO_x from lightning also provide a significant source of upper tropospheric NO_x.

The upper right panel of Figure 3.13 shows the change in the net ozone production when the reaction that inter-converts NO_x and PAN is removed from the chemical mechanism in the model. The changes were obtained by taking the difference of the "no PAN" and baseline simulations. The figure shows that NO_x supplied through PAN was providing up to 0.25 ppbv/day of ozone near the surface in May, when this effect has the greatest impact at the surface. This accounted for 93% of the total ozone production at the surface in May. In June, NO_x from PAN accounted for 55% of the total production at the surface, whereas by August the impact was negligible. In all months in the middle and upper troposphere, above about 600 hPa, suppressing the conversion of NO_x to PAN resulted in a slight increase in net ozone production of about 12%, since PAN formation acts as a NO_x sink at these altitudes. The bottom panels of Figure 3.13 show the effect of this chemical pathway on the mean Arctic ozone concentrations. From May to August, NO_x supplied through PAN provides an additional 2 ppbv of ozone to the Arctic boundary layer, which accounts for up to 10% of the total ozone abundance.

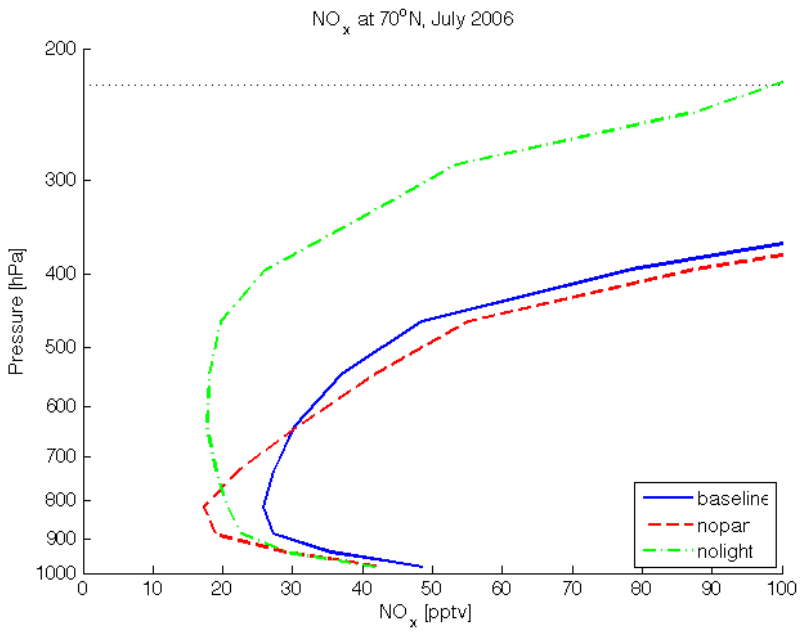

Figure 3.14: Vertical zonal mean profile of NO_x at 70°N in July 2006. The solid blue line shows the baseline simulation, the dashed red line shows the "no PAN" simulation, and the green dash-dotted line shows the baseline simulation with the lightning NO_x source turned off. The dotted line shows the mean tropopause height at 70°N in July 2006.

3.4 Conclusions

An analysis of the budget of ozone in the Arctic troposphere in summer 2006 has been constructed using the GEOS-Chem model. A particular focus has been on quantifying the ozone budget at Eureka, Ny-Ålesund, and Alert, where good observational records exist. When TES ozone data was assimilated to constrain the modelled ozone distribution south of 60°N, the model reproduced well the ozonesonde observations in the Arctic, indicating that the poleward transport of midlatitude ozone in the model is reliable. Although the impact of midlatitude emissions on ozone abundances in the Arctic is at a maximum in fall and winter, in July transport from North America, Asia, and Europe together contributed about 25% of surface ozone abundances in the Arctic. As expected, surface

ozone abundances at Eureka were influenced more by transport from North America than from Europe, which accounted for 11% and 5% of local surface ozone abundances, respectively. In contrast, at Ny-Ålesund transport of ozone from North America and Europe contributed about 10–15% each to local ozone abundances. Transport of ozone from Asia had the least impact on the Arctic troposphere. Throughout the summer, the dominant source of ozone in the Arctic troposphere was photochemical production within the Arctic, which accounted for more than 50% of the ozone in the Arctic boundary layer and as much as 30–40% of the ozone in the middle troposphere. This, combined with the strong adjoint sensitivity to high latitude surface emissions, suggests that increases in Arctic shipping in a more ice-free Arctic Ocean would impact summertime ozone abundances in the Arctic lower troposphere.

To better under the processes contributing to summertime ozone abundances in the Arctic, the adjoint of GEOS-Chem was used to perform a sensitivity analysis of the impact of NO_x emissions on ozone at Alert. NO_x is a key ozone precursor and in both the boundary layer and middle troposphere, ozone abundances at Alert were most sensitive to NO_x emissions between 50°–70°N. Throughout the summer there was strong sensitivity to anthropogenic emissions at these latitudes, although soil emissions of NO_x in the Arctic, near 70°N, also had a strong influence on surface ozone abundances at Alert. As expected, the influence of biomass burning and lighting was more variable. The sensitivity of middle tropospheric ozone above Alert to lightning emissions at times exceeded that to anthropogenic emissions. In the boundary layer and in the middle troposphere, the sensitivity to biomass burning peaked in July, when it was comparable to the sensitivity to anthropogenic emissions. In June ozone abundances in the middle troposphere over Alert were most sensitive to anthropogenic and biomass burning emissions from northern Alberta, Canada, whereas in July the greatest sensitivity was to biomass burning and lightning NO_x emissions from Central Russia. The sensitivity analysis is specific to the year for which the ozone simulation was well-characterized (2006). Sensitivity to partic-

ular sources, especially sources that vary strongly in location such as biomass burning, depends on the synoptic conditions. In a warmer climate, emissions from lightning [*Price and Rind*, 1994] and biomass burning [*Stocks et al.*, 1998] are both expected to increase, impacting the composition of the Arctic troposphere.

Although local surface emissions of NO_x contributed significantly to ozone production within the Arctic boundary layer, transport of NO_x in the form of PAN from outside the Arctic and from the upper troposphere also contributed to ozone production in the lower troposphere. In late May and June, the release of NO_x from PAN decomposition accounted for 93% and 55%, respectively, of the ozone production at the Arctic surface. By July, the fraction of ozone production at the surface associated with PAN decomposition had decreased to 8%. In the upper troposphere, the production of PAN, which acts as a sink for NO_x, resulted in about a 12% decrease in ozone production, averaged from June through August.

The results presented here suggest that although the Arctic lower troposphere is more isolated in summer than at other times during the year, transport of ozone from midlatitude source regions does impact surface ozone abundances in the Arctic. An important question that needs to be examined is how climate-related changes in atmospheric transport pathways will influence summertime ozone abundances in the Arctic. There are also climate-related implications for the strong sensitivity in ozone with respect to high latitude emissions of NO_x from soils and lightning. Although these are natural sources of NO_x, it is important in both an air quality and climate context to understand how changes in climate will influence the contribution of these sources to background ozone levels throughout the Arctic.

Chapter 4

Adjoint Sensitivity Analysis of North American Surface Ozone Concentrations: Implications for Dry Deposition

4.1 Introduction

The composition of the lowermost atmosphere is crucial for air quality; this is where health effects of air pollution are manifested, and where concentrations are monitored for policy requirements. The deposition of harmful oxidants to plant tissues can have further economic impacts on forests or crops [*Driscoll et al.*, 2001]. It is therefore important that models capture the behaviour of the lowermost atmosphere to enable accurate air quality forecasts and proper attribution of pollution sources.

As with elsewhere in the troposphere, ozone concentrations in the planetary boundary layer (PBL) result from the balance of chemical production and loss, modulated by transport (see Figure 4.1). The PBL itself is a complex dynamic environment with air

entrained from above, turbulent mixing, and deposition processes at the surface. The vertical extent of the PBL varies with season, time of day, and synoptic meteorological conditions. Peak pollutant concentrations are strongly related to the extent of the boundary layer, with larger mixing depths allowing more dilution [*Lin et al.*, 2008]. Poor estimates of boundary layer height affect model performance with respect to surface observations [*Mao et al.*, 2010].

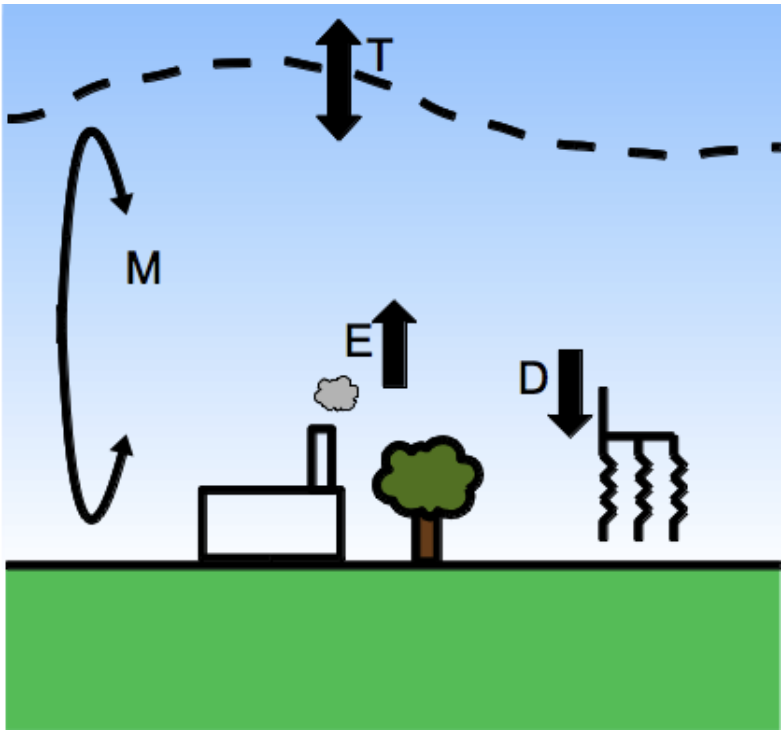

Figure 4.1: Processes affecting ozone concentrations in the planetary boundary layer. A balance between chemical production from emissions (E) and destruction through surface deposition (D) is modulated by transport processes such as mixing (M) in the variable depth PBL and transport (T) of free tropospheric air from above.

Ozone in the PBL comes from both precursor emissions, which drive in situ production, and from downward transport of free tropospheric ozone. Estimates of both anthropogenic and natural surface NO_x emissions have been obtained from remote sensing observations [*Martin et al.*, 2003a; *Jaeglé et al.*, 2005; *Sauvage et al.*, 2007; *Lin*, 2012].

Satellite-observed formaldehyde columns have been used as a constraint on biogenic isoprene emissions [*Palmer et al.*, 2003; *Millet et al.*, 2008]. The free tropospheric ozone distribution has also been constrained from satellite observations [*Lamarque et al.*, 2002; *Parrington et al.*, 2008].

A multi-model study showed large positive biases (maximum daily 8-h averages biased from 10 to 20 ppbv in the multi-model mean) relative to surface ozone over the eastern U.S. in summertime [*Reidmiller et al.*, 2009]. Large mean summertime biases can be seen in Figure 4.2 for the northeastern and southeastern U.S. The large spread among models can likely be attributed to differences in deposition, humidity, and isoprene chemistry. Using the MOZART CTM, *Lin et al.* [2008] also found a positive bias relative to surface measurements, and that while increasing the horizontal resolution from $\sim 1.9°$ to $\sim 1.1°$ in the model impacted individual sites, the effects were cancelled in regional averages. *Parrington et al.* [2013] showed that using TES ozone profiles to constrain the free tropospheric background ozone together with additional satellite constraints on emissions of NO_x [*Martin et al.*, 2003a] and isoprene [*Millet et al.*, 2008] was insufficient to correct the bias between simulated ozone in GEOS-Chem and ozone observations from surface measurement networks in eastern North America. We scrutinize possible reasons for the remaining bias, including the effects of model resolution, boundary layer mixing scheme, and sensitivity to dry deposition rates. A particular focus of this chapter is on quantifying the dry deposition of ozone, which is highly uncertain, as shown in Table 1.1.

This chapter examines possible explanations for the model bias in surface ozone that are not related to precursor emissions estimates or the distribution of ozone in the free troposphere. Ozone observations from surface measurement networks are used together with a regional CTM and its adjoint. The data and models are described in Section 4.2. The adjoint sensitivities of surface ozone are examined in Section 4.3 to determine which parameters may be responsible for the remaining bias. In Section 4.4, the observation

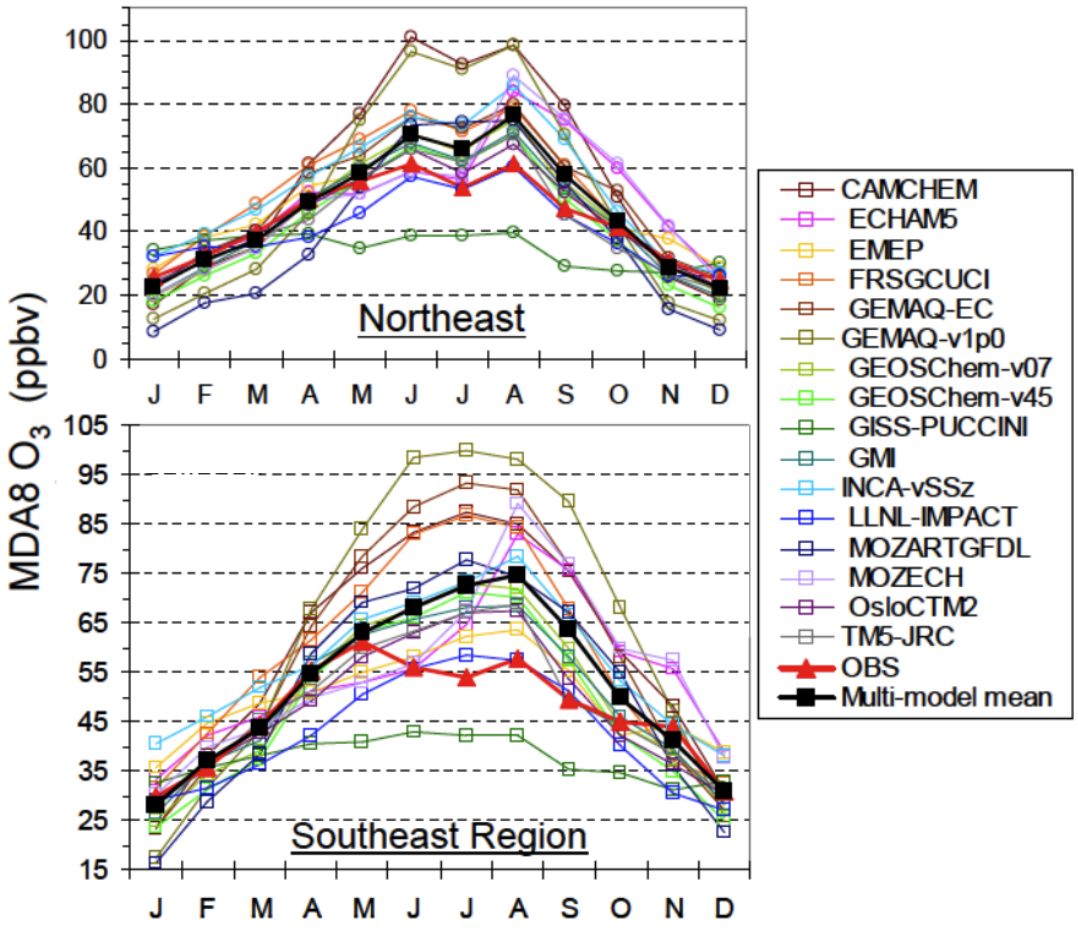

Figure 4.2: Observed (red triangles) and simulated monthly mean maximum daily 8-hour (MDA8) surface ozone for the northeastern (top) and southeastern (bottom) U.S. The multi-model mean is shown in black squares. Figure adapted from *Reidmiller et al.* [2009].

network data is assimilated using the adjoint model to constrain these parameters. Conclusions are presented in Section 4.5.

4.2 Observations and Model Configuration

4.2.1 Surface Observation Networks

Surface ozone concentrations are monitored by regional networks for air quality reporting and forecasts, as described briefly in Section 2.3.1. Data from three North American networks are used in this study: CASTNET [*Sickles and Shadwick*, 2002], AQS [*Chameides et al.*, 1997]), and NAPS [*Curren and Dann*, 2004]. All three networks provide measurements of ozone concentrations, which have been averaged hourly. The focus here is on afternoon observations between 1200-1800h local time, which is a time of peak surface ozone concentrations in the summer [*Bloomer et al.*, 2010] and has been used as a metric of model performance in previous studies [*Parrington et al.*, 2009]. The distribution of the hourly surface ozone measurements is displayed in Figure 4.3, comprising over 260,000 hourly observations between August 1–10, 2006. Network coverage is most comprehensive in the eastern U.S. and southern Canada, with sparser spacing over the western part of the continent. Figure 4.4 shows the mean surface ozone concentrations at all the surface sites. The overall mean of the observations is 33.0 ppbv.

4.2.2 Chemical Transport Model Configuration

This study employs version v9-01-02 of GEOS-Chem forward model, which is a more recent version than that used in Chapter 3, and is similar to that employed by *Zhang et al.* [2011]. Recent improvements in model resolution have enabled studies at the native GEOS-5 horizontal resolution of $0.5^\circ \times 0.666^\circ$ over regional domains [*Wang et al.*, 2004; *Chen et al.*, 2009]. Figure 4.5 compares the model bias in surface ozone relative to the network observations during the study period at coarse and fine resolutions. The peak

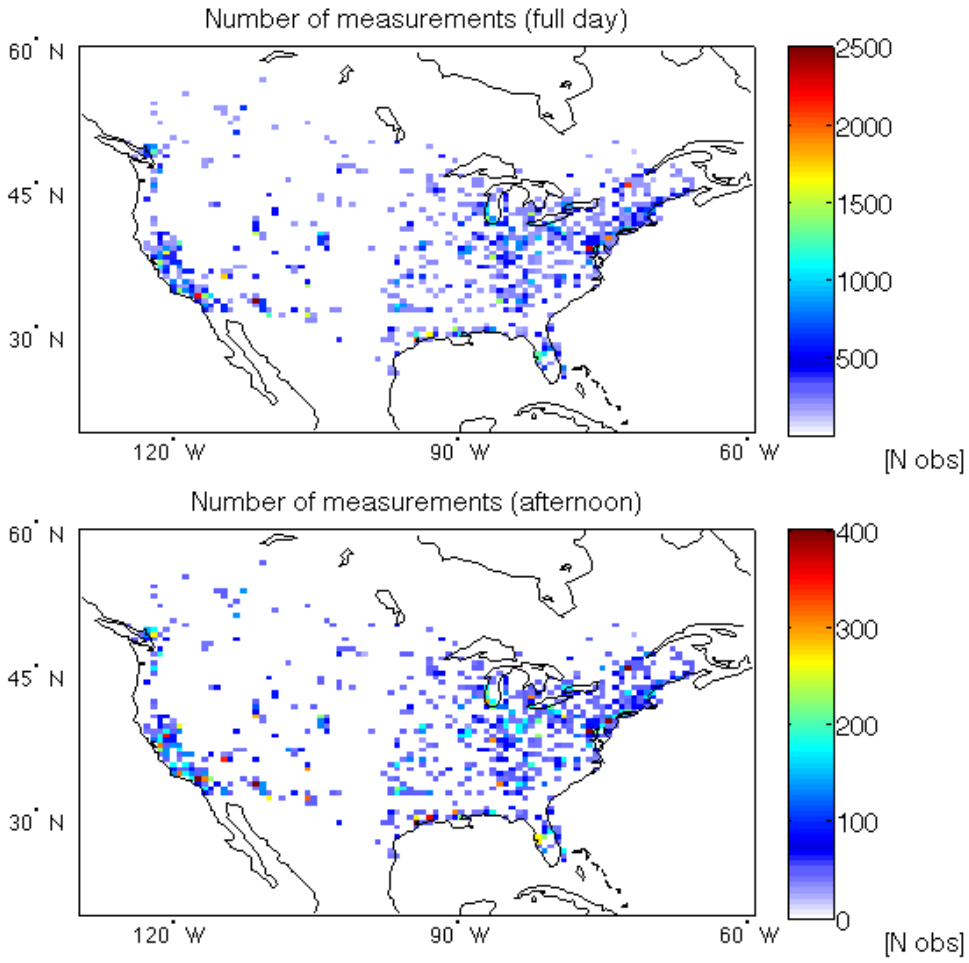

Figure 4.3: Number of hourly ozone measurements at CASTNET, AQS, and NAPS network sites from August 1-10, 2006, averaged onto the GEOS $0.5° \times 0.666°$ grid. The number of observations is shown for the full day (top) and for the afternoon only (1200-1800h, bottom).

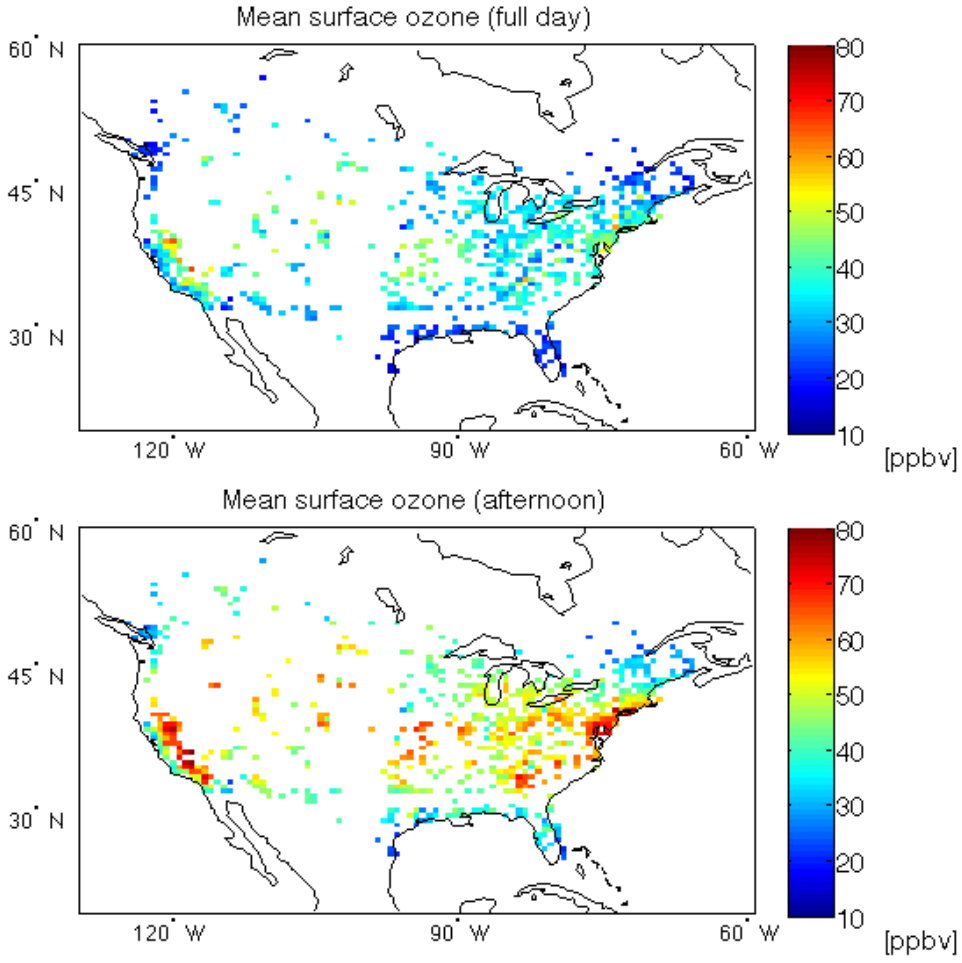

Figure 4.4: Mean of hourly ozone measurements at CASTNET, AQS, and NAPS network sites from August 1-10, 2006, averaged onto the GEOS $0.5° \times 0.666°$ grid. Means are shown for the full day (top) and for the afternoon only (1200-1800h, bottom).

negative biases on the West Coast become diluted in the coarse model, and some of the East Coast sites that are well-represented at the fine resolution are averaged with nearby positively biased stations in the coarse grid. Table 4.1 shows the change in mean bias for various subregions of the domain, sampled at the network locations. *Fiore et al.* [2003] found a similar increase in ozone bias at higher model resolution as the small-scale features in the ozone distribution are more difficult for the model to capture correctly.

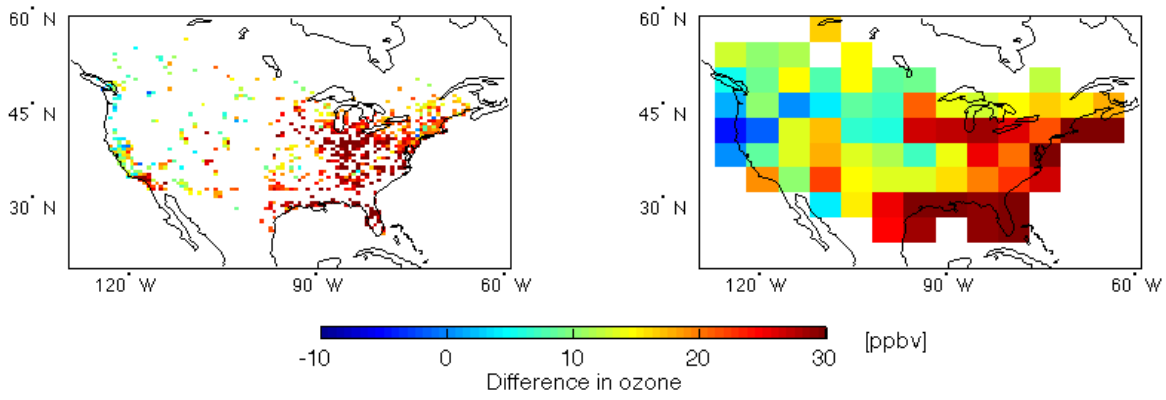

Figure 4.5: Difference in surface ozone at surface network sites in August 2006 between the surface ozone network observations and GEOS-Chem simulations at $0.5° \times 0.666°$ (left) and at $4° \times 5°$ (right).

Planetary Boundary Layer Mixing

Mixing of a tracer within the PBL affects its concentration at the surface. The turbulent flux of a chemical tracer is often taken as proportional to the local concentration gradient. This parameterization works reasonably well when the length scale of the smallest turbulent eddies is smaller than the domain. However, an additional term is needed to represent unstable, convective motions ("large eddy motion"). This so-called non-

Table 4.1: Mean GEOS-Chem model ozone bias relative to surface observing networks at all available latitudes for various simulations. FMBL and NLBL refer to the fully-mixed and non-local boundary layer mixing schemes, respectively. All values are given in ppbv.

Region	$4° \times 5°$ FMBL	$0.5° \times 0.666°$ FMBL	$0.5° \times 0.666°$ NLBL
North America	16.4	21.3	17.4
West of 100°W	9.9	13.4	10.7
East of 100°W	21.0	24.2	19.8

local term is the part of the diffusion that does not depend on the local concentration gradient [*Holtslag and Boville*, 1993], and depends on the bulk properties of the PBL.

The implementation of a non-local boundary layer (NLBL) mixing scheme was studied in the MOZART CTM [*Lin et al.*, 2008], and a similar scheme has been introduced in GEOS-Chem [*Lin and McElroy*, 2010]. The PBL in previous versions of GEOS-Chem was assumed to be fully mixed (FMBL). The non-local scheme has previously been shown to reduce the bias in GEOS-Chem at $2° \times 2.5°$ resolution relative to surface ozone observations by 2–5 ppbv, with the largest differences occurring at night [*Lin and McElroy*, 2010]. High resolution simulations using both schemes were performed, and the difference in hourly surface ozone at the network locations is shown in Figure 4.6. The fully-mixed PBL produces higher surface ozone concentrations at most sites, with a mean increase of 3.9 ppbv over the more accurate non-local mixing scheme.

Dry Deposition

Dry deposition in GEOS-Chem is modelled using a "big-leaf" model, where the flux to the surface is proportional to the concentration near the surface. The constant of proportionality is called the dry deposition velocity (V_d), and is usually modelled as a set

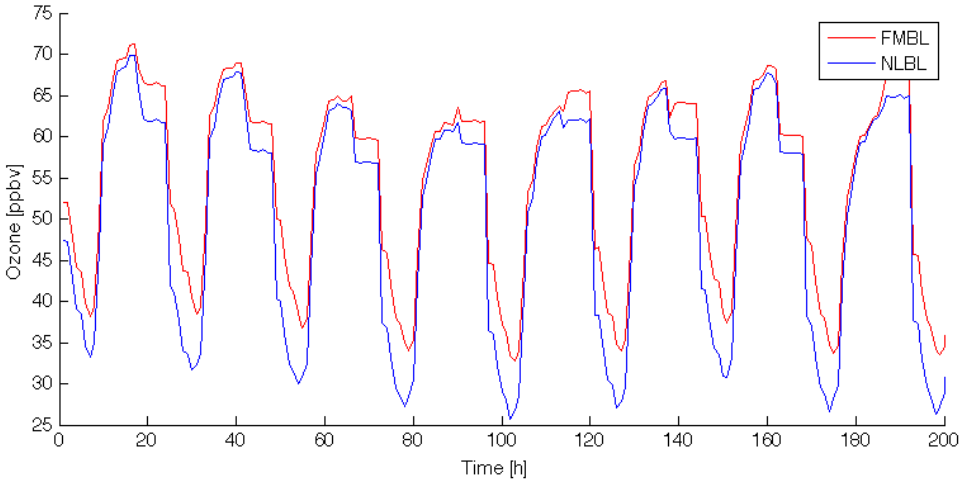

Figure 4.6: Timeseries of GEOS-Chem surface ozone at network sites starting at midnight UTC, August 1, 2006, for a simulation using a FMBL and one using a NLBL for the planetary boundary layer.

of resistances [*Wesely and Hicks*, 2000]. For a chemical species i, the flux to the surface F^i is given by

$$F^i = V_d^i C^i, \tag{4.1}$$

where C^i is the concentration near the surface, and the deposition velocity may be expressed

$$V_d^i = \frac{1}{R_a + R_b^i + R_c^i}, \tag{4.2}$$

where R_a represents aerodynamic resistance above the surface, R_b^i the resistance in a quasi-laminar layer of air adjacent to the surface, and R_c^i is the total surface resistance. R_a and R_b^i are calculated using standard methods. The aerodynamic resistance, which is independent of the gaseous species, depends on the stability near the surface. The formulation for stable, neutral, and unstable conditions are as follows [*Wu et al.*, 2011]:

$$R_a = 0.74(\kappa u*)^{-1}[\ln(z/z_0) + 4.7(z - z_0)/L] \quad (4.3)$$

$$R_a = 0.74(\kappa u*)^{-1}\ln(z/z_0) \quad (4.4)$$

$$R_a = 0.74(\kappa u*)^{-1}\left(\ln\left[\frac{(1-9z/L)^{0.5}-1}{(1-9z/L)^{0.5}+1}\right] - \ln\left[\frac{(1-9z_0/L)^{0.5}-1}{(1-9z_0/L)^{0.5}+1}\right]\right), \quad (4.5)$$

where z_0 is a roughness length for momentum, κ is von Karman's constant, $u*$ is the friction velocity, and L is the Obukhov length. The sublayer resistance R_b represents mass transfer across a thin layer of air in contact with the surface, and depends on the species diffusivity, as follows:

$$R_b = 2(\kappa u*)^{-1}(S_c/P_r)^{2/3}, \quad (4.6)$$

where S_c is the Schmidt number, and P_r is the Prandtl number for air [*Wesely and Hicks*, 1977].

The main uncertainty arises in the calculation of R_c^i, called the total surface resistance. The latter term includes resistances to deposition to the soil, water, or other surface, to the vegetative canopy, as well as resistances to uptake by plants through the stomata or on the cuticle. In GEOS-Chem, the deposition velocities are used to calculate the deposition rates at each vertical level within the PBL, which are used in the chemistry solver at the chemistry timestep. The deposition rates are calculated throughout the PBL because during each discrete timestep, the model mixing brings the air in the PBL in contact with the surface.

A variety of models exist for calculating the total surface resistance. The formulation used in GEOS-Chem is based on *Wesely* [1989]. The dominant error in calculating dry deposition velocity for ozone using this scheme is the minimum stomatal resistance [*Schwede et al.*, 2011; *Wu et al.*, 2011]. The non-stomatal pathway can also cause increases in uptake rates of up to a factor of three under wetter conditions [*Zhang et al.*, 2002], an effect that is difficult to model owing to the diversity of situations involving wet vegetation

surfaces (e.g., dew, rain, high humidity) [*Wesely and Hicks*, 2000]. The mean dry deposition velocity calculated by GEOS-Chem across the North American domain for August 2006 is about 0.3 cm/s with peak values of up to 0.8 cm/s.

CASTNET also provides hourly output of quantities related to dry deposition. The CASTNET stations measure meteorological variables that are used as input to a multilayer model that calculates deposition velocities [*Meyers et al.*, 1998]. *Finkelstein et al.* [2000] showed good agreement of the inferred fluxes from this model with measured fluxes at coniferous and deciduous forest sites, while *Meyers et al.* [1998] showed agreement with measurements over croplands. However, a comparison between the multilayer and big-leaf models of deposition revealed differences in the calculated flux on the order of a factor of 2–3, which was attributed to the specification of surface resistances [*Schwede et al.*, 2011]. This highlights the uncertainty in the calculation of deposition rates introduced in Table 1.1.

Isoprene Oxidation Chemistry

In the VOC oxidation chemistry described in Chapter 1, the hydroxyl radical (OH) is regenerated through reactions with NO_x. However, recent observations of OH regeneration in a low-NO_x environment over tropical forests have stimulated research into additional chemical mechanisms [*Lelieveld et al.*, 2008; *Paulot et al.*, 2009; *Peeters et al.*, 2009; *Taraborrelli et al.*, 2009]. Adding an OH yield to the reactions between peroxy radicals (which are products of isoprene oxidation) improves agreement between modelled and observed OH in the tropics [*Lelieveld et al.*, 2008], and while the effect of this reaction on OH concentrations is smaller at midlatitudes, changing the abundance of HO_x has strong implications for the ozone production regime.

Recent work implementing a new isoprene oxidation mechanism that includes regeneration of OH radicals in GEOS-Chem [*Mao et al.*, 2013] demonstrates this change in ozone production regime in the eastern U.S. Because OH is no longer titrated by isoprene,

ozone loss by direct reaction with isoprene is lessened. This is aided in the simulation by also including recycling of NO_x from isoprene nitrates [*Paulot et al.*, 2012; *Mao et al.*, 2013], further distancing the simulated conditions from those conducive to ozone loss by reaction with isoprene [*Fiore et al.*, 2005]. The updated chemical mechanism presented in *Mao et al.* [2013] is not included in the version of GEOS-Chem used in this thesis; however, implications of the new chemistry are discussed below.

4.2.3 Adjoint Model Configuration

We use v32 of the GEOS-Chem adjoint model. The adjoint model was initially described by *Henze et al.* [2007] with updates and recent applications presented by *Kopacz et al.* [2010]; *Jiang et al.* [2011]; *Singh et al.* [2011]. Emissions for the adjoint model simulations in this study are chosen to match those described in *Parrington et al.* [2008] and the forward GEOS-Chem simulations described above. As described previously, the adjoint model efficiently calculates the gradients around the simulated state of model output (e.g., a metric of tracer concentrations) with respect to model inputs simultaneously, at the resolution of the model. These gradients are interpreted here as the sensitivity of the tracer concentrations to either spatially-resolved emissions, to initial tracer concentrations, or to reaction rates.

Adjoint models have been used to study ozone pollution episodes in Paris [*Schmidt and Martin*, 2003], and the sensitivity of tracer concentrations to reaction rates [*Menut et al.*, 2000; *Paulot et al.*, 2012]. Other data assimilation methods such as the ensemble Kalman filter have proven effective in improving ozone air quality forecasts by optimizing both emissions and initial concentrations of ozone [*Tang et al.*, 2011].

Motivated by the results of *Parrington et al.* [2013], the adjoint model of GEOS-Chem was used to calculate the sensitivity of the mean surface ozone concentration over eastern North America to the initial tracer concentrations in a simulation running during August 2006. The sensitivity of the mean surface concentrations of both ozone and NO_x

in the same spatial domain to model emissions of NO_x and isoprene were also calculated. Finally, 4D-Var inversions using the surface ozone network observations were performed to obtain optimized estimates of control parameters such as emissions and reaction rates.

Running the adjoint model at high spatial resolution over the standard nested domain is computationally expensive, so an appropriate subdomain over eastern North America where the model biases are large was used (20–51°N, 64–110°W). The nested model over the full North American domain (10–70°N, 40–140°W) is run using boundary conditions from a low-resolution simulation that has been constrained in the free troposphere using TES ozone and CO profiles as in *Parrington et al.* [2008]. The boundary conditions to the subdomain are archived from the full nested domain simulation. Errors incurred in transport from the edge of the full nested domain to the edge of the subdomain are presumed to be small.

The adjoint of the newly implemented non-local boundary layer mixing scheme is not available in this version of the GEOS-Chem adjoint model. However, as an interim correction, the time-varying, three-hour average bias in surface ozone caused by the difference in boundary layer schemes (shown in Figure 4.6) is removed from the adjoint forcing during the 4D-Var inversions to assess the impact of the bias on the optimized ozone distribution.

4.3 Adjoint Sensitivity Analysis of Surface Ozone

4.3.1 Sensitivity of Surface Concentrations to Emissions

While assimilating ozone profiles from TES into GEOS-Chem produces good agreement with independent observations in the free troposphere [*Parrington et al.*, 2008], it does not result in a similar improvement at the surface [*Parrington et al.*, 2009]. The free tropospheric ozone background corrected by the TES assimilation reduces biases at the surface in western North America, but exacerbates the model's high bias in the east.

The adjoint gradients are used as an indication of sensitivity to explore what model parameters may be influencing the high simulated values in this region.

Figure 4.7 shows the adjoint sensitivities of mean surface ozone concentrations over eastern North America to NO_x and isoprene emissions. In both cases the sensitivities are largest within the eastern North America region where we are calculating the sensitivities, which shows that surface concentrations have relatively smaller sensitivity to changes in emissions upwind in western North America. Surface ozone sensitivities to NO_x emissions are positive with large values occurring around many of the observation sites, which happen to be coincident with emissions sources. The larger positive sensitivities here mean that surface ozone over eastern North America would increase more in response to a unit increase in NO_x emissions at these locations.

The sensitivity of surface ozone to isoprene emissions comprises both positive and negative values, reflecting the different chemical regimes present in the sumer. Two regions of positive sensitivities appear: south of the Great Lakes, and along the Gulf

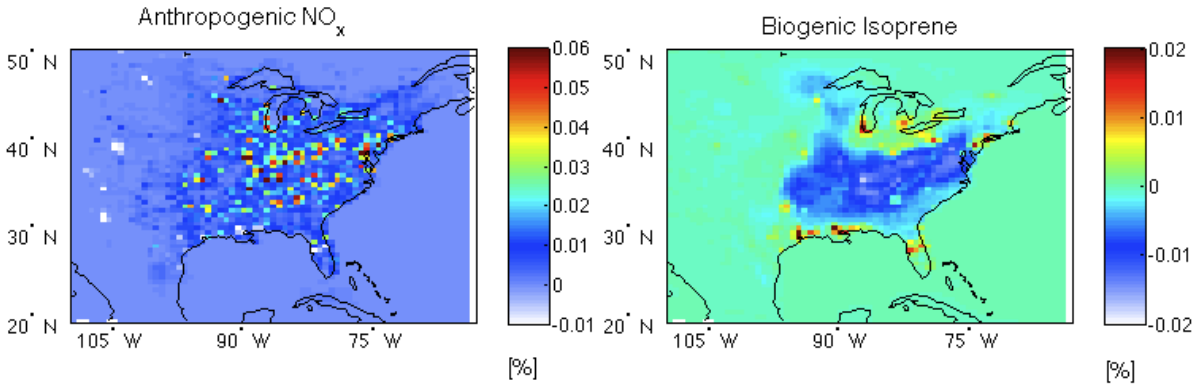

Figure 4.7: Maps of the sensitivity (λ_{ij}) of surface ozone concentrations from the GEOS-Chem adjoint model at network sites to emissions, in percent, for the first ten days of August 2006. The left panel shows the sensitivity with respect to anthropogenic NO_x emissions, and the right panel shows sensitivity with respect to biogenic isoprene emissions.

Coast. Surface ozone in these areas would increase if isoprene emissions were to increase. Contrarily, negative sensitivities of ozone to isoprene emissions occur throughout much of the inland eastern U.S. This region already has high isoprene concentrations, and increasing isoprene emissions further would lead to increased ozone destruction through direct ozonolysis by isoprene [*Fiore et al.*, 2005]. With the recent updates to the isoprene oxidation scheme proposed by *Mao et al.* [2013], ozone loss through reaction with isoprene is mitigated, and the negative values of the sensitivity of surface ozone to isoprene emissions change to positive.

Adjoint sensitivities were also calculated for surface ozone concentrations (5–49°N and 101–61°W) with respect to the initial conditions of all chemical tracers in the model. Figure 4.8 displays the magnitude of the maximum sensitivity with respect to each of these tracers at each vertical level in the model. The strongest sensitivities, in order, are for ozone with respect to O_x, followed by those with respect to PAN, CO, ALD2, and NO_x. Vertical gradients in the maximum sensitivity are more pronounced for the shorter-lived tracers because they will exhibit a greater difference in their impact on surface ozone at different altitudes.

Sensitivity analysis using the adjoint model of GEOS-Chem reveals characteristics about the chemical regime and a detailed representation of how ozone would respond to changes in precursor emissions. It also provides a means to guide future studies into the residual biases in the simulation of surface ozone by succinctly demonstrating the chemical linkages to all of the model tracers and ranking them according to their potential impacts on ozone.

4.3.2 Sensitivity of Surface Concentrations to Reaction Rates

The GEOS-Chem adjoint model was updated to provide sensitivities of a cost function with respect to chemical reaction rates, including dry deposition rates [*Paulot et al.*, 2012]. The sensitivities to reaction rates provide yet another means of probing the importance

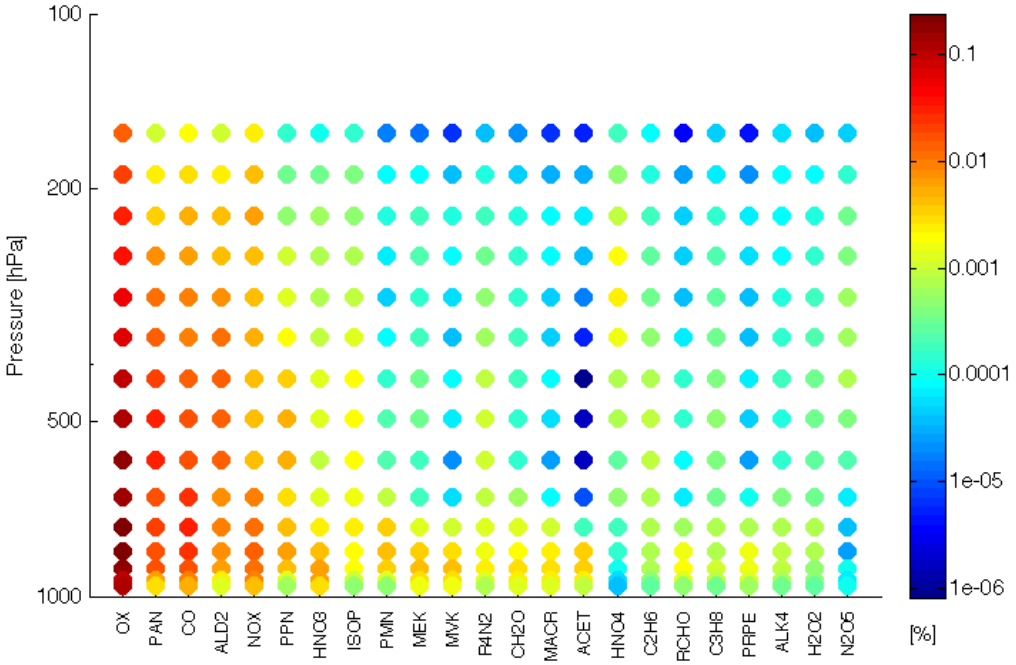

Figure 4.8: Magnitude of the maximum sensitivity (in percent) at each model vertical level of mean surface ozone over eastern North America in August 2006 to initial tracer concentrations. Tracer labels are defined as follows: OX = odd oxygen; PAN = peroxyacetyl nitrate; CO = carbon monoxide; ALD2 = acetaldehyde; NOX = reactive nitrogen oxides; PPN = peroxypropionyl nitrate; HNO3 = nitric acid; ISOP = isoprene; PMN = peroxymethacryloyl nitrate; MEK = methyl ethyl ketone; MVK = methyl vinyl ketone; R4N2 = >C3 alkyl nitrates; CH2O = formaldehyde; MACR = methacroelein; ACET = acetone; HNO4 = pernitric acid; C2H6 ethane; RCHO = >C2 aldehydes; C3H8 = propane; PRPE = propene; ALK4 = >C3 alkanes; H2O2 = hydrogen peroxide; N2O5 = dinitrogen pentoxide.

of chemical processes affecting surface ozone and guiding studies towards reactions with the greatest potential impacts.

Figure 4.9 shows the summed magnitude of fully normalized adjoint gradients, as calculated by Equation (2.24), of ozone within the surface layer with respect to various reaction rates. Of the reactions examined here, surface ozone was most sensitive to ozone reacting with NO. The next most significant reaction was the ozone dry deposition rate. If the former rate were increased, less NO would be available to participate in the catalytic ozone production cycle. Other NO_x sinks were similarly significant in this ranking, including NO_2 dry deposition, and production of nitric acid (NO_2+OH) and isoprene nitrates (RIO_2+NO). Further efforts in this study are directed towards the ozone dry deposition rate, which is both significant in its impact on ozone concentrations and contains appreciable uncertainty in its parameterization. The uncertainties on these reaction rates are discussed in greater detail in Section 4.4.2.

4.4 4D-VAR Inversion Results

4.4.1 Constraining Precursor Emissions

As demonstrated by Figure 4.5, surface ozone simulated in GEOS-Chem is biased relative to the observing networks over eastern North America. *Parrington et al.* [2013] attempted to correct this bias by combining observations of TES ozone, SCIAMACHY NO_2, and OMI formaldehyde in GEOS-Chem to constrain the free tropospheric ozone distribution, surface NO_x emissions, and biogenic isoprene emissions, respectively. Despite these refined estimates of precursor emissions and of ozone transported from above, the simulation remained biased with respect to surface ozone observations, especially in the eastern U.S.

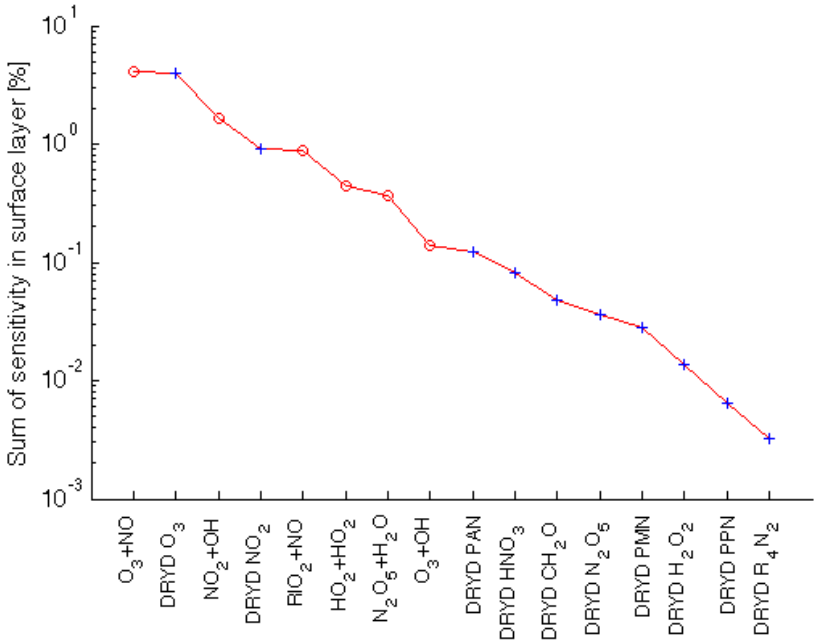

Figure 4.9: Magnitude of the summed normalized adjoint gradients (in percent) in the surface layer with respect to reaction rates. The sum of the gradients is negative, indicating that an increase in each rate would decrease ozone abundances. Gradients are shown for a cost function using the mean O_3 concentration at the surface network sites. Sensitivities to dry deposition rates are shown with blue crosses, and those to chemical reaction rates are shown with red circles.

A 4D-Var inversion was conducted with the high resolution GEOS-Chem adjoint model, using observations from the surface ozone networks, and precursor emissions as control parameters. The cost function for this inversion can be expressed as

$$J = \frac{1}{2}\Big(\sum_{n=0}^{N}(\mathbf{x}-\mathbf{x}^{obs})^T\mathbf{S}_{obs}^{-1}(\mathbf{x}-\mathbf{x}^{obs}) + \gamma(\mathbf{c}-\mathbf{c}_0)^T\mathbf{S}_a^{-1}(\mathbf{c}-\mathbf{c}_0)\Big), \tag{4.7}$$

where $\mathbf{S}_{obs}$ indicates the observation covariance matrix, which is assumed to be diagonal with a 50% error on observations. The sparser observations west of 100°W are not

included in the cost function. Also, the observation error at coastal sites is inflated by a factor of 5 to account for model representativeness at these sites.

The vector of model parameters $\mathbf{c}$ contains scale factors for all latitudes, longitudes, and types of emission in the model domain. At every latitude (i) and longitude (j), the emissions are modified by a scale factor $\mathbf{c}^n$ that begins with an a priori value of $\mathbf{c}_0^n$ in the first iteration, and is updated during the inversion to modify emissions from their initial values (E_0) as follows:

$$E^n = \mathbf{c}^n E_0^n. \tag{4.8}$$

The superscript n indicates the various types of emissions included in the control vector (e.g., anthropogenic NO_x, biogenic isoprene, biomass burning CO, etc...). The matrix $\mathbf{S}_a$ is the covariance matrix for the a priori guesses for the scale factors, which is again assumed to be diagonal. A 100% error is assumed for the a priori emissions.

Figure 4.10 shows that the reduction in NO_x emissions across the eastern United States needed to match the observed surface ozone distribution is severe. The inversion attempts to drastically reduce NO_x emissions over most of the eastern U.S. The scale factors shown for anthropogenic NO_x reduce the continental total emissions from 0.43 Tg N/month to 0.25 Tg N/month. This reduction is unrealistic compared to constraints from the International Consortium for Atmospheric Research on Transport and Transformation (ICARTT) measurement campaign on the bottom-up inventories for the same study period [*Hudman et al.*, 2007], which produce an estimate of 0.62 Tg N over 45 days (0.40 Tg N/month). Further, satellite-derived estimates of anthropogenic NO_x [*Martin et al.*, 2003a] find an increase from their a priori estimate from 7.0 Tg N/yr (0.58 Tg N/month on average) to 7.7 Tg N/yr (0.63 Tg N/month). Comparing the NO_2 columns resulting from the inversion to those retrieved from the OMI satellite instrument highlights regions of unreasonably low NO_2 across the midwest and central eastern states.

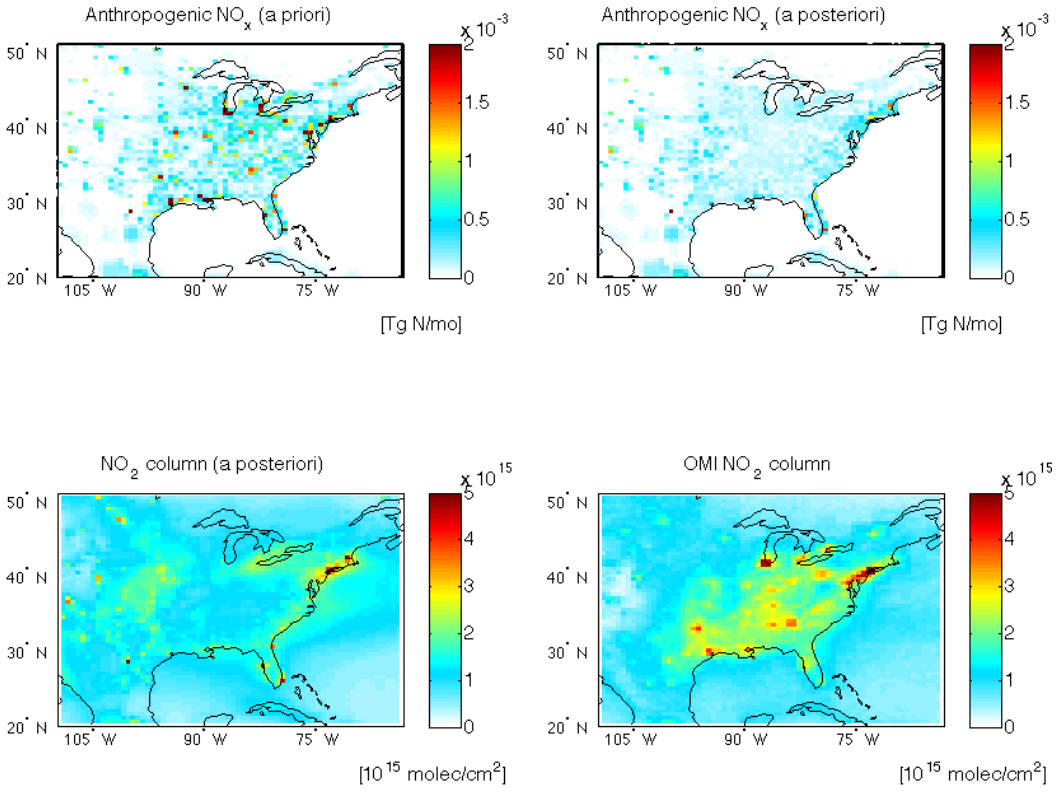

Figure 4.10: Scaling of anthropogenic NO_x emissions resulting from an adjoint inversion using surface ozone observations. The a priori emissions distributions (top left) are scaled in the inversion to produce the a posteriori distribution (top right). The resulting NO_2 columns (bottom left) are then compared to those obtained from the OMI satellite (bottom right).

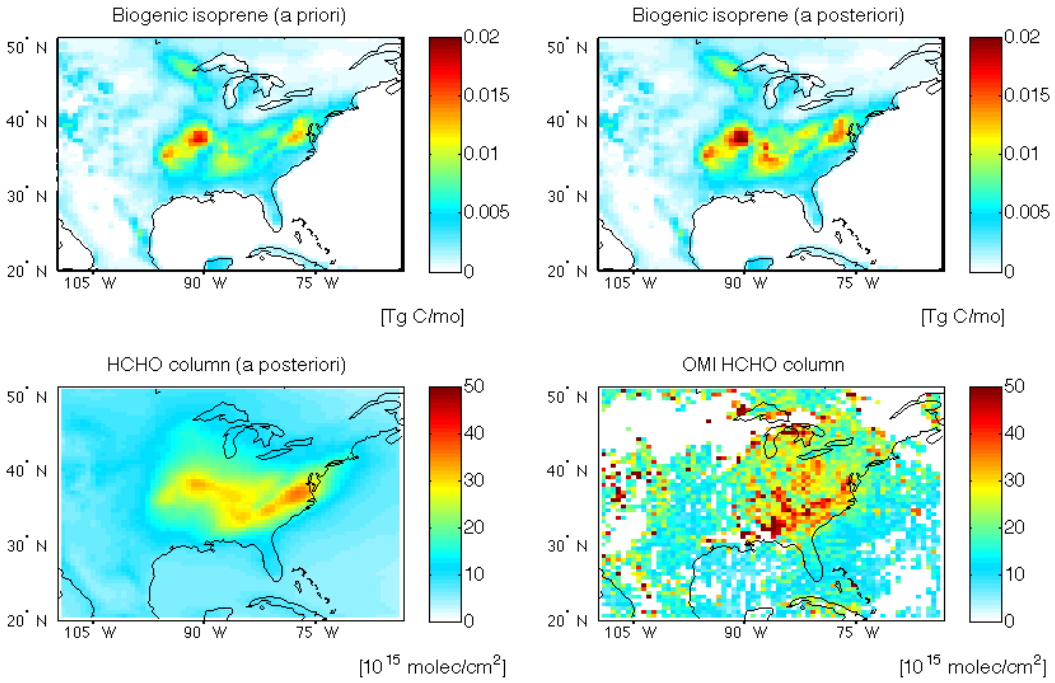

Figure 4.11: Scaling of biogenic isoprene emissions resulting from an adjoint inversion using surface ozone observations. The a priori emissions distributions (top left) are scaled in the inversion to produce the a posteriori distribution (top right). The resulting CH_2O columns (bottom left) are then compared to those obtained from the OMI satellite (bottom right).

The a posteriori emissions for isoprene in this inversion are shown in Figure 4.11. The inferred emissions in this case also appear unrealistic, with the largest increases concentrated in the inland southeastern U.S. The continental total emissions rise from 7.0 Tg C/month to 7.7 Tg C/month. A satellite-based estimate of continental isoprene emissions, based on formaldehyde (an oxidation product of isoprene) observations, reduced the initial guess of 6.9 Tg C/month to 3.7 Tg C/month [*Millet et al.*, 2008]. The Model of Emissions of Gases and Aerosols from Nature (MEGAN) [*Guenther et al.*, 2006] produces an estimate of 4.1 Tg C/month for biogenic isoprene emissions during the same period. Comparing the CH_2O columns resulting from the inversion to those derived

from OMI observations shows evidence of the unrealistic spread in the spatial extent of maximum isoprene emissions to the west of 90°W. However, if the sensitivity of ozone to isoprene emissions is positive as suggested by [*Mao et al.*, 2013], isoprene emissions in the southeastern U.S. would be scaled in the opposite direction. This change would exacerbate the difference relative to the OMI formaldehyde columns, but also lower the continental total, in the direction of estimates from MEGAN or [*Millet et al.*, 2008]. A proper inversion reconciling these impacts is left for future study. With the chemistry included in this model version, modifying only surface emissions requires unrealistic changes in order to match the surface network ozone observations.

4.4.2 Constraining Surface Sinks

The GEOS-Chem adjoint model was further extended to include reaction rate coefficients as possible parameters in a 4D-VAR inversion. Here the GEOS-Chem adjoint model is used for the first time to constrain reaction rate coefficients. Hourly mean observations from surface network sites were incorporated with an observation error of 50%. The majority of this error assignment is due to the model's difficulty in representing a point measurement at the surface. A priori values of the ozone dry deposition rate calculated by the GEOS-Chem model are assumed to have 100% error. Both the observation covariance matrix and the background covariance matrix are assumed to be diagonal. The cost function for this inversion may be expressed in the same form as Equation (4.7). However, the scale factors $\mathbf{c}$ in the second term now also extend in the vertical dimension, and instead of modifying emissions, now modify the dry deposition rate of ozone or other chemical reaction rates.

A set of four inversion experiments was carried out, as is summarized in Table 4.2. The same restrictions on observations are used in all inversions here as were used in the inversions to constrain emissions in the previous section. In addition to a baseline inversion, the "PBL corrected" simulation is used to assess the impact of correcting for

the known bias due to the PBL mixing. This was done by subtracting the difference in surface ozone between simulations using a fully-mixed boundary layer and the non-local mixing scheme. This corrected state is used as the model state in the calculation of the adjoint gradients, calculated according to Equation (2.19). The "daytime only" simulation assimilated observations only between 0800-2000h local time, in an attempt to avoid known issues with boundary layer mixing at night. Finally, the "multiple rates" simulation expanded the size of the control vector to include other reaction rates than just ozone dry deposition. This is done to assess the magnitude of error induced by correcting the entire surface ozone bias by adjusting ozone deposition rates alone. The additional reactions were chosen based on the sensitivity analysis presented in Section 4.3, and are O_3+NO, N_2O_5 hydrolysis, formation of nitric acid (NO_2+OH), and formation of isoprene nitrate(RIO_2+NO). Technically, this is accomplished by extending the size of the control parameter vector $\mathbf{c}$ to include scale factors for these additional reactions.

Table 4.2: Inversion parameters for surface ozone studies.

Simulation	Control parameters	Observation times	PBL bias removal
Baseline	O_3 dry deposition only	all day	no
PBL corrected	O_3 dry deposition only	all day	yes
Daytime only	O_3 dry deposition only	0800-2000h	no
Multiple rates	5 reaction rates	all day	no

Scale factors for ozone dry deposition rates in the baseline inversion are shown in Figure 4.12. Recall that the scale factors calculated in the inversion are three-dimensional. To get the change to the column rate, let the rate of deposition in the a priori simulation at vertical level l be $r_0(l)$. Here, we have dropped the indices i and j, with the understanding that these calculations are done for all latitudes and longitudes. A scale factor c modifies this rate,

$$k(l) = c(l)k_0(l). \tag{4.9}$$

The total deposition rate in a column k_T will be the sum of $k(l)$ over the column. If we define a scale factor for the column deposition rate c_T,

$$c_T \equiv \frac{k_T}{k_{T,0}} = \frac{\sum_{l=0}^{l_{max}}(c(l)k_0(l))}{\sum_{l=0}^{l_{max}}(k_0(l))}. \tag{4.10}$$

The baseline inversion results suggest a large increase to the dry deposition rate along the Ohio River Valley (roughly 40°N, 81°W to 37°N, 88°W), which coincides with some of the strongest a priori ozone biases. Figure 4.13 shows that the inversion over-corrects in this region, resulting in a negative ozone bias in the a posteriori emissions. The timeseries of mean ozone in the baseline inversion (the dark blue line in Figure 4.14) shows that this negative bias is strongest at night.

The nighttime values of planetary mixing layer heights in GEOS-Chem are a potential source of problems. Two inversion experiments were implemented to circumvent the nighttime mixing issues: the "daytime only" experiment and the "PBL corrected" experiment. In the former, observations during the night are excluded from the analysis. The result, seen in Figure 4.14 and Table 4.3, is that the inversion performs more poorly (characterized by a higher value of reduced chi-squared, χ^2/n, a measure of inversion performance), and is unable to reconcile the simulation to the afternoon observations. In the latter experiment, a time-varying bias correction is applied to the ozone concentrations every three hours used in the adjoint forcing, in an attempt to bring them in line with the non-local mixing scheme. This results in a small residual bias during both the afternoon and nighttime extrema.

Finally, the "multiple rates" experiment explores the likely case that not all of the a priori ozone bias is due to the ozone deposition rate alone, and attempts to constrain several of the relevant reaction rates simultaneously. The control vector was expanded to include reaction rates for the following reactions, with uncertainties given

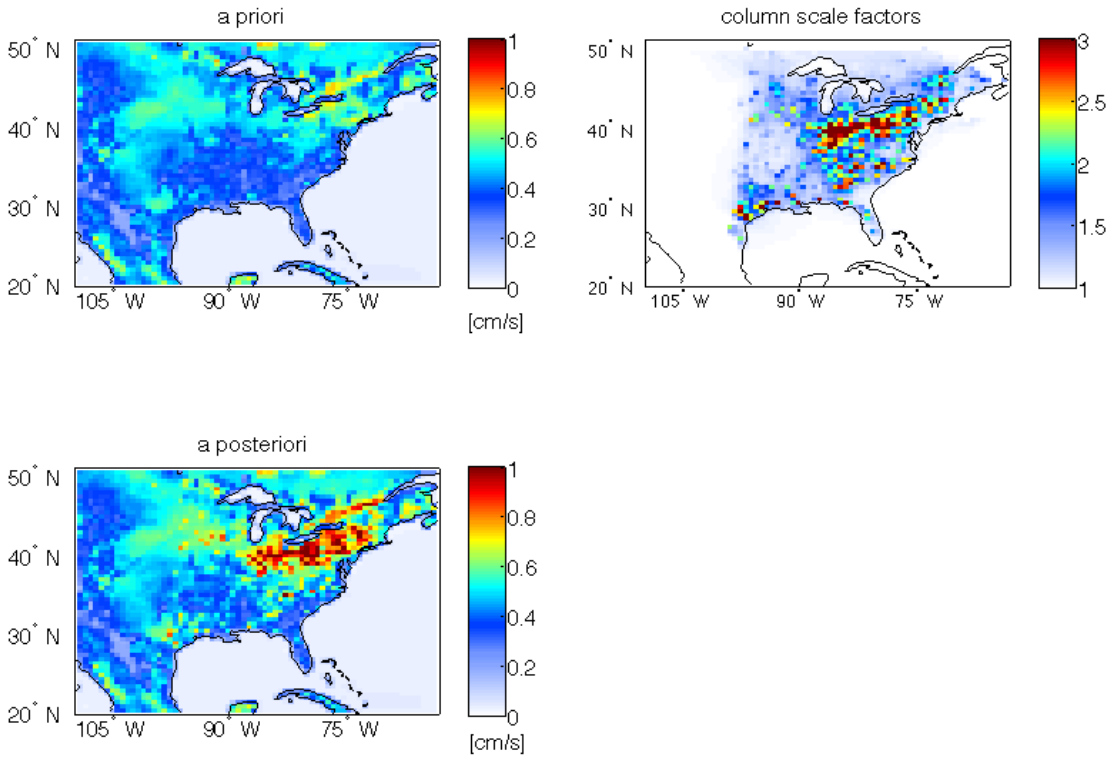

Figure 4.12: Ozone dry deposition from the baseline inversion for the first ten days of August 2006. The a priori ozone dry deposition velocity (top left) is multiplied by the column scale factors (top right) to obtain the a posteriori dry deposition velocities (bottom left).

in brackets: O_3+NO (10%), NO_2+OH (50%), RIO_2+NO (100%), and N_2O_5 hydrolysis (200%) [*Sander et al.*, 2011]. This experiment bears out the large sensitivity to ozone dry deposition, in that the resulting ozone a posteriori biases are in the same direction as those in the baseline case, and the difference between the biases for these two simulations is smaller than for other simulation pairs. The O_3+NO reaction has a similar amount of sensitivity to surface ozone concentrations, but is less uncertain and so is not as strongly affected in the inversion.

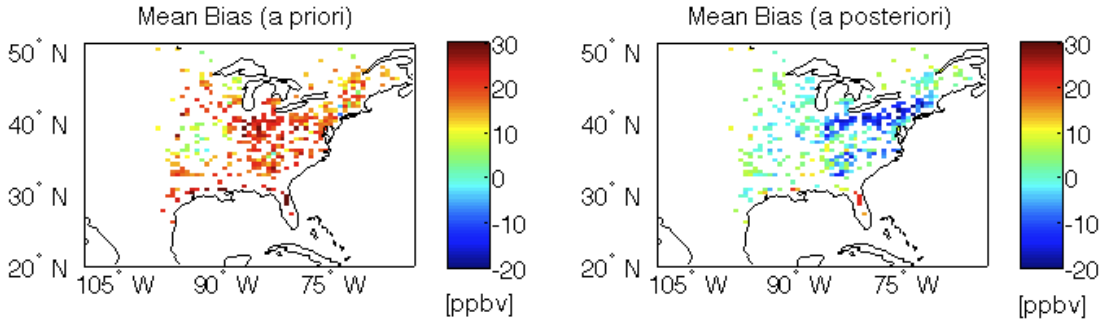

Figure 4.13: Ozone mean bias relative to surface network observations in the baseline inversion, comparing the a priori bias (left) to the a posteriori bias (right).

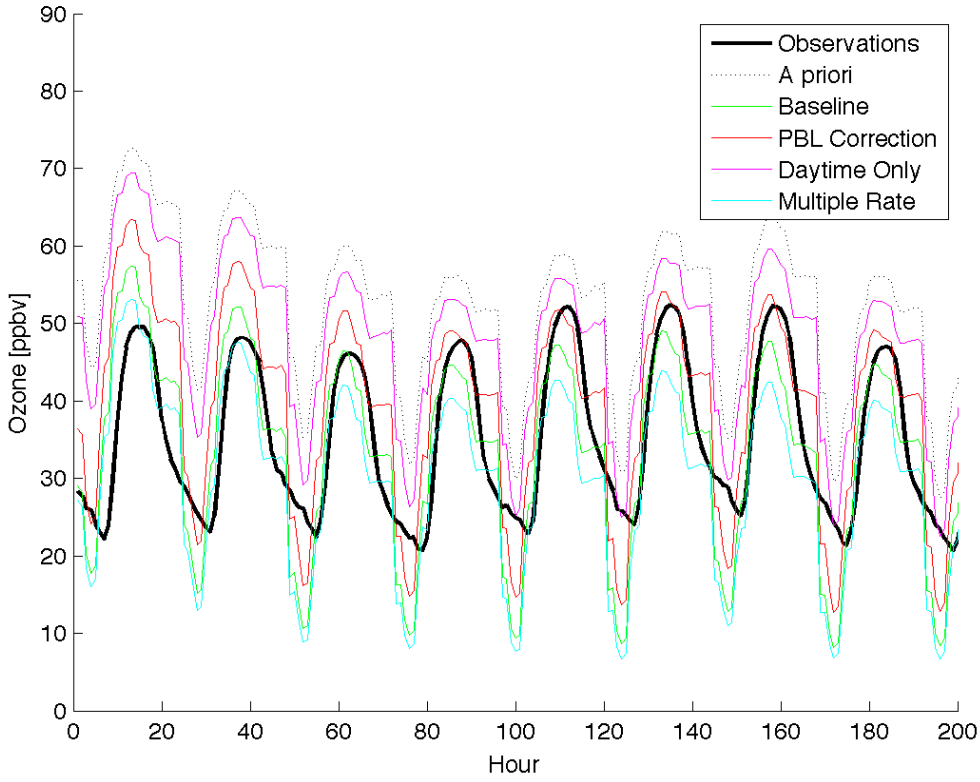

Figure 4.14: Time series of 3-hourly mean ozone for various inversion experiments. The time axis begins at midnight on August 1, 2006.

Table 4.3: Error metrics for various inversion experiments. The bias (model − observation) and root-mean-squared-error (RMSE) are given in units of ppbv.

Simulation	χ^2/n	Bias	RMSE
A priori	5.5	17.0	22.7
Baseline	2.4	-1.3	16.9
Daytime only	3.8	12.8	19.4
PBL corrected	2.5	5.6	16.8
Multiple rates	2.5	-5.1	17.0

4.5 Conclusions

This analysis examined surface ozone in the GEOS-Chem model from the perspective of biases not related to transport from the free troposphere. A persistent positive bias in simulated surface ozone over the eastern U.S. in summer was not improved by moving to a higher horizontal resolution ($0.5^\circ \times 0.666^\circ$), although an improvement of 3.9 ppbv in the mean bias was achieved by using an updated boundary layer mixing scheme [*Lin and McElroy*, 2010].

Sensitivity studies using a high-resolution nested adjoint model over the North American domain show, at the model resolution, the parameters most strongly linked to surface ozone observations. Precursor emissions such as anthropogenic NO_x and biogenic isoprene, while strongly linked to surface ozone concentrations, require unreasonable adjustments in order to match the observations. In the case of anthropogenic NO_x, continental total emissions must be lowered from 0.43 Tg N/month to 0.25 Tg N/month, with reductions over urban regions in the eastern U.S. that do not match observed NO_2 distributions. Similarly, adjusting isoprene emissions to match observed surface ozone requires an increase in biogenic emissions to 7.7 Tg C/month, almost twice that of recent estimates (3.7–4.1 Tg C/month [*Guenther et al.*, 2006; *Millet et al.*, 2008]).

The adjoint model sensitivities also highlight the importance of key chemical sink reactions on surface ozone abundances. Specifically, they showed the greatest sensitivity to ozone dry deposition and the O_3+NO reaction. The latter reaction is reasonably well-constrained [*Sander et al.*, 2011]. The dry deposition rate, however, is highly parameterized with potential uncertainties up to a factor of three [*Schwede et al.*, 2011].

An inversion constraining ozone dry deposition rates is able to significantly reduce the model bias relative to surface ozone observations, from 17.0 ppbv to 5.6 ppbv. This inversion suggests a factor of three increase in dry deposition velocities south of the Great Lakes, where the initial model-measurement mismatch is greatest.

Updates to model chemistry have significant implications for the sensitivity of ozone to isoprene [*Lelieveld et al.*, 2008; *Mao et al.*, 2013]. The simulations of *Mao et al.* [2013] seem to agree well with aircraft observations of ozone near the Great Lakes, but retain a high bias in the southeastern U.S. This suggests a certain complimentarity of the approach described here with the updates to isoprene chemistry, as ozone deposition provides a plausible alternative sink of ozone in the southeastern U.S. Furthermore, *Mao et al.* [2013] assume an uptake efficiency for HO_2 on aerosols of 1, which is larger than is generally assumed [*Thornton et al.*, 2008], that serves to reduce ozone in their simulation; increases to deposition offer a viable sink without the need for such strong uptake.

Most likely, changes to both precursor emissions and chemical sinks will be needed to match the observed concentrations. Using the 4D-Var inversion approach to simultaneously constrain both sources and sinks of ozone is possible, but would require additional observations. If both emissions and sink reaction rates are constrained using only surface ozone observations, the solution becomes subject to instabilities, as many values of emissions and sink rates can result in the same ozone concentration. An additional independent source of information, such as NO_2 observations, would be required to resolve the potential for larger emissions to compensate for larger sink values. Such an inversion could constitute a future research project.

Chapter 5

Assimilation of Free Tropospheric Ozone to Constrain the Horizontal Distribution of Lightning NO_x Emissions

5.1 Introduction

The preceding two chapters discuss ozone in the Arctic and in the midlatitude PBL, where the abundance of ozone is influenced by transport from the midlatitude free troposphere. However, ozone production in the free troposphere depends strongly on NO_x emissions from lightning, the global distribution of which remains uncertain [*Schumann and Huntrieser*, 2007]. As described in Chapter 2, *Parrington et al.* [2008] suggested that the underestimate of tropospheric ozone, shown in Figure 1.2, was due to an underestimate of lightning NO_x emissions. *Hudman et al.* [2007], using aircraft observations from the ICARTT campaign, estimated the lightning NO_x source in the version of GEOS-Chem employed by *Parrington et al.* [2008] was too low by about a factor of four. This

chapter focuses on the use of ozonesonde data to quantify the lightning NO_x source over North America.

A common parameterization in CTMs uses the empirical relationship between the fifth power of cloud-top height and lightning flash rate [*Price and Rind*, 1992] together with an assumption about the NO_x yield per flash to estimate the emissions rate. Observations of lightning flash locations from satellites [*Sauvage et al.*, 2007] and from ground-based networks [*Allen et al.*, 2010, 2012] have been used to refine these estimates, but the NO_x yield per flash remains uncertain and seems to vary from storm to storm [*DeCaria et al.*, 2005; *Huntrieser et al.*, 2008, 2009, 2011].

Top-down estimates of the lightning NO_x source have been obtained from satellite observations of NO_2 columns at both global [*Martin et al.*, 2003b, 2007] and regional [*Sauvage et al.*, 2007; *Stavrakou et al.*, 2008; *Lin*, 2012] scales. These estimates are limited in spatial resolution (e.g., $5^\circ \times 5^\circ$ in *Stavrakou et al.* [2008]), and the lightning signal in the column satellite observations can be difficult to distinguish from other natural emissions sources [*Lin*, 2012]. Inferences about lightning NO_x emissions on continental scales have also been drawn from comprehensive composition measurements from aircraft platforms [*Hudman et al.*, 2007; *Cooper et al.*, 2009]. However, the precise distribution of lightning NO_x emissions remains a source of uncertainty in the upper tropospheric oxidant budget.

The IONS-06 campaign provides a set of high precision observations of ozone at a near-daily time scale across North America [*Thompson et al.*, 2008]. This valuable dataset has been employed in numerous studies, several of which attribute a significant fraction of the tropospheric ozone profile to recent lightning activity [*Pfister et al.*, 2008; *Cooper et al.*, 2009]. Here, the IONS-06 ozone data will be assimilated into a CTM using a 4D-Var data assimilation framework to produce a grid-scale estimate of the lightning NO_x emissions distribution.

A wealth of observational data made available by satellite measurements has led researchers to attempt to improve constraints on the global distribution of lightning NO_x emissions [*Martin et al.*, 2007; *Stavrakou et al.*, 2008]. Observations with high vertical resolution are particularly valuable, and have been shown to provide information on trace gases in the upper troposphere that complements column observations [*Pak and Prather*, 2001]. However, the interplay of emissions, chemistry, and transport that impact ozone abundances in the upper troposphere necessitates a careful assessment of how well these tracer abundances are represented in the observational data sets.

The SOAR mission was proposed as a concept study to the Canadian Space Agency in 2007 and the study results were submitted in 2009. The payload was designed to measure atmospheric composition of both trace gases and aerosols through solar occultation [*Walker et al.*, 2009], and consisted of three instruments. The infrared Fourier transform spectrometer instrument design aimed for a vertical resolution of 2 km or better in the upper troposphere, similar to the model vertical resolution at that altitude. One of the science objectives for the proposed SOAR mission was a better understanding of the chemistry and dynamics of trace gases in the free troposphere [*Walker et al.*, 2009]. Lightning plays a key role in the partitioning of total reactive nitrogen and ozone production in the upper troposphere, and needs to be well-quantified. In support of this objective, an observing system simulation experiment (OSSE) using the GEOS-Chem CTM to produce pseudo-observations that an occultation instrument such as that proposed for the SOAR mission could provide was performed to assess these observations' capacity to constrain the global lightning NO_x source.

Section 5.2 details the global CTM used in this study, the specification of boundary conditions for the regional simulation, and the adjoint model used to perform the inversion. It also describes the ozonesonde data being ingested into the inversion and independent data used for validating the results. Section 5.3 describes inversion tests executed with the global and regional models, and presents results of a 4D-Var inversion

using the IONS-06 data. Section 5.4 outlines inversion tests to integrate space-based observations into the 4D-Var framework and their potential to constrain the lightning emissions source. Section 5.5 discusses the impacts of the assumptions that go into the inversion methods, as well as the sensitivity of the results to these assumptions.

5.2 Components of the Inversion Study

5.2.1 Chemical Transport Model Set-up

The same nested version of GEOS-Chem (v9-01-02) is used here as was described in Chapter 4, driven by GEOS-5 assimilated meteorological fields. Table 5.1 lists the total NO_x, CO, and isoprene emissions for the nested domain (13–57°N, 66–126°W) from various sources. The simulated lightning flash distribution is estimated according to the cloud-top height parameterization of *Price and Rind* [1992] and then scaled to match the observed distribution of lightning flashes in a 10-year climatology of Optical Transient Detector and Lightning Imaging Sensor observations [*Murray et al.*, 2012]. The OTD-LIS rescaling may be switched off to use the unmodified cloud-top height parameterization. In both of these cases, the midlatitude emissions per flash are enhanced compared to those in the tropics [*Murray et al.*, 2012]. Within the column, lightning emissions are distributed vertically according to profiles calculated by *Ott et al.* [2010].

5.2.2 Ozonesonde Data

Ozonesondes provide a high-quality, high-vertical-resolution profile sounding of ozone throughout the troposphere and lower stratosphere. Networks of ozonesondes have been used to enhance large-scale experiments and provide excellent validation datasets for satellite instruments and chemical models. One such network was the IONS-06 campaign, which saw the coordinated launch of over 400 soundings from 21 North American locations (including one ship-based platform) during August 2006 [*Thompson et al.*,

Table 5.1: Total emissions for August 2006 (in Tg N, Tg CO, or Tg of isoprene) over the North American nested domain, and adjoint sensitivities (in percent) of the ozone at the IONS-06 observing locations to this type of emission averaged across the domain.

Source	A priori emissions	Sensitivity
Lightning NO_x	0.26	8.71
Anthropogenic NO_x	0.50	10.41
Soil NO_x	0.11	1.94
Biomass burning NO_x	0.0099	0.15
Biofuel NO_x	0.0067	0.13
Aircraft NO_x	0.015	0.44
Anthropogenic CO	7.34	0.54
Biomass burning CO	0.74	0.03
Biofuel CO	0.56	0.03
Biogenic Isoprene	7.0	-1.73

2008]. Figure 5.1 shows the locations and frequency of soundings at sites within the nested model domain during August. The launches in the Gulf of Mexico were from the R/V Ronald H. Brown ship-board platform. The Sable Island site falls outside the model domain, leaving a total of 379 soundings in August for use in the assimilation.

5.2.3 Independent Validation Data

Measured ozone profiles from the civilian aircraft MOZAIC (Measurements of OZone and water vapour by in-service AIrbus airCraft, http://mozaic.aero.obs-mip.fr/) project [*Thouret et al.*, 1998] are used here to provide an independent means of validating the inversion results. The number of flights from each MOZAIC location used in this study is shown in Table 5.2. The measurements use a commercial UV absorption instrument deployed on

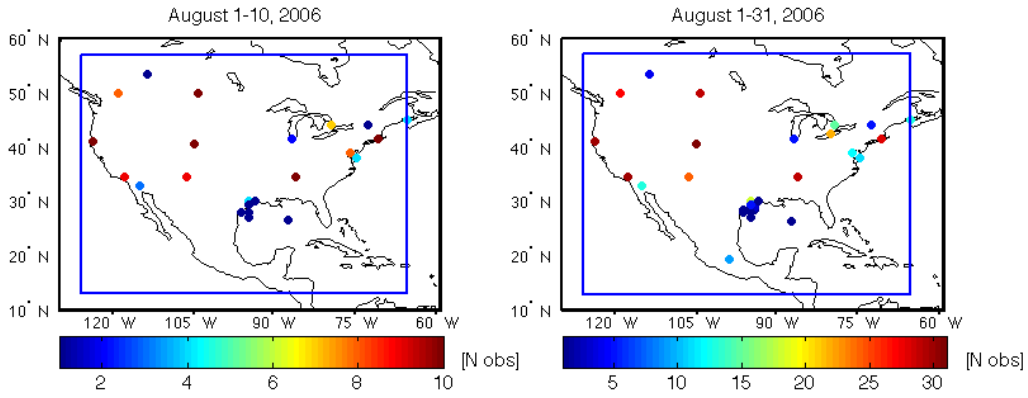

Figure 5.1: Locations of the IONS-06 ozonesonde launches during the first ten days (left), and the full month of August 2006 (right) on the nested GEOS-Chem grid. The colour scale indicates the number of launches in a particular grid box. The boundaries of the nested grid domain are outlined in blue.

long-range civilian aircraft and vertical soundings are accrued automatically during take-off and landing of intercontinental flights. The accuracy is estimated at ±(2 ppbv + 2%) for each 4 second measurement [*Thouret et al.*, 1998]. For comparison to the GEOS-Chem model, data from aircraft ascents and descents are averaged onto the GEOS-5 vertical grid.

5.2.4 Inversion Approach

The analyses presented here use the full chemistry adjoint of GEOS-Chem on both the global 4° × 5° domain and on a nested domain at 0.5° × 0.666° resolution [*Jiang*, 2012]. The nested domain covers the continental U.S. and southern Canada (13–57° N, 66–126° W) and is shown as a blue box in Figure 5.1. The adjoint of GEOS-Chem operates using the same meteorology and emissions data as the standard GEOS-Chem model.

Table 5.2: Locations of MOZAIC ascent and descent profiles used in this study, as well as the number of flights during August 2006 at each location.

Location	Latitude	Longitude	# of Flights
Atlanta, GA	33.6° N	84.4° W	10
Boston, MA	42.4° N	71.0° W	4
Dallas, TX	32.9° N	97.0° W	12
Philadelphia, PA	49.9° N	75.2° W	8
Portland, OR	45.6° N	122.6° W	16

For adjoint inversions using ozonesonde measurements, the cost function J is defined with terms accounting for the error-weighted difference between the simulated and observed ozone concentrations, as well as with a penalty term accounting for deviations of the optimized model parameters from their a priori values,

$$J = \frac{1}{2}\Big(\sum_{n=0}^{N}(\mathbf{x}-\mathbf{x}^{obs})^T\mathbf{S}_{obs}^{-1}(\mathbf{x}-\mathbf{x}^{obs}) + \gamma(\mathbf{c}-\mathbf{c}_0)^T\mathbf{S}_a^{-1}(\mathbf{c}-\mathbf{c}_0)\Big). \quad (5.1)$$

Here, $\mathbf{x}$ and $\mathbf{x}^{obs}$ are vectors of simulated and observed profile ozone concentrations at the ozonesonde times and locations. $\mathbf{c}$ and $\mathbf{c}_0$ are vectors of the optimized and a priori linear scale factors applied to grid-scale lightning NO_x emissions. $\mathbf{S}_{obs}$ denotes the error covariance matrix of the observations, and $\mathbf{S}_a$ the background error covariance matrix. γ is a regularization parameter that weights the relative importance of the two terms, and is set to $\gamma = 1$ here. Only observations between 4 km and the tropopause are included in the cost function, and scale factors on the lightning emissions are likewise limited to these altitudes. This prevents the optimization from being dominated by large adjoint gradients near the top of the boundary layer, where simulated ozone values are known to be biased [*Parrington et al.*, 2009]. Corrections to ozone in the boundary layer ozone were addressed previously in Chapter 4 and are not considered in this analysis.

A monthly scale factor for lightning NO_x emissions is optimized for every column in the model domain. The a priori vertical distribution from *Ott et al.* [2010] is taken as correct. The impact of only optimizing emissions in the horizontal plane is discussed in Section 5.5. The a priori lightning emissions in each column are assigned a 100% error, that is, the diagonal elements of $\mathbf{S}_a$ are set equal to $\mathbf{c}_0$. This magnitude of error is similar to that used in other inversion studies that address lightning emissions [*Stavrakou et al.*, 2008; *Lin*, 2012]. No horizontal correlation in the a priori errors is assumed.

For assimilation into the adjoint model, IONS-06 observations are averaged onto the GEOS-5 vertical grid, which in the free troposphere has spacing between 100–500 m, larger than the ozonesonde effective resolution. No vertical or horizontal correlations are accounted for in the observation covariance matrix (i.e. $\mathbf{S}_{obs}$ is a diagonal matrix). Data are assimilated in the adjoint simulation at the nearest hour to the launch time, which is typically early afternoon local time.

Previous studies identified significant influence of stratosphere to troposphere transport in the IONS-06 data [*Cooper et al.*, 2007; *Bourqui and Trépanier*, 2010]. Given the known bias in ozone concentrations in the lower stratosphere of GEOS-Chem (see Figure 5.3), it is important to identify observations impacted by the stratosphere to avoid aliasing biases in the lower stratosphere into the inversion and affecting the estimate of lightning emissions. Based on the relative coherence of ozone to relative humidity (RH) ratios within dry, ozone-rich stratospheric intrusions observed by *Bourqui et al.* [2012], this ratio is used to filter out ozonesonde data that displays stratospheric character in the troposphere. Sonde data points with an O_3:RH ratio greater than 10 ppbv O_3 to 1% RH are removed prior to averaging. Any model cells where more than 20% of the observation data are removed by this filter are not included in further analysis. The number of points removed is not very sensitive to this percentage, indicating that the resolution is fine enough that grid cells are either primarily tropospheric or stratospheric in character. This filter removes 1882 out of 12612 model grid cells from the analysis

(∼15%). The cut-off ratio of 10 ppbv O_3 to 1% RH is chosen conservatively to retain as much data as possible for the inversion, while removing points that might be influenced by the model bias in the upper troposphere and lower stratosphere (UTLS).

Another filter was applied to condition the data to be near to the initial model state. Any profiles with averaged observed ozone values less than 10 ppbv were removed as being unphysical, which occurred in one profile. Also, if the square of the model minus sonde difference divided by the observation covariance exceeded 20, the point was removed as an outlier. This filter removed an additional 296 model grid cells in 119 profiles from the analysis (∼2% of the total number of grid cells containing observations).

5.2.5 Chemical Boundary Conditions

The main analysis in this chapter will be conducted using the nested regional version of GEOS-Chem since air quality studies require horizontal resolution that is better than is typically available in global models. However, regional models require lateral boundary conditions, which can impact the high-resolution air quality simulation. To demonstrate the importance of the lateral boundary conditions, a global analysis, focused regionally on North America, is also presented. If a global model is used to specify the boundary conditions, any biases in the global model free troposphere are generally transmitted to the regional model [*Tang et al.*, 2007]. Similarly, interpolation of observation-based boundary conditions onto the model grid can introduce biases, especially near large concentration gradients such as at the tropopause [*Pour-Biazar et al.*, 2011]. Furthermore, biases above the regional model ceiling can introduce biases in the upper troposphere [*Tang et al.*, 2009]. The effect of the boundary conditions is generally stronger in the free troposphere than in the planetary boundary layer. However, *Pfister et al.* [2011] found that using different ozone boundary conditions could impact simulated surface ozone in a regional model by ±15 ppbv. Essentially, regional model boundary conditions produce

a background concentration field of long-lived species (e.g., ozone, CO) on top of which variations due to the regional model chemistry are superimposed [*Tang et al.*, 2007].

In studies of the impact of boundary conditions on regional simulations, the best model performance is obtained when time-varying, observation-based boundary conditions are used [*Tang et al.*, 2009; *Huang et al.*, 2010; *Pour-Biazar et al.*, 2011]. In this study, two global full chemistry simulations are performed for 2006 with GEOS-Chem v9-01-02 to produce chemical initial and boundary conditions for the regional simulations. One is the free-running model, while the other uses a suboptimal sequential Kalman filter to assimilate tropospheric ozone and CO profiles from TES, as described in Chapter 2 and in *Parrington et al.* [2008]. The lateral boundary conditions are archived during the full chemistry runs and updated in the regional simulations every three hours.

The TES assimilation has already been shown to improve the ozone simulation in some regions, but a comparison across northern midlatitudes is needed to assess its suitability as boundary conditions to the regional model. Figure 5.2 shows the median bias in ozone averaged between the model boundary layer and the tropopause relative to ozonesonde measurements from selected WOUDC sites [*Environment Canada et al.*, 2009]. At most North American sites, the median bias is less than 15 ppbv, with the model biased high relative to the sondes. The model does have a low bias relative to the Middle Eastern site of Isfahan. In general, the assimilation of TES profiles increased simulated free tropospheric ozone concentrations by 2–3%, with the largest differences between the two simulations over North America reaching 3.7 ppbv. The correction due to the assimilation is smaller with this model version than in previous studies, and the biases relative to the median of the ozonesonde observations are small, both of which give confidence in the fidelity of the assimilated ozone field.

Using this assimilated ozone field as boundary conditions improves on previous studies by integrating consistent global and regional models, thus mitigating the need to interpolate to a different vertical grid which can introduce biases [*Pour-Biazar et al.*, 2011].

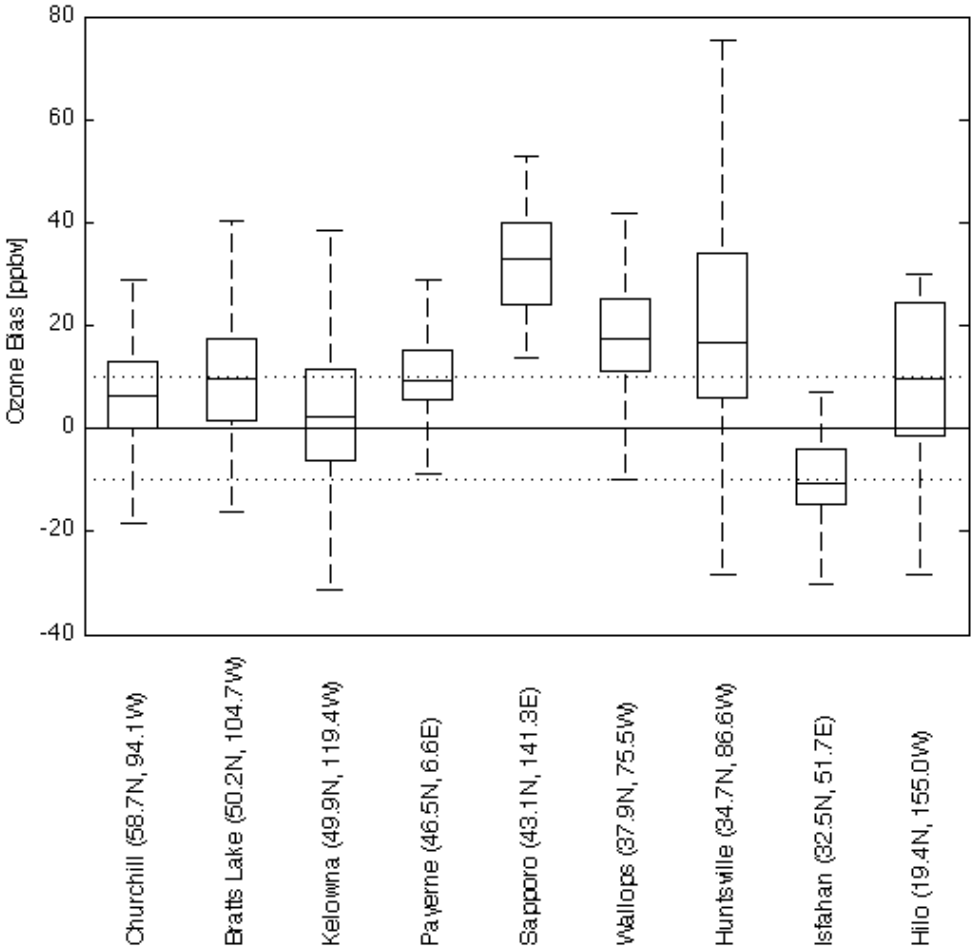

Figure 5.2: Absolute bias between GEOS-Chem with assimilated TES ozone profiles and ozonesondes between the model boundary layer and the tropopause in August 2006 for various northern midlatitude WOUDC stations. For each station, the central line denotes the median bias, while the box marks the quartile ranges. The dashed error bars encompass more than 99% of the points included in the bias calculation. Dotted lines indicate ± 10 ppbv.

Also, by accounting for both model and observation errors in a formal data assimilation system instead of an ad hoc interpolation of observations to the model grid, we avoid the introduction of new biases in the transition from the global model to the regional simulation [*Tang et al.*, 2009; *Huang et al.*, 2010].

In the framework described above, TES profiles are only assimilated in the troposphere where the model is performing a full chemistry simulation. In the stratosphere, ozone tendencies are calculated by a first-order relaxation to a climatology of ozone and temperature observations (LINOZ, *McLinden et al.* [2000]). Concentrations from the two different chemistry domains are advected and mixed in the UTLS region according to the prescribed meteorological fields. The UTLS constitutes an upper boundary on the full chemistry domain. We evaluate the model ozone fields in the UTLS by comparing to an assimilation of MLS and OMI ozone observations into the GMAO GEOS-4 ozone simulation [*Stajner et al.*, 2008]. The tropospheric simulation in the GMAO product uses a recent version of GEOS-Chem (v7-04), so we expect differences between our simulations and the GMAO product to be driven mainly by the observational constraints on the troposphere and lower stratosphere from TES in the GEOS-Chem simulation, and from MLS and OMI in the GMAO product.

Figure 5.3 compares vertical profiles in the UTLS between our GEOS-Chem simulations (in red) and the GMAO assimilation (in blue) over three latitude bands spanning North America in August 2006. Note that the GEOS-4 (blue) and GEOS-5 (red) vertical grids differ. The GMAO assimilation captures the mean profiles seen by ozonesonde and aircraft profile data. GEOS-Chem with LINOZ also produces the correct ozone concentrations in the UTLS at low latitudes within ±20%. In the high midlatitudes, the GEOS-Chem concentrations are biased low by up to 41% compared to the ozonesondes. Ozone at the tropopause also exhibits the greatest variability in the higher latitude band, consistent with recent observational studies [*Hegglin et al.*, 2010; *Tilmes et al.*, 2010]. Correcting the low bias in the GEOS-Chem extratropical lower stratosphere is be-

yond the scope of this work, but the filtering described in the previous section attempts to avoid transmitting this bias into the inversion analysis.

5.3 Testing the Inversion Set-up

Table 5.1 shows the total sensitivity of the IONS-06 observations in the free troposphere to each type of emissions listed, calculated from an adjoint sensitivity study in a similar way to those in Figure 3.10. The largest adjoint sensitivities here are to the lightning and anthropogenic NO_x sources. Even though the anthropogenic source is nearly double the lightning source, the observations have an 8.7% sensitivity to lightning compared to a 10.4% sensitivity to anthropogenic NO_x. This reinforces the idea that the magnitude and distribution of lightning emissions over North America plays a significant role in determining the free tropospheric ozone distribution, as observed by the IONS-06 network.

5.3.1 Global Inversion Analysis

An OSSE was performed in which the GEOS-Chem parameterization of lightning NO_x emissions, rescaled to OTD-LIS, was used to simulate a modelled ozone field that was taken as the true state. Pseudo-observations were generated by sampling this true state at the launch times and locations of the IONS-06 observations (Figure 5.1). A factor of two perturbation was applied to the initial estimate of the global lightning emissions in the adjoint inversion to produce an incorrect a priori estimate of the lightning source. The objective of the analysis was to assimilate the pseudo-observations, starting from the incorrect a priori, to recover the emissions used in producing the true state. Errors of 10% and 100% were assigned to the observations and initial emissions estimate, respectively. The ratio of the true to constrained emissions after a one-month inversion analysis of the pseudo-observations is shown in Figure 5.4.

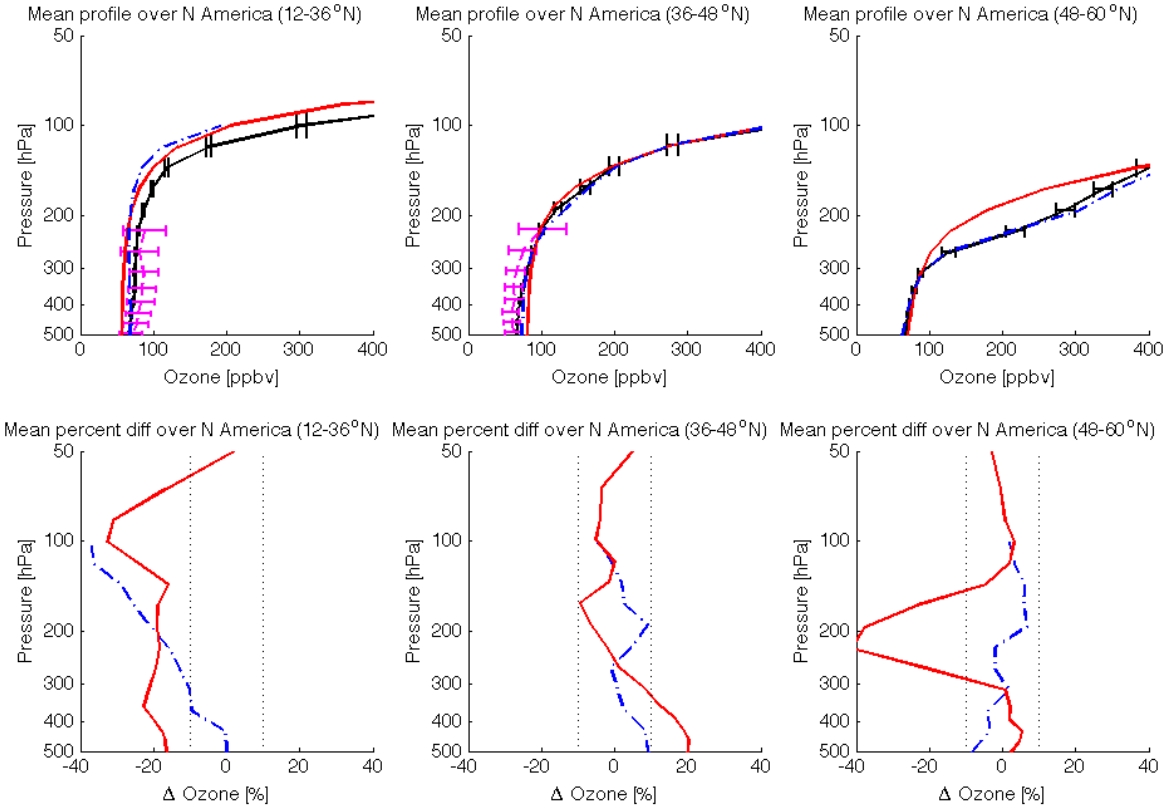

Figure 5.3: Comparison of vertical profiles above North America (65–125° W) in August 2006 averaged across three latitude bands (left, 12–36°N; middle, 36–48°N; right, 48–60°N). Mean profiles are shown in the top row in thick lines for GEOS-Chem (solid red), GMAO assimilation (dash-dotted blue), ozonesondes (solid black), and MOZAIC (dashed magenta). Horizontal error bars represent the standard deviation of the individual ozonesonde or aircraft profiles around the mean. The percent difference between both models (GEOS-Chem and GMAO) and the ozonesonde profiles, calculated with respect to the ozonesondes, for each latitude band is shown in the bottom row.

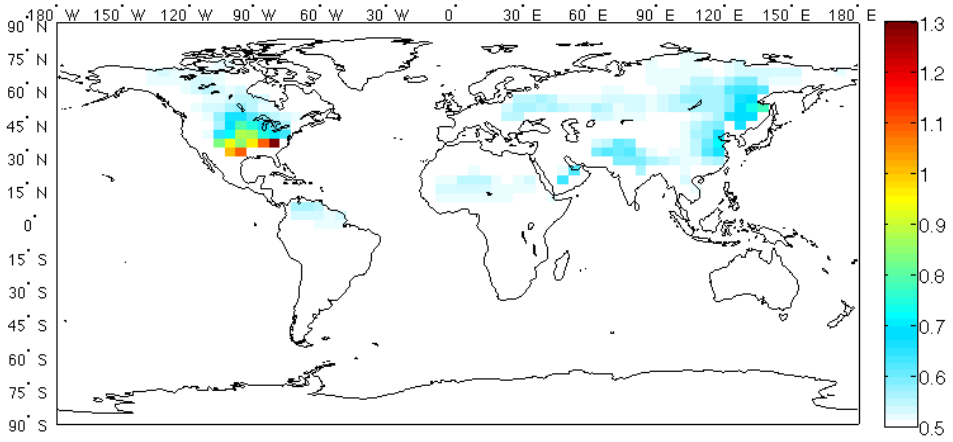

Figure 5.4: Ratio of true to constrained lightning NO_x emissions for the OSSE using IONS-06 pseudo-observations.

The North American network of observations provides the strongest constraint over the southeastern part of the continent where lightning emissions are high. Over the month-long simulation, the influence of the observations is transported upwind across the Pacific to decrease the Eurasian source. The global lightning emissions recovered by this inversion total 1.71 Tg N (186% of the true emissions). Total North American emissions after the inversion were 0.51 Tg N (171% of the true North American total).

Ratios greater than one indicate that the adjoint inversion is decreasing the emissions locally beyond their true value. This is an expedient way for the optimization to match the low observed ozone values locally to compensate for the larger background concentrations being transported from upwind areas (e.g., western North America) where the true emissions have not been fully recovered. The large local reduction in emissions is possible because there are no observations downwind (e.g., over the Atlantic Ocean or in Europe) to constrain the outflow from eastern North America. This experiment stresses the importance of having a solid constraint on background ozone transport, especially when dealing with spatially heterogeneous observations.

5.3.2 Regional Inversion Analysis

The OSSE described above was repeated using the high-resolution regional model to test its suitability for assimilating IONS-06 observations to constrain lightning NO_x emissions at the continental scale. As with the global OSSE, pseudo-observations were generated from the true ozone field by sampling the model at the times and locations of the IONS-06 observations. The inversion was then initialized with an a priori estimate that was 1.5 times the true emissions (Figure 5.5). The error values assigned to the pseudo-observations and the a priori lightning emissions were 10% and 100%, respectively.

The inversion, starting from a total 0.397 Tg N, recovers a total of 0.334 Tg N for lightning emissions, where the true total is 0.264 Tg N. When the inversion was repeated starting from an a priori of 0.132 Tg N (half the true emissions), the a posteriori value was 0.204 Tg N, suggesting that the inversion can recover the true estimate to within about 25%. Figure 5.5 shows that the true distribution is underestimated in the southwestern U.S. and along the Gulf Coast, but overestimated across much of the northern part of the country. Figure 5.6 shows the ratio of true to a posteriori emissions. Deviations from the 1:1 line represent instances where the inversion fails to recover the true emissions from the information contained in the pseudo-observations. Points where the recovered emissions are equal to the a priori fall along the 3:2 line.

Figure 5.6 shows the ratio of true to a posteriori emissions for two inversion time frames: 10 days and 30 days. In the 30-day inversion, most regions with high emissions are well-corrected, and fall near the 1:1 line, while the lower part of the emissions distribution is less well-corrected. Grid cells that are far from the observations, for instance those at very high or very low latitudes, also fall closer to the a priori than to the true emissions. The 10-day inversion still has many uncorrected grid cells with high emissions, suggesting that the observations over the shorter time frame do not contain enough information to properly constrain the major features of the emissions distribution.

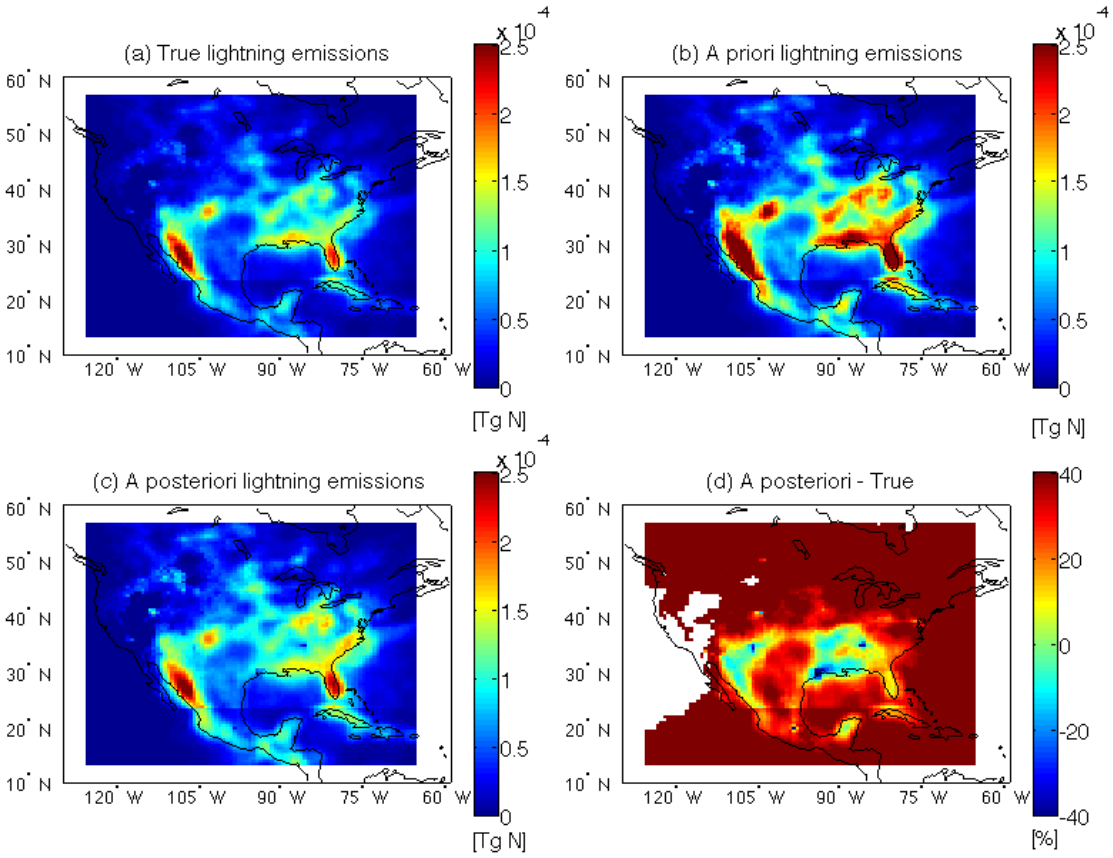

Figure 5.5: Lightning NO_x emissions in the regional OSSE. The true emissions (a) are from the standard parameterization in GEOS-Chem, and are used to generate the ozone field from which pseudo-observations are taken (see description in text). The a posteriori emissions (c) result from an inversion using these pseudo-observations starting from an a priori guess of emissions (b) that is 1.5 times the true emissions. The percent difference between the a posteriori and true emissions is shown in (d). White pixels in (d) indicate regions where there are no lightning NO_x emissions.

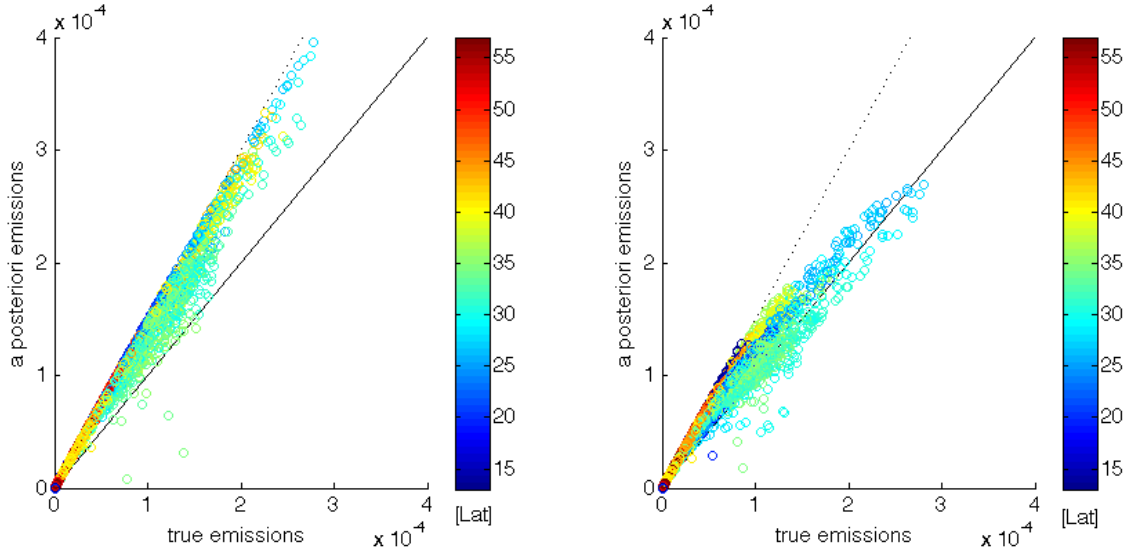

Figure 5.6: Ratios of true to a posteriori emissions for the OSSE at each horizontal grid cell in the domain. The left and right panels contain results from 10-day and a 30-day simulation periods, respectively. Lightning NO_x emissions were perturbed by a factor of 1.5. The colour scales indicate latitude. The solid black line is the 1:1 line, and the dotted black line is the 3:2 line.

5.3.3 Inversion Analysis of IONS-06 Data

Adjoint inversions using the actual observations from the IONS-06 campaign were carried out in the high-resolution nested model for August 2006. As in the OSSE described in the last section, the boundary conditions were provided from a simulation that assimilated TES ozone profiles. A 100% error was assumed for the a priori lightning emissions, and a 15% error was used for the IONS-06 observations. Two different distributions were tested for the a priori lightning NO_x emissions: a distribution scaled to the OTD-LIS flash climatology [*Murray et al.*, 2012], and the unscaled cloud-top height parameterization of *Price and Rind* [1992]. Figure 5.7 displays the lightning emissions resulting from both inversions. The domain-wide total emissions for this period were reduced from 0.264 Tg N to 0.203 Tg N in the inversion with the OTD-LIS a priori. In the inversion

with the Price and Rind a priori distribution, total emissions increased from 0.066 Tg N to 0.076 Tg N.

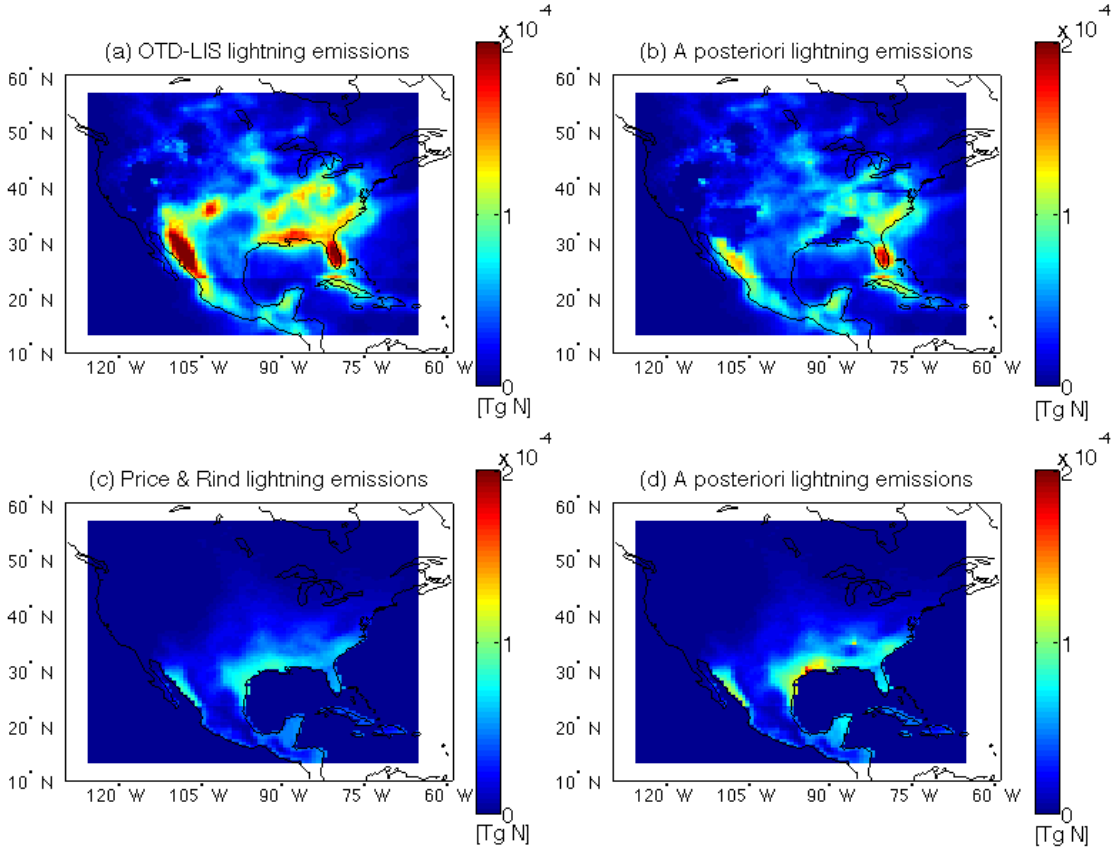

Figure 5.7: Lightning NO_x emissions resulting from inversions where IONS-06 observations are assimilated into the GEOS-Chem adjoint model. A priori emissions are from (a) the OTD-LIS scaled and (c) the Price and Rind parameterizations in GEOS-Chem, and are adjusted with linear scale factors to produce the a posteriori emissions ((b) and (d), respectively).

In the inversion with the OTD-LIS a priori, lightning emissions are scaled strongly in the southwestern U.S. and along the Gulf Coast. There is also a widespread reduction in emissions in the southeastern U.S. The local maxima in emissions over the Sierra Nevada, Florida, and the Carolinas are retained in the a posteriori emissions.

The Price and Rind a priori distribution was determined to have a low bias based on upper tropospheric NO_x measurements during the ICARTT campaign [*Hudman et al.*, 2007]. A factor of four increase was suggested at midlatitudes to correct the NO_x deficiency. The inversion result here, based on ozonesonde observations, does not approach a factor of four, but does indicate that the Price and Rind emissions distribution underestimates lightning emissions across the southern U.S.

The impact of assimilating the ozonesonde data should be readily apparent in the vertical model profiles at the observation sites. Figure 5.8 shows the correction in the residuals (model − observations) relative to the IONS-06 observations at select sites for the inversion with the OTD-LIS a priori. For the inversion with the OTD-LIS a priori, the correction in the free troposphere is substantial at these two sites; however, the profiles from the simulation using the Price and Rind distribution without any inversion matches the observations best.

The inversion results are also compared to independent observations that were not incorporated into the data assimilation system. Flights from the MOZAIC program provide ascent or descent profiles at five different sites during August 2006, and the ozone measured during these profiles is compared to the results of the inversion with the OTD-LIS a priori distribution in Figure 5.9. The inversion does produce a modest improvement at Atlanta, Dallas, and Philadelphia. At the Portland site in the northwestern U.S., changes in the lightning emissions are very small, so the priori and posteriori profiles overlap.

Table 5.3 summarizes bias statistics for ozone profiles resulting the two inversions relative to both sets of ozone observations (IONS-06 and MOZAIC). It also shows the reduced chi-squared value (χ^2/n) for the simulation, which is a measure of how well the model–observation differences are characterized by the assumed observation error. Values greater than one indicate that the 15% observation error is an underestimate.

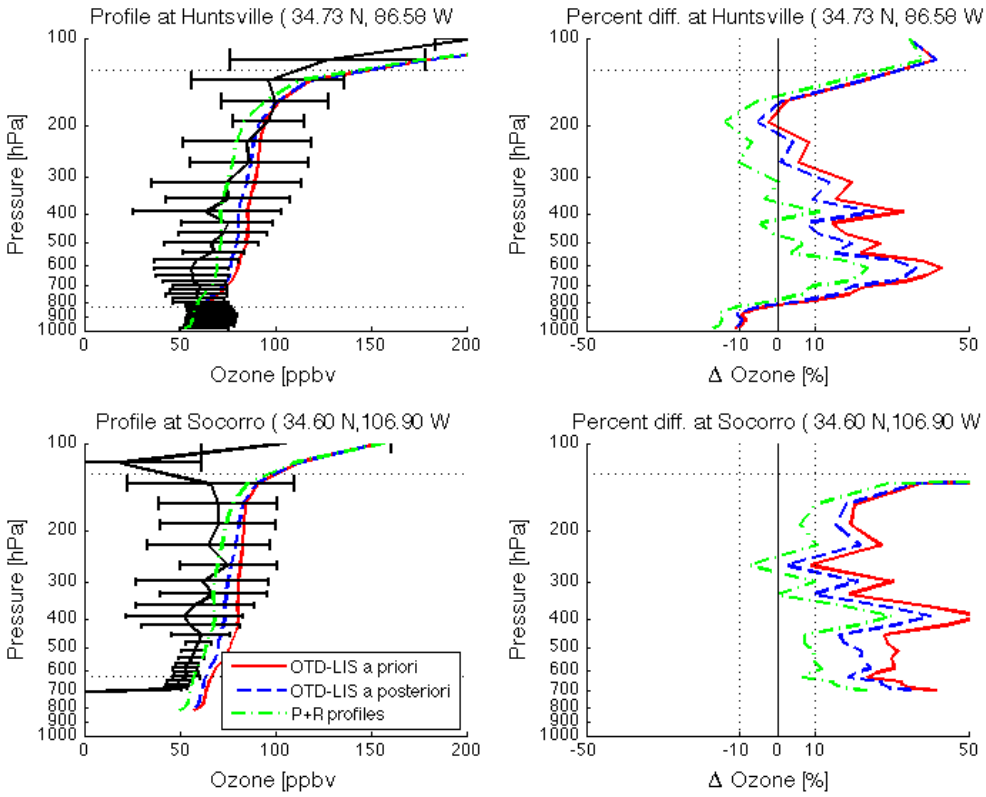

Figure 5.8: Campaign mean ozone profiles resulting from the a priori and a posteriori distributions of lightning NO_x emissions compared to IONS-06 ozonesonde observations at Huntsville, AL (top) and Socorro, NM (bottom). Horizontal dotted lines represent the mean tropopause height and PBL top. Black solid lines on the left represent the mean observed profile, and the percent difference of the model from this mean is shown on the right. At these locations, the Price and Rind a priori and a posteriori profiles overlay one another.

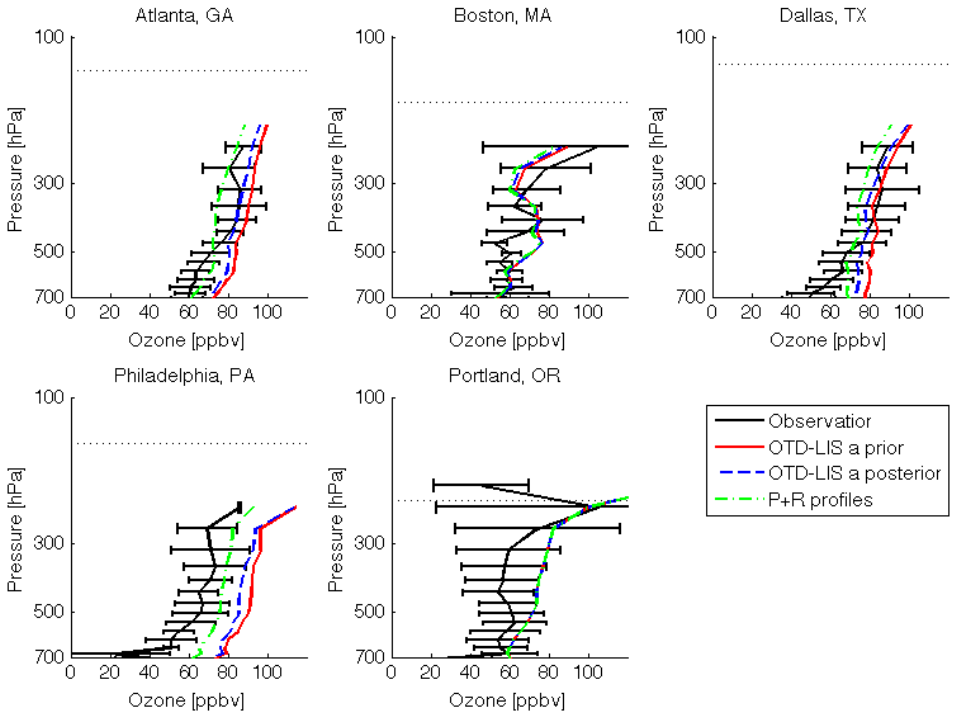

Figure 5.9: Ozone profiles resulting from the a priori and a posteriori distributions of lightning NO_x emissions compared to MOZAIC ascent and descent observations. The thin dotted horizontal lines indicate the mean tropopause at each site.

Table 5.3: Error metrics for inversions using the scaled OTD-LIS a priori distribution and the unscaled Price and Rind (P+R) a priori distribution for lightning NO_x emissions. The bias and root-mean-squared-error (RMSE) are given in units of ppbv.

		IONS		MOZAIC	
	χ^2/n	Bias	RMSE	Bias	RMSE
OTD-LIS a priori	2.98	7.5	19.9	11.4	22.2
OTD-LIS a posteriori	2.75	5.0	19.2	9.2	20.7
P+R a priori	2.45	0.1	19.8	4.2	18.5
P+R a posteriori	2.44	0.7	19.8	4.8	18.5

5.4 Future Space-Based Constraints on Lightning NO_x Emissions

Satellite data offers extensive spatial coverage and potentially high observation density compared to in situ measurements, which is promising for data assimilation. However, appropriate consideration must be given to the limitations of satellite instruments. For example, the reason that TES observations were not assimilated directly in the study described in this chapter is that the averaging kernels for this instrument are broad, and aliasing lower stratospheric ozone values into the upper troposphere could potentially bias the inversion results. With the high vertical resolution of the ozonesondes, this was not an issue; moreover, satellite instruments with high vertical resolution present an opportunity to expand this work in the future.

This section details an experiment with the GEOS-Chem adjoint model at the global scale ($4^\circ \times 5^\circ$ resolution) to determine the usefulness of satellite observations from the SOAR mission in deriving a constraint on the global lightning NO_x source. The SOAR proposal expanded on existing Canadian expertise in remote sensing through solar occultation, developed largely through the Atmospheric Chemistry Experiment (ACE) satellite mission [*Bernath et al.*, 2005]. Because the selection of orbit parameters was under consideration for SOAR, locations of occultation measurements from ACE were used as a reasonable estimate of the distribution of observations that SOAR would provide.

In the SOAR OSSE, the global full-chemistry GEOS-Chem simulation was run once to provide a distribution of ozone that was assumed to be the known true state of the atmosphere. A perturbation factor of two was applied to the model lightning NO_x emissions to initialize an adjoint inversion. Then, the ozone distribution from the true state simulation was sampled in time and space in a manner similar to observations taken from a satellite occultation instrument such as SOAR. The locations of these pseudo-observations were concentrated at low latitudes for the selected simulation period (the

first two weeks of August), as displayed in Figure 5.10. A 10% error was attributed to the pseudo-observations, which were assumed to extend from the tropopause down to 8 km altitude, below which clouds would obstruct the measurement. This altitude cut-off at 8 km is idealized, especially for tropical cases where clouds are prevalent at higher altitudes, but testing with different cut-off altitudes showed little variation in the inversion results, presumably in part because the vertical lightning emissions profile was taken as a strong constraint. For the time period under consideration, the horizontal extent of the occultation observations was small compared to the resolution of the CTM.

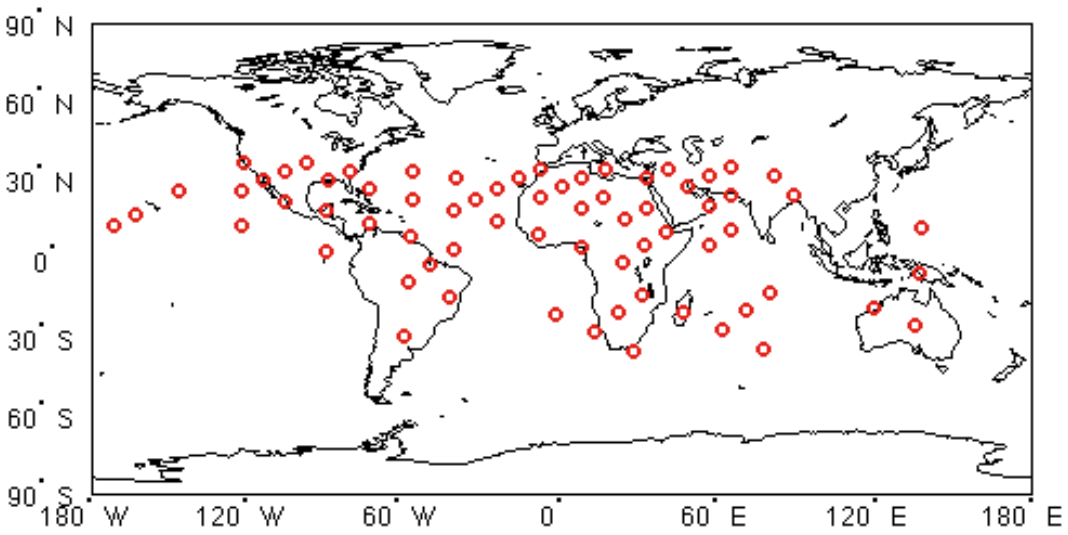

Figure 5.10: Locations of SOAR pseudo-observations from August 1–15, 2006. The occultation profiles are assumed to extend from 8 km to the tropopause.

Ozone concentrations from the pseudo-observations were used to force the adjoint model, which was configured to optimize lightning emissions as control parameters. Lightning emissions were assigned a 100% error in this inversion. In a perfect experiment, the OSSE would correct for the factor of two perturbation and recover the emissions that were used to simulate the true state. The ratio of the true state emissions to the constrained

emissions shown in Figure 5.11 is close to unity over equatorial Africa, South America, and East Asia. This indicates that information from the pseudo-observations constrains the lightning emissions well in these regions. The global total lightning emissions in the true state was 0.92 Tg N, and after starting from a factor of two higher (1.84 Tg N), the emissions in the inversion recovered to 1.65 Tg N. Emissions over Africa recovered from 0.35 Tg N to 0.24 Tg N (where the true emissions were 0.18 Tg N).

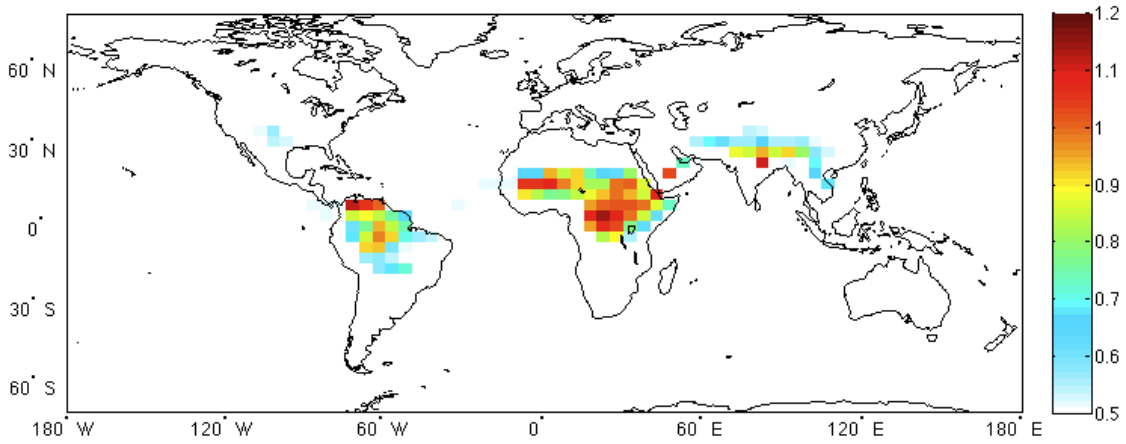

Figure 5.11: Ratio of true to constrained lightning NO_x emissions for the OSSE using SOAR pseudo-observations.

This OSSE shows the potential for occultation measurements of ozone from the SOAR mission to be used in a data assimilation context to constrain the global lightning NO_x source. Using only two weeks of pseudo-observations, an adjoint inversion is able to offer some constraint on the global source and produce a reasonable estimate of the source over the tropical continents. Furthermore, this study establishes the general usefulness of global-scale ozone measurements in optimization of NO_x emissions with an adjoint method.

5.5 Conclusions

The main result of this study is the constraint on continental scale lightning NO_x emissions obtained by adjoint inversions using ozone measurements in the free troposphere from the IONS-06 strategic ozonesonde network in August 2006. The inversion results indicate that the Price and Rind parameterization as implemented in GEOS-Chem produces an ozone field in better agreement with the ozone observations than the distribution rescaled to the OTD-LIS climatology. However, the lightning distribution that produces the optimum fit to these ozone measurements is likely between the a posteriori estimates for the two inversions starting from these different parameterizations, with a total at the continental scale between 0.076 and 0.204 Tg N. The broad range of this estimate indicates the critical need for better constraints on estimates of this source.

A study based on aircraft measurements of NO_x in the upper troposphere in August 2006 [*Hudman et al.*, 2007] concluded that a four-fold increase in GEOS-Chem lightning emissions (using the Price and Rind parameterization) at midlatitudes would resolve the low model bias relative to the NO_x measurements. However, later work suggests that chemical processing of NO_x in the upper troposphere in global CTMs happens too rapidly [*Henderson et al.*, 2011, 2012], leading to underpredictions in NO_x of at least 30%. The inversion results here do not support a four-fold increase over the Price and Rind parameterization over North America. Likewise, simulations that incorporate this factor of four increase in lightning emissions tend to overestimate ozone abundances in the free troposphere, as can be seen in Figure 5.2.

This analysis does not appear to recommend one of the lightning emissions a priori distributions examined here over the other. Rescaling the Price and Rind scheme to match a flash rate climatology does improve the ozone simulation on the global scale over the unconstrained Price and Rind parameterization [*Murray et al.*, 2012]; however, the yield of NO_x per flash applied in the GEOS-Chem model still differs in the tropics and extratropics [*Hudman et al.*, 2007], with a somewhat arbitrary cut-off latitude [*Zhang*

et al., 2013]. It is possible that the climatological flash rates do not predict well the distribution of flashes in a given year; indeed, when a high-density network of lightning flash observations over North America is used to scale emissions in place of the satellite climatology [*Zhang et al.*, 2013], the rescaled emissions appear to better match the a posteriori distribution calculated here.

A number of factors influence the ability of the inversion analyses here to reduce the range of uncertainty on the lightning source. One is whether the IONS-06 observations provide enough information to produce a constraint on the lightning distribution at all. After filtering for stratospheric influence and outliers, 10,434 model grid cells ($\sim 85\%$) remained that contained observations over the course of the full month. The number of variables being optimized was one for every horizontal grid cell ($89 \times 91 = 8,099$). This gives a good indication of why the 10-day OSSE did not produce as good a result as the 30-day OSSE. Even though ten days is sufficient to allow for transport, the reduced number of observations limits the efficacy of the observations in constraining the spatial structure at high resolution.

Another consideration is that the a priori distribution in each case was taken to be correct in the locations without lightning emissions - that is, the adjoint inversion had no ability to add emissions in a grid cell where there were none before. This is apparent in Figure 5.7 from the differences along the Gulf Coast. The Price and Rind a priori distribution places far fewer emissions over water than the OTD-LIS distribution, so the adjoint inversion in that case attempts to correct the lack of emissions over water by enhancing nearby coastal emissions.

Finally, the vertical distribution of lightning NO_x emissions within each column was assumed to be correct, in part to reduce the number of variables to constrain. A full three-dimensional inversion of the lightning emission distribution would require more observations, although the high vertical resolution of the ozonesonde network would present a useful complement to satellite data in such an inversion. One promising development

is the recent availability of tropospheric ozone retrievals from the combined spectra from TES and OMI. *Fu et al.* [2013] showed that these new retrievals provide greater constraints on the vertical distribution of ozone than retrievals from either TES or OMI alone. These data would better discriminate between ozone in the lower and upper troposphere and might, therefore, better enable the inversion to optimize the three-dimensional lightning NO_x source. Use of these data will be a focus of future work.

Chapter 6

Conclusions and Future Directions

This work addressed a number of processes affecting the distribution of ozone, a greenhouse gas and air quality concern, at middle and high northern latitudes. In a review of satellite remote sensing of surface air quality, *Martin* [2008] identified a number of specific tasks for improving models for their synergistic use with satellite instruments for air quality studies. Among them are better constraints on the free troposphere (e.g., lightning emissions), higher resolution, and development of data assimilation and adjoint methods. This work has showed the usefulness of a high-resolution adjoint model in several applications, including linking the high-latitude ozone distribution to midlatitude lightning NO_x emissions, and attempting to constrain lightning emissions at a continental scale. The same adjoint method was also extended to analyze discrepancies in surface ozone over North America, and the effects of chemistry and precursor emissions upon them.

Quantifying the ozone and total reactive nitrogen budgets in the Arctic throughout the year is important to understand both air quality and climate impacts of increases in pollution from midlatitude sources and from potential high-latitude developments. This study developed a simulation that reproduces various surface and free tropospheric

observations that establishes it as an appropriate tool for studying transport and chemical pathways for ozone reaching the Arctic troposphere.

Midlatitude sources impact the ozone abundance at Arctic sites with fractional contributions up to 30% in some seasons. The contribution from midlatitudes peaks in spring and fall, and nearby sources have a relatively larger impact on individual sites (e.g., Europe on Ny-Ålesund in summer). Local production within the Arctic region dominates the budget in the summer, producing up to 50% of the ozone abundance.

Adjoint sensitivity studies provide a large amount of detailed information about the sources that impact a particular receptor site. In the case of ozone above Alert, sensitivities are largest to anthropogenic surface NO_x emissions in May and have large sensitivities to anthropogenic, biomass burning, and lightning emissions in July. In July, the sensitivity of middle tropospheric ozone to midlatitude lightning NO_x emissions exceeds even that of midlatitude anthropogenic emissions. Southern latitudes are more likely to affect ozone abundances at Alert in spring than in summer.

A sensitivity study to isolate the influence of PAN decomposition finds that when the Arctic lower troposphere becomes isolated from external sources in the summer, subsidence and decomposition of PAN provides a local source of NO_x and ozone production. PAN in the model is produced both in the Arctic free troposphere and in midlatitude source regions. PAN constitutes a significant portion of total reactive nitrogen in the Arctic, although there is evidence that the overall partitioning of total reactive nitrogen in GEOS-Chem is flawed [*Alvarado et al.*, 2010]. Further study of this partitioning is encouraged, which could draw on long-term measurements of PAN at the Alert site as well as a number of high-latitude aircraft campaigns.

Assimilation of TES observations of ozone and CO into the midlatitudes in the model produces a correction that is in many ways similar to a redistribution of lightning NO_x emissions in the model [*Parrington et al.*, 2008]. The assimilation increases background free tropospheric ozone abundances throughout midlatitudes, providing an improved rep-

resentation of ozone transported to the Arctic from lower latitudes. Both the assimilation and the improved distribution of lightning NO_x emissions effect a correction in free tropospheric ozone concentrations relative to ozonesondes, reducing the mean bias in the summer at Eureka from -18% to -6% and at Ny-Ålesund from -18% to -7%.

While the simulation of ozone in the free troposphere improves after assimilating TES profiles, the assimilation exacerbates an existing bias at the surface over North America. This surface ozone bias is common to many models [*Reidmiller et al.*, 2009]. Inversion results in this work to account for this bias with changes to precursor emissions show that unreasonable adjustments to the emissions are needed to correct the bias. Anthropogenic NO_x emissions, for instance, must be reduced from 0.43 Tg N/month to 0.25 Tg N/month, with reductions over urban regions in the eastern U.S. that produces column abundances of NO_2 that do not match observed NO_2 distributions.

A separate inversion that uses surface ozone observations to optimize reaction rates suggests that deposition rates in the northeastern U.S. can be adjusted by a factor of 2–3 to mitigate the ozone bias. The inversion results are sensitive to the planetary boundary layer mixing scheme, which is potentially biased at night [*Lin and McElroy*, 2010]. Subtracting the bias due to a change in the mixing scheme improves the inversion agreement with observations, but improvements to the adjoint dry deposition and mixing modules could directly address these effects.

A significant limitation in the analyses presented here is that the covariance matrices used in the 4D-Var inversions and sensitivity studies were assumed to be diagonal. That is, the observations were treated as independent from one another, and any parameters included in the control vector were also treated as being uncorrelated. At the time of writing, the GEOS-Chem adjoint model was unable to represent non-diagonal covariances. In general, this is a simplification, as both observations and control parameters may be correlated one to another through time and space. Updates to the adjoint model are in progress to represent the full non-diagonal covariance, enabling the study of effects

of these correlations. This would be helpful, for example, in specifying spatial correlations so that the inversion analyses can optimize the deposition velocities according to vegetation type.

Another difficulty is the lack of widespread data to directly validate the inferred deposition fluxes; instead concentration measurements are combined with a model-calculated deposition velocity to obtain a flux [*Clarke et al.*, 1997]. Measurements of ozone deposition flux with eddy covariance techniques are sparse, and occur at the canopy scale ($\sim$ 10 m), but even the high-resolution model used here has a lowest level $\sim$ 100 m thick and a horizontal resolution of tens of kilometres. Improving the link between canopy-scale observations and fluxes calculated at model resolution is an avenue for future research.

Combining air quality constraints from multiple observational platforms in a common modelling framework provides a promising avenue for future work. Integrating space-based measurements of NO_2, CH_2O, ozone, and CO into the 4D-Var inversions described here would greatly improve data density, and so produce a more reliable a posteriori simulation of surface ozone [*Miyazaki et al.*, 2012]. Observations of additional species also give more constraints on the ozone chemistry, for instance CH_2O can give information about isoprene emissions [*Millet et al.*, 2008]. This would enable observation-based assessments of the impacts of ozone pollution, such as quantifying ozone-induced crop loss, the study of which has been limited by models' inability to reproduce ozone exposure metrics.

Another promising future data source for air quality studies is the upcoming availability of earth observation from geostationary orbit. Satellite missions such as the Tropospheric Emissions: Monitoring of Pollution (TEMPO) mission over North America, the European Sentinel-4 mission, the Geostationary Environment Monitoring Spectrometer over Asia, and the Polar Communication and Weather (PCW) mission in the Arctic will provide a constellation of geostationary observations of atmospheric composition similar to the current instrumental array, except with 24-hour coverage. For example, the

continuous, hourly daytime observations from TEMPO of near-surface ozone over North America would provide significantly greater constraints on ozone deposition than that available from the existing surface observation network. Observations over the full day will allow the capture of fast variations in emissions and chemistry, and enhance the monitoring of air quality events.

The distribution of lightning NO_x emissions over North America is linked to ozone both at high latitudes and at the surface. A 4D-Var inversion to constrain the continental scale lightning emissions using data from a strategic ozonesonde network (IONS-06) was performed, suggesting that the continental scale emissions lie between 0.076 and 0.204 Tg N for August 2006. While the range is broad, it is an improvement on previous conclusions that implied factors of four uncertainty in this NO_x source [*Hudman et al.*, 2007].

A key improvement to this work would be an extension to optimize the three-dimensional distribution of the NO_x source. The ozonesonde network used here does not contain sufficient information to accomplish this, but promising new satellite products could be used in a similar inversion framework in the future. One promising satellite product for future studies is the TES-OMI combined retrieval, which has better vertical resolution, and in particular, greater sensitivity to near-surface ozone than products retrieved from either instrument individually [*Fu et al.*, 2013]. These could provide valuable new information for inverse modelling of the lightning NO_x source and the surface deposition fluxes of ozone.

Bibliography

Akagi, S. K., R. J. Yokelson, C. Wiedinmyer, M. J. Alvarado, J. S. Reid, T. Karl, J. D. Crounse, and P. O. Wennberg (2011), Emission factors for open and domestic biomass burning for use in atmospheric models, *Atmos. Chem. Phys.*, *11*, 4039–4072.

Allen, D., K. Pickering, B. Duncan, and M. Damon (2010), Impact of lightning NO emissions on North American photochemistry as determined using the Global Modeling Initiative (GMI) model, *J. Geophys. Res.*, *115*, D22301, doi:10.1029/2010JD014062.

Allen, D. J., K. E. Pickering, R. W. Pinder, B. H. Henderson, K. W. Appel, and A. Prados (2012), Impact of lightning-NO on eastern United States photochemistry during the summer of 2006 as determined using the CMAQ model, *Atmos. Chem. Phys.*, *12*, 1737–1758.

Alvarado, M. J., et al. (2010), Nitrogen oxides and PAN in plumes from boreal fires during ARCTAS-B and their impact on ozone: an integrated analysis of aircraft and satellite observations, *Atmos. Chem. Phys.*, *10*, 9739–9760.

Apel, E. C., et al. (2012), Impact of the deep convection of isoprene and other reactive trace species on radicals and ozone in the upper troposphere, *Atmos. Chem. Phys.*, *12*, 1135–1150.

Ashmore, M. R. (2005), Assessing the future global impacts of ozone on vegetation, *Plant, Cell & Environment*, *28 (8)*, 949–964.

Atlas, E. L., B. A. Ridley, and C. A. Cantrell (2003), The Tropospheric Ozone Production about the Spring Equinox (TOPSE) Experiment: Introduction, *J. Geophys. Res.*, *108*(D4), doi:10.1029/2002JD003172.

Barthe, C., W. Deierling, and M. C. Barth (2010), Estimation of total lightning from various storm parameters: A cloud-resolving model study, *J. Geophys. Res.*, *115*, D24202, doi:10.1029/2010JD014405.

Baumgardner, R. E., Jr., T. F. Lavery, C. M. Rogers, and S. S. Isil (2002), Estimates of the atmospheric deposition of sulfur and nitrogen species: Clean Air Status and Trends Network, 1990-2000, *Environ. Sci. Technol.*, *36*, 2614–2629.

Beer, R., T. Glavich, and D. Rider (2001), Tropospheric Emission Spectrometer for the Earth Observing System's Aura satellite, *Appl. Opt.*, *40*, 2356–2367.

Beine, H. J., and T. Krojnes (2000), The seasonal cycle of peroxyacetyl nitrate (PAN) in the European Arctic, *Atmos. Environ.*, *34*, 933–940.

Bell, M. L., R. Goldberg, C. Hogrefe, P. L. Kinney, K. Knowlton, B. Lynn, et al. (2007), Climate change, ambient ozone, and health in 50 US cities, *Clim. Change*, *82*, 61–76.

Benkovitz, C. M., M. T. Scholtz, J. Pacyna, L. Tarrasón, J. Dignon, E. C. Voldner, P. A. Spiro, J. A. Logan, and T. E. Graedel (1996), Global gridded inventories of anthropogenic emissions of sulfur and nitrogen, *J. Geophys. Res.*, *101*(D22), 29,239–29,254.

Bernath, P. F., et al. (2005), Atmospheric Chemistry Experiment (ACE): Mission overview, *Geophys. Res. Lett.*, *32*, L15S01, doi:10.1029/2005GL022386.

Bey, I., et al. (2001), Global modeling of tropospheric chemistry with assimilated meteorology: Model description and evaluation, *J. Geophys. Res.*, *106*, 23,073–23,096.

Bloom, S., et al. (2005), Documentation and Validation of the Goddard Earth Observing System (GEOS) Data Assimilation System - Version 4, *Tech. rep.*, Global Modelling and Assimilation Office, Technical Report Series on Global Modeling and Data Assimilation 104606, 26.

Bloomer, B. J., K. Y. Vinnikov, and R. R. Dickerson (2010), Changes in seasonal and diurnal cycles of ozone and temperature in the eastern U.S., *Atmos. Environ.*, *44*, 2543–2551.

Boersma, K. F., D. J. Jacob, M. Trainic, Y. Rudich, I. DeSmedt, R. Dirksen, and H. J. Eskes (2009), Validation of urban NO_2 concentrations and their diurnal and seasonal variations observed from the SCIAMACHY and OMI sensors using in situ surface measurements in Israeli cities, *Atmos. Chem. Phys.*, *9*, 3867–3879.

Bottenheim, J. W., L. A. Barrie, and E. Atlas (1993), The Partitioning of Nitrogen Oxides in the Lower Arctic Troposphere During Spring 1988, *J. Atmos. Sci.*, *17*, 15–27.

Bottenheim, J. W., J. D. Fuentes, D. W. Tarasick, and K. G. Anlauf (2002), Ozone in the Arctic lower troposphere during winter and spring 2000 (ALERT2000), *Atmos. Environ.*, *36*, 2535–2544.

Bottenheim, J. W., S. Netcheva, S. Morin, and S. V. Nghiem (2009), Ozone in the boundary layer air over the Arctic Ocean: measurements during the TARA transpolar drift 2006-2008, *Atmos. Chem. Phys.*, *9*, 4545–4557.

Bourqui, M. S. (2006), Stratosphere-troposphere exchange from the Lagrangian perspective: a case study and method sensitivities, *Atmos. Chem. Phys.*, *6*, 2651–2670.

Bourqui, M. S., and P.-Y. Trépanier (2010), Descent of deep stratospheric intrusions during the IONS August 2006 campaign, *J. Geophys. Res.*, *115*, D18301, doi:10.1029/2009JD013183.

Bourqui, M. S., et al. (2012), A new global real-time Lagrangian diagnostic system for stratosphere-troposphere exchange: evaluation during a balloon sonde campaign in eastern Canada, *Atmos. Chem. Phys.*, *12*, 2661–2679.

Bowman, K. W., J. Worden, T. Steck, H. M. Worden, S. Clough, and C. Rodgers (2002), Capturing time and vertical variability of tropospheric ozone: A study using TES nadir retrievals, *J. Geophys. Res.*, *107*(D23), 4723–4734, doi:10.1029/2002JD002150.

Bowman, K. W., et al. (2006), Tropospheric Emission Spectrometer: Retrieval Method and Error Analysis, *IEEE Trans. Geosci. Remote Sens.*, *44 (5)*, 1297–1307.

Boxe, C., et al. (2010), Validation of northern latitude Tropospheric Emission Spectrometer stare ozone profiles with ARC-IONS sondes during ARCTAS: sensitivity, bias and error analysis, *Atmos. Chem. Phys.*, *10*, 9901–9914.

Brook, J. R., R. T. Burnett, T. F. Dann, S. Cakmak, M. S. Goldberg, X. Fan, and A. J. Wheeler (2007), Further interpretation of the acute effect of nitrogen dioxide observed in Canadian time-series studies, *Journal of Exposure Science and Environmental Epidemiology*, *17*, S36–S44.

Browne, E. C., et al. (2011), Global and regional effects of the photochemistry of $CH_3O_2NO_2$: evidence from ARCTAS, *Atmos. Chem. Phys.*, *11*, 4209–4219.

Brühl, C., U. Pöschl, P. J. Crutzen, and B. Steil (2000), Acetone and PAN in the upper troposphere: impact on ozone production from aircraft emissions, *Atmos. Environ.*, *34*, 3931–3938.

Byrd, R. H., P. Lu, J. Nocedal, and C. Zhu (1995), A limited memory algorithm for bound constrained optimization, *Scientific Computing*, *16*, 1190–1208.

Cantrell, C. A., et al. (2003), Steady state free radical budgets and ozone photochemistry during TOPSE, *J. Geophys. Res.*, *108*(D4), 8361–8383, doi:10.1029/2002JD002198.

Chameides, W. L., R. D. Saylor, and E. B. Cowling (1997), Ozone pollution in the rural United States and the new NAAQS, *Science*, *276*, 916.

Chan, E. (2009), Regional ground-level ozone trends in the context of meteorological influences across Canada and the eastern United States from 1997 to 2006, *J. Geophys. Res.*, *114*, D05301, doi:10.1029/2008JD010090.

Chen, D., Y. X. Wang, M. B. McElroy, K. He, R. M. Yantosca, and P. Le Sager (2009), Regional CO pollution in China simulated by the high-resolution nested-grid GEOS-Chem model, *Atmos. Chem. Phys.*, *9*, 3825–3839.

Christian, H. J., et al. (2003), Global frequency and distribution of lightning as observed from space by the Optical Transient Detector, *J. Geophys. Res.*, *108*(D1), 4005–4020, doi:10.1029/2002JD002347.

Clarke, J. F., E. S. Edgerton, and B. E. Martin (1997), Dry deposition calculations for the Clean Air Status and Trends Network, *Atmos. Environ.*, *31*(21), 3667–3678.

Coman, A., et al. (2012), Assimilation of IASI partial tropospheric columns with an Ensemble Kalman Filter over Europe, *Atmos. Chem. Phys.*, *12*, 2513–2532.

Cooper, O. R., et al. (2007), Evidence for a recurring eastern North American upper tropospheric ozone maximum during summer, *J. Geophys. Res.*, *112*, D23306, doi: 10.1029/2007JD008910.

Cooper, O. R., et al. (2009), Summertime buildup and decay of lightning NO_x and aged thunderstorm outflow above North America, *J. Geophys. Res.*, *114*, D01101, doi: 10.1029/2008JD010293.

Corbett, J. J., D. A. Lack, J. J. Winebrake, S. Harder, J. A. Silberman, and M. Gold (2010), Arctic shipping emissions inventories and future scenarios, *Atmos. Chem. Phys.*, *10*, 9689–9704.

Crutzen, P. J. (1979), The role of NO and NO_2 in the chemistry of the troposphere and stratosphere, *Ann. Rev. Earth Planet. Sci.*, *7*, 443–472.

Cui, J., S. Pandey Deolal, M. Sprenger, S. Henne, J. Staehelin, M. Steinbacher, and P. Nédélec (2011), Free tropospheric ozone changes over Europe as observed at Jungfraujoch (1990-2008): An analysis based on backward trajectories, *J. Geophys. Res.*, *116*, D10304, doi:10.1029/2010JD015154.

Curren, K., and T. Dann (2004), Air Quality in Canada: 2001 Summary and 1990-2001 Trend Analyses, *Tech. Rep. EPS 7/AP/36*, Environment Canada.

Daescu, D. N., A. Sandu, and G. R. Carmichael (2003), Direct and Adjoint Sensitivity Analysis of Chemical Kinetic Systems with KPP: II - Numerical Validation and Applications, *Atmos. Environ.*, *37*, 5097–5114.

Day, D. A., P. J. Wooldridge, M. B. Dillon, J. A. Thornton, and R. C. Cohen (2002), A thermal dissociation laser-induced fluorescence instrument for in situ detection of NO_2, peroxy nitrates, alkyl nitrates, and HNO_3, *J. Geophys. Res.*, *107*(D6), 4046–4060, doi:10.1029/2001JD000779.

DeCaria, A. J., K. E. Pickering, G. L. Stenchikov, and L. E. Ott (2005), Lightning-generated NO_x and its impact on tropospheric ozone production: A three-dimensional modeling study of a Stratosphere-Troposphere Experiment: Radiation, Aerosols, and Ozone (STERAO-A) thunderstorm, *J. Geophys. Res.*, *110*, D14303, doi:10.1029/2004JD005556.

Driscoll, C. T., et al. (2001), Acidic deposition in the northeastern United States: sources and inputs, ecosystem effects, and management strategies, *Bioscience*, *51 (3)*, 180–198.

Duncan, B. N., and I. Bey (2004), A modeling study of the export pathways of pollution from Europe: Seasonal and interannual variations (1987-1997), *J. Geophys. Res.*, *109*, D08301, doi:10.1029/2003JD004079.

Duncan, B. N., R. V. Martin, A. C. Staudt, R. Yevich, and J. A. Logan (2003), Interannual and seasonal variability of biomass burning emissions constrained by satellite observations, *J. Geophys. Res.*, *108*, 4100–4127.

Dunlea, E. J., et al. (2007), Evaluation of nitrogen dioxide chemiluminescence monitors in a polluted urban environment, *Atmos. Chem. Phys.*, *7*, 2691–2704.

Eckhardt, S., et al. (2003), The North Atlantic Oscillation controls air pollution transport to the Arctic, *Atmos. Chem. Phys.*, *3*, 1769–1778.

Elbern, H., H. Schmidt, O. Talagrand, and A. Ebel (2000), 4D-variational data assimilation with an adjoint air quality model for emission analysis, *Environ. Modell. Software*, *15*, 539–548.

Environment Canada, Alfred Wegener Institute, Japan Meteorological Agency, Meteorological Department of Iran, MeteoSwiss, NOAA Climate Monitoring and Diagnostics Laboratory, University of Alabama at Huntsville, and NASA Wallops Island Flight Facility (2009), World Ozone and Ultraviolet Radiation Data Centre (WOUDC) [Data], retrieved December 10, 2009, from http://www.woudc.org/.

Evans, M. J., and D. J. Jacob (2005), Impact of new laboratory studies of N_2O_5 hydrolysis on global model budgets of tropospheric nitrogen oxides, ozone and OH, *Geophys. Res. Lett.*, *32*, L09813, doi:10.1029/2005GL022469.

Fan, J., and R. Zhang (2004), Atmospheric Oxidation Mechanism of Isoprene, *Environ. Chem.*, *1*, 140–149.

Fan, S.-M., and D. J. Jacob (1992), Surface ozone depletion in Arctic spring sustained by bromine reactions on aerosols, *Nature*, *359*, 522–524.

Fan, S.-M., et al. (1994), Origin of tropospheric NO_x over subarctic eastern Canada in summer, *J. Geophys. Res.*, *99*(D8), 16,867–16,877.

Farmer, D. K., P. J. Wooldridge, and R. C. Cohen (2006), Application of thermal-dissociation laser induced fluoresence (TD-LIF) to measurements of HNO_3, $\sum$alkyl nitrates, $\sum$peroxy nitrates, and NO_2 fluxes using eddy covariance, *Atmos. Chem. Phys.*, *6*, 3471–3486.

Finkelstein, P. L., T. G. Ellestad, J. F. Clarke, T. P. Meyers, D. B. Schwede, E. O. Hebert, and J. A. Neal (2000), Ozone and sulfur dioxide dry deposition to forests: Observations and model evaluation, *J. Geophys. Res.*, *105*(D12), 15,365–15,377.

Fiore, A. M., D. J. Jacob, I. Bey, R. M. Yantosca, B. D. Field, A. C. Fusco, and J. G. Wilkinson (2002), Background ozone over the United States in summer: Origin, trend, and contribution to pollution episodes, *J. Geophys. Res.*, *107*(D15), 1–25, doi:10.1029/2001JD000982.

Fiore, A. M., D. J. Jacob, R. Mathur, and R. V. Martin (2003), Application of empirical orthogonal functions to evaluate ozone simulations with regional and global models, *J. Geophys. Res.*, *108*(D14), 4431–4439.

Fiore, A. M., L. W. Horowitz, D. W. Purves, I. H. Levy, M. J. Evans, Y. Wang, Q. Li, and R. M. Yantosca (2005), Evaluating the contribution of changes in isoprene emissions to surface ozone trends over the eastern United States, *J. Geophys. Res.*, *110*, D12303, doi:10.1029/2004JD005485.

Fiore, A. M., et al. (2009), Multimodel estimates of intercontinental source-receptor relationships for ozone pollution, *J. Geophys. Res.*, *114*, D04301, doi:10.1029/2008JD010816.

Fischer, E. V., D. J. Jacob, D. B. Millet, R. M. Yantosca, and J. Mao (2012), The role of the ocean in the global atmospheric budget of acetone, *Geophys. Res. Lett.*, *39*, L01807, doi:10.1029/2011GL050086.

Fisher, J. A., et al. (2010), Source attribution and interannual variability of Arctic pollution in spring constrained by aircraft (ARCTAS, ARCPAC) and satellite (AIRS) observations of carbon monoxide, *Atmos. Chem. Phys.*, *10*, 977–996.

Folberth, G. A., D. A. Hauglustaine, P. Ciais, and J. Lathière (2006), Interactive chemistry in the Laboratoire de Météorologie Dynamique general circulation model: model description and impact of biogenic hydrocarbons on tropospheric chemistry, *Atmos. Chem. Phys.*, *6*, 2273–2319.

Folkins, I., P. Bernath, C. Boone, L. J. Donner, A. Eldering, G. Lesins, R. V. Martin, B.-M. Sinnhuber, and K. Walker (2006), Testing convective paramaterizations with tropical measurements of HNO_3, CO, H_2O, and O_3: Implications for the water vapor budget, *J. Geophys. Res.*, *111*, D23304, doi:10.1029/2006JD007325.

Fu, D., J. R. Worden, X. Liu, S. S. Kulawik, K. W. Bowman, and V. Natraj (2013), Characterization of ozone profiles derived from Aura TES and OMI radiances, *Atmos. Chem. Phys.*, *13*, 3445–3462.

Fusco, A. C., and J. A. Logan (2003), Analysis of 1970-1995 trends in tropospheric ozone at Northern Hemisphere midlatitudes with the GEOS-Chem model, *J. Geophys. Res.*, *108*(D15), 4449–4473, doi:10.1029/2002JD002742.

Giering, R., and T. Kaminski (1998), Recipes for Adjoint code Construction, *ACM Trans. Math. Softw.*, *24*, 437.

Giglio, L., G. R. van der Werf, J. T. Randerson, G. J. Collatz, and P. S. Kasibhatla (2006), Global estimation of burned area using MODIS active fire observations, *Atmos. Chem. Phys.*, *6*, 957–974.

Gou, T., and A. Sandu (2011), Continuous versus discrete advection adjoints in chemical data assimilation with CMAQ, *Atmos. Environ.*, *45 (28)*, 4868–4881.

Guenther, A., et al. (1995), A global model of natural volatile organic compound emissions, *J. Geophys. Res.*, *100*(D5), 8873–8892.

Guenther, A., T. Karl, P. Harley, C. Wiedinmyer, P. I. Palmer, and C. Geron (2006), Estimates of global terrestrial isoprene emissions using MEGAN (Model of Emissions of Gases and Aerosols from Nature), *Atmos. Chem. Phys.*, *6*, 3181–3210.

Hack, J. J. (1994), Parameterization of moist convection in the National Center for Atmospheric Research Community Climate Model (CCM2), *J. Geophys. Res.*, *99*, 5551–5568.

Hakami, A., D. K. Henze, J. H. Seinfeld, T. Chai, Y. Tang, G. R. Carmichael, and A. Sandu (2005), Adjoint inverse modeling of black carbon during the Asian Pacific Regional Aerosol Characterization Experiment, *J. Geophys. Res.*, *110*, D14301, doi: 10.1029/2004JD005671.

Hakami, A., J. H. Seinfeld, T. Chai, Y. Tang, G. R. Carmichael, and A. Sandu (2006), Adjoint Sensitivity Analysis of Ozone Nonattainment over the Continental United States, *Environ. Sci. Technol.*, *40*, 3855–3864.

Hakami, A., D. K. Henze, J. H. Seinfeld, K. Singh, A. Sandu, S. Kim, D. Byun, and Q. Li (2007), The adjoint of CMAQ, *Environ. Sci. Technol.*, *41 (22)*, 7807–7818.

Hauglustaine, D. A., J. Lathière, S. Szopa, and G. A. Folberth (2005), Future tropospheric ozone simulated with a climate-chemistry-biosphere model, *Geophys. Res. Lett.*, *32*, L24807, doi:10.1029/2005GL024031.

Hauglustaine, D. A., et al. (2004), Interactive chemistry in the laboratoire de meteorologie dynamique general circulation model: description and background tropospheric chemistry, *J. Geophys. Res.*, *109*, D04314, doi:10.1029/2003JD003957.

Hegglin, M. I., et al. (2010), Multimodel assessment of the upper troposphere and lower stratosphere: Extratropics, *J. Geophys. Res.*, *115*, D00M09, doi:10.1029/2010JD013884.

Helmig, D., S. J. Oltmans, D. Carlson, J.-F. Lamarque, A. Jones, C. Labuschagne, K. Anlauf, and K. Hayden (2007), A review of surface ozone in the polar regions, *Atmos. Environ.*, *41*(24), 5138–5161, doi:10.1016/j.atmosenv.2006.09.053.

Henderson, B. H., et al. (2011), Evaulation of simulated photochemical partitioning of oxidized nitrogen in the upper troposphere, *Atmos. Chem. Phys.*, *11*, 275–291.

Henderson, B. H., R. W. Pinder, J. Crooks, R. C. Cohen, A. G. Carlton, H. O. T. Pye, and W. Vizuete (2012), Combining Bayesian methods and aircraft observations to constrain the HO+NO_2 reaction rates, *Atmos. Chem. Phys.*, *12*, 653–667.

Henze, D. K., A. Hakami, and J. H. Seinfeld (2007), Development of the adjoint of GEOS-Chem, *Atmos. Chem. Phys.*, *7*, 2413–2433.

Henze, D. K., J. H. Seinfeld, and D. T. Shindell (2009), Inverse modeling and mapping US air quality influences of inorganic $PM_{2.5}$ precursor emissions using the adjoint of GEOS-Chem, *Atmos. Chem. Phys.*, *9*, 5877–5903.

Hess, P. G., and R. Zbinden (2013), Stratospheric impact on tropospheric ozone variability and trends: 1990-2009, *Atmos. Chem. Phys.*, *13*, 649–674.

Hirdman, D., et al. (2010), Source identification of short-lived air pollutants in the Arctic using statistical analysis of measurement data and particle dispersion model output, *Atmos. Chem. Phys.*, *10*, 669–693.

Holton, J. R., P. H. Haynes, M. E. McIntyre, A. R. Douglass, R. B. Rood, and L. Pfister (1995), Stratosphere-troposphere exchange, *Review of Geophysics*, *33 (4)*, 403–439.

Holtslag, A. A. M., and B. A. Boville (1993), Local Versus Nonlocal Boundary-Layer Diffusion in a Global Climate Model, *J. Clim.*, *6*, 1825–1842.

Honrath, R. E., Y. Lu, M. C. Peterson, J. E. Dibb, M. A. Arsenault, N. J. Cullen, and K. Steffen (2002), Vertical fluxes of NO_x, HONO, and HNO_3 above the snowpack at Summit, Greenland, *Atmos. Environ.*, *36*, 2629–2640.

Horowitz, L. W., et al. (2003), A global simulation of tropospheric ozone and related tracers: description and evaluation of MOZART, version 2, *J. Geophys. Res.*, *108*, 4784, doi:10.1029/2002JD002853.

Hsu, J., and M. J. Prather (2009), Stratospheric variability and tropospheric ozone, *J. Geophys. Res.*, *114*, D06102, doi:10.1029/2008JD010942.

Huang, M., et al. (2010), Impacts of transported background ozone on California air quality during the ARCTAS-CARB period - a multi-scale modeling study, *Atmos. Chem. Phys.*, *10*, 6947–6968.

Hudman, R. C., et al. (2004), Ozone production in transpacific Asian pollution plumes and implications for ozone air quality in California, *J. Geophys. Res.*, *109*, D23S10, doi:10.1029/2004JD004974.

Hudman, R. C., et al. (2007), Surface and lightning sources of nitrogen oxides over the United States: magnitudes, chemical evolution, and outflow, *J. Geophys. Res.*, *112*, D12S05, doi:10.1029/2006JD007912.

Hudman, R. C., A. R. Russell, L. C. Valin, and R. C. Cohen (2010), Interannual variability in soil nitric oxide emissions over the United States as viewed from space, *Atmos. Chem. Phys.*, *10*, 9943–9952.

Hudman, R. C., N. E. Moore, A. K. Mebust, R. V. Martin, A. R. Russell, L. C. Valin, and R. C. Cohen (2012), Steps towards a mechanistic model of global soil nitric ox-

ide emissions: implementation and space-based constraints, *Atmos. Chem. Phys.*, *12*, 7779–7795.

Huntrieser, H., et al. (2008), Lightning activity in Brazilian thunderstorms during TROCCINOX: implications for NO_x production, *Atmos. Chem. Phys.*, *8*, 921–953.

Huntrieser, H., et al. (2009), NO_x production by lightning in Hector: first airborne measurements during SCOUT-O3/ACTIVE, *Atmos. Chem. Phys.*, *9*, 8377–8412.

Huntrieser, H., et al. (2011), Mesoscale convective systems observed during AMMA and their impact on the NO_x and O_3 budget over West Africa, *Atmos. Chem. Phys.*, *11*, 2503–2536.

Jacob, D. J. (1999), *Introduction to Atmospheric Chemistry*, Princeton University Press, Princeton, NJ.

Jacobson, M. Z. (2010), Short-term effects of controlling fossil-fuel soot, biofuel soot and gases, and methane on climate, Arctic ice, and air pollution health, *J. Geophys. Res.*, *115*, D14209, doi:10.1029/2010JD013795.

Jaeglé, L., et al. (2004), Satellite mapping of rain-induced nitric oxide emissions from soils, *J. Geophys. Res.*, *109*, D21310, doi:10.1029/2004JD004787.

Jaeglé, L., L. Steinberger, R. V. Martin, and K. Chance (2005), Global partitioning of NO_x sources using satellite observations: Relative roles of fossil fuel combustion, biomass burning and soil emissions, *Faraday Discussions*, *130*, 407–423.

Jerrett, M., R. T. Burnett, I. C. A. Pope, K. Ito, G. Thurston, D. Krewski, Y. Shi, E. Calle, and M. Thun (2009), Long-term ozone exposure and mortality, *N. Engl. J. Med.*, *360*, 1085–1095.

Jiang, Z. (2012), Remote sensing and inverse transport modelling of carbon monoxide, Ph.D. thesis, University of Toronto.

Jiang, Z., D. B. A. Jones, M. Kopacz, J. Liu, D. K. Henze, and C. Heald (2011), Quantifying the impact of model errors on top-down estimates of carbon monoxide emissions using satellite observations, *J. Geophys. Res.*, *116*, D15306, doi:10.1029/2010JD015282.

Jourdain, L., S. S. Kulawik, H. M. Worden, K. E. Pickering, J. Worden, and A. M. Thompson (2010), Lightning NO_x emissions over the USA constrained by TES ozone observations and the GEOS-Chem model, *Atmos. Chem. Phys.*, *10*, 107–119.

Katragkou, E., P. Zanis, I. Kioutsioukis, I. Tegoulias, D. Melas, B. C. Krüger, and E. Coppola (2011), Future climate change impacts on summer surface ozone from regional climate-air quality simulations over Europe, *J. Geophys. Res.*, *116*, D22307, doi:10.1029/2011JD015899.

Kerzenmacher, T. E., et al. (2005), Measurements of O_3, NO_2 and Temperature during the 2004 Canadian Arctic ACE Validation Campaign, *Geophys. Res. Lett.*, *32*, L16S07, doi:10.1029/2005GL023032.

Kivi, R., E. Kyrö, T. Turunen, N. R. P. Harris, P. von der Gathen, M. Rex, S. B. Andersen, and I. Wohltmann (2007), Ozonesonde observations in the Arctic during 1989-2003: Ozone variability and trends in the lower stratosphere and free troposphere, *J. Geophys. Res.*, *112*, D08306, doi:10.1029/2006JD007271.

Klonecki, A., P. Hess, L. Emmons, L. Smith, J. Orlando, and D. Blake (2003), Seasonal changes in the transport of pollutants into the Arctic troposphere - model study, *J. Geophys. Res.*, *108*(D4), 8367–8387, doi:10.1029/2002JD002199.

Koch, D., and J. Hansen (2005), Distant origins of Arctic black carbon: A Goddard Institute for Space Studies ModelE experiment, *J. Geophys. Res.*, *110*, D04204, doi: 10.1029/2004JD005296.

Komhyr, W. D. (1969), Electrochemical Concentration Cells for gas analysis, *Ann. Geophys.*, *25*, 203–210.

Konovalov, I. B., M. Beekmann, A. Richter, J. P. Burrows, and A. Hilboll (2010), Multi-annual changes of NO_x emissions in megacity regions: nonlinear trend analysis of satellite measurement based estimates, *Atmos. Chem. Phys.*, *10*, 8481–8498.

Kopacz, M., D. J. Jacob, D. K. Henze, C. L. Heald, D. G. Streets, and Q. Zhiang (2009), A comparison of analytical and adjoint Bayesian inversion methods for constraining Asian sources of CO using satellite (MOPITT) measurements of CO columns, *J. Geophys. Res.*, *114*, D04305, doi:10.1029/2007JD009264.

Kopacz, M., et al. (2010), Global estimates of CO sources with high resolution by adjoint inversion of multiple satellite datasets (MOPITT, AIRS, SCIAMACHY, TES), *Atmos. Chem. Phys.*, *10*, 855–876.

Krupa, S. V., and W. J. Manning (1988), Atmospheric ozone: Formation and effects on vegetation, *Environmental Pollution*, *50*, 101–137.

Kuhns, H., E. M. Knipping, and J. M. Vukovich (2005), Development of a United States-Mexico Emissions Inventory for the Big Bend Regional Aerosol and Visibility Observational (BRAVO) Study, *J. Air Waste Management*, *55*, 677–692.

LaFranchi, B. W., et al. (2009), Closing the peroxy acetyl nitrate budget: observations of acyl peroxy nitrates (PAN, PPN, and MPAN) during BEARPEX 2007, *Atmos. Chem. Phys.*, *9*, 7623–7641.

Lamarque, J.-F., and P. G. Hess (2003), Model analysis of the temporal and geographical origin of the CO distribution during the TOPSE campaign, *J. Geophys. Res.*, *108*(D4), 8354–8365, doi:10.1029/2002JD002077.

Lamarque, J.-F., B. V. Khattatov, and J. C. Gille (2002), Constraining tropospheric ozone column through data assimilation, *J. Geophys. Res.*, *107*(D22), 4651–4676, doi: 10.1029/2001JD001249.

Lamsal, L. N., R. V. Martin, M. Steinbacher, E. A. Celarier, E. Bucsela, E. J. Dunlea, and J. Pinto (2008), Ground-level nitrogen dioxide concentrations inferred from the satellite-borne Ozone Monitoring Instrument, *J. Geophys. Res.*, *113*, D16308, doi:10.1029/2007JD009235.

Lamsal, L. N., R. V. Martin, A. van Donkelaar, E. A. Celarier, R. K. Boersma, R. Dirksen, C. Luo, and Y. Wang (2010), Indirect validation of tropospheric nitrogen dioxide retrieved from the OMI satellite instrument: insight into the seasonal variation of nitrogen oxides at northern midlatitudes, *J. Geophys. Res.*, *115*, D05302, doi:10.1029/2009JD013351.

Langford, A. O., J. Brioude, O. R. Cooper, C. J. Senff, R. J. Alvarez, II, R. M. Hardesty, B. J. Johnson, and S. J. Oltmans (2012), Stratospheric influence on surface ozone in the Los Angeles area during late spring and early summer of 2010, *J. Geophys. Res.*, *117*, D00V06, doi:10.1029/2011JD016766.

Law, K. S., and A. Stohl (2007), Arctic Air Pollution: Origins and Impacts, *Science*, *315*, 1537–1540.

Lay, E. H., R. H. Holzworth, C. J. Rodger, J. N. Thomas, O. Pinto, Jr., and R. L. Dowden (2004), WWLLN global lightning detection system: Regional validation study in Brazil, *Geophys. Res. Lett.*, *31*, L03102, doi:10.1029/2003GL018882.

Lefohn, A. S., D. Shadwick, and S. J. Oltmans (2010), Characterizing changes in surface ozone levels in metropolitan and rural areas in the United States for 1980-2008 and 1994-2008, *Atmos. Environ.*, *44*, 5199–5210.

Lelieveld, J., and F. J. Dentener (2000), What controls tropospheric ozone?, *J. Geophys. Res.*, *105*(D23), 3531–3552.

Lelieveld, J., et al. (2008), Atmospheric oxidation capacity sustained by a tropical forest, *Nature*, *452*, 737–740, doi:10.1038/nature06870.

Levy, H., II, W. J. Moxim, A. A. Klonecki, and P. S. Kasibhatla (1999), Simulated tropospheric NO_x: Its evaluation, global distribution and individual source contributions, *J. Geophys. Res.*, *104*(D21), 26,279–26,306.

Liang, Q., A. R. Douglass, B. N. Duncan, R. S. Stolarski, and J. C. Witte (2009), The governing processes and timescales of stratosphere-to-troposphere transport and its contribution to ozone in the Arctic troposphere, *Atmos. Chem. Phys.*, *9*, 3011–3025.

Liang, Q., et al. (2011), Reactive nitrogen, ozone and ozone production in the Arctic troposphere and the impact of stratosphere-troposphere exchange, *Atmos. Chem. Phys.*, *11*, 13,181–13,199.

Lin, J.-T. (2012), Satellite constraint for emissions of nitrogen oxides from anthropogenic, lightning and soil sources over East China on a high-resolution grid, *Atmos. Chem. Phys.*, *12*, 2881–2898.

Lin, J.-T., and M. B. McElroy (2010), Impacts of boundary layer mixing on pollutant vertical profiles in the lower troposphere: Implications to satellite remote sensing, *Atmos. Environ.*, *44*, 1726–1739.

Lin, J.-T., D. Youn, X.-Z. Liang, and D. J. Wuebbles (2008), Global model simulation of summertime U.S. ozone diurnal cycle and its sensitivity to PBL mixing, spatial resolution, and emissions, *Atmos. Environ.*, *42*, 8470–8483.

Lin, J.-T., M. B. McElroy, and K. F. Boersma (2010), Constraint of anthropogenic NO_x emissions in China from different sectors: a new methodology using multiple satellite retrievals, *Atmos. Chem. Phys.*, *10*, 63–78.

Lin, S.-J., and R. B. Rood (1996), Multidimensional flux form semi-Lagrangian transport schemes, *Mon. Wea. Rev.*, *124*, 2046–2070.

Logan, J. A. (1999), An analysis of ozonesonde data for the troposphere: Recommendations for testing 3-D models and development of a gridded climatology for tropospheric ozone, *J. Geophys. Res.*, *104*(D13), 16,115–16,149.

Logan, J. A., et al. (2012), Changes in ozone over Europe: Analysis of ozone measurements from sondes, regular aircraft (MOZAIC) and alpine surface sites, *J. Geophys. Res.*, *117*, D09301, doi:10.1029/2011JD016952.

Mao, H., M. Chen, J. D. Hegarty, R. W. Talbot, J. P. Koermer, A. M. Thompson, and M. A. Avery (2010), A comprehensive evaluation of seasonal simulations of ozone in the northeastern US during summers of 2001-2005, *Atmos. Chem. Phys.*, *10*, 9–27.

Mao, J., et al. (2013), Ozone and organic nitrates over the eastern United States: Sensitivity to isoprene chemistry, *J. Geophys. Res.*, *118*(16), doi:10.1002/jgrd.50817.

Martin, R. V. (2008), Satellite remote sensing of surface air quality, *Atmos. Environ.*, *42*, 7823–7843.

Martin, R. V., et al. (2002a), An improved retrieval of tropospheric nitrogen dioxide from GOME, *J. Geophys. Res.*, *107*(D20), 4437–4457, doi:10.1029/2001JD001027.

Martin, R. V., et al. (2002b), Interpretation of TOMS observations of tropical tropospheric ozone with a global model and in-situ observations, *J. Geophys. Res.*, *107*(D18), 4351–4377, doi:10.1029/2001JD001480.

Martin, R. V., D. J. Jacob, K. V. Chance, T. P. Kurosu, P. I. Palmer, and M. J. Evans (2003a), Global inventory of nitrogen oxide emissions constrained by space-based observations of NO_2 columns, *J. Geophys. Res.*, *108*(D17), 4537–4552, doi:10.1029/2003JD003453.

Martin, R. V., D. J. Jacob, R. M. Yantosca, M. Chin, and P. Ginoux (2003b), Global and Regional Decreases in Tropospheric Oxidants from Photochemical Effects of Aerosols, *J. Geophys. Res.*, *108*(D3), 4097–4113, doi:10.1029/2002JD002622.

Martin, R. V., B. Sauvage, I. Folkins, C. E. Sioris, C. Boone, P. Bernath, and J. Ziemke (2007), Space-based constraints on the production of nitric oxide by lightning, *J. Geophys. Res.*, *112*, D09309, doi:10.1029/2006JD007831.

Martins, D. K., R. M. Stauffer, A. M. Thompson, T. N. Knepp, and M. Pippin (2012), Surface ozone at a coastal suburban site in 2009 and 2010: Relationship to chemical and meteorological processes, *J. Geophys. Res.*, *117*, D05306, doi:10.1029/2011JD016828.

McLinden, C. A., S. C. Olsen, B. J. Hannegan, O. Wild, M. J. Prather, and J. Sundet (2000), Stratospheric Ozone in 3-D Models: A simple chemistry and the cross-tropopause flux, *J. Geophys. Res.*, *105*(D11), 14,653–14,665.

Mebust, A. K., A. R. Russell, R. C. Hudman, L. C. Valin, and R. C. Cohen (2011), Characterization of wildfire NO_x emissions using MODIS fire radiative power and OMI tropospheric NO_2 columns, *Atmos. Chem. Phys.*, *11*, 5839–5851.

Ménard, R., S. E. Cohn, L.-P. Chang, and P. M. Lyster (2000), Assimilation of stratospheric chemical tracer observations using a Kalman Filter. Part I: Formulation, *Mon. Weather Rev.*, *128*, 2654–2671.

Menut, L., R. Vautard, M. Beekmann, and C. Honore (2000), Sensitivity of photochemical pollution using the adjoint of a simplified chemistry-transport model, *J. Geophys. Res.*, *105*(D12), 15,379–15,402.

Meyers, T. P., P. L. Finkelstein, J. Clarke, T. G. Ellestad, and P. F. Sims (1998), A multilayer model for inferring dry deposition using standard meteorological measurements, *J. Geophys. Res.*, *103*(D17), 22,645–22,661.

Mickley, L. J., D. J. Jacob, B. D. Field, and D. Rind (2004), Climate response to the increase in tropospheric ozone since preindustrial times: A comparison between ozone and equivalent CO_2 forcings, *J. Geophys. Res.*, *109*, D05106, doi: 10.1029/2003JD003653.

Millet, D. B., et al. (2006), Formaldehyde distribution over North America: Implications for satellite retrievals of formaldehyde columns and isoprene emissions, *J. Geophys. Res.*, *111*, D24S02, doi:10.1029/2005JD006853.

Millet, D. B., D. J. Jacob, K. F. Boersma, T.-M. Fu, T. P. Kurosu, K. Chance, C. L. Heald, and A. Guenther (2008), Spatial distribution of isoprene emissions from North America derived from formaldehyde column measurements by the OMI satellite sensor, *J. Geophys. Res.*, *113*, D02307, doi:10.1029/2007JD008950.

Millet, D. B., et al. (2010), Global atmospheric budget of acetaldehyde: 3-D model analysis and constraints from in-situ and satellite observations, *Atmos. Chem. Phys.*, *10*, 3405–3425.

Miyazaki, K., H. J. Eskes, and K. Sudo (2012), Global NO_x emission estimates derived from an assimilation of OMI tropospheric NO_2 columns, *Atmos. Chem. Phys.*, *12*, 2263–2288.

Monks, P. S. (2000), A review of the observations and origins of the spring ozone maximum, *Atmos. Environ.*, *34*, 3545–3561.

Moorthi, S., and M. J. Suarez (1992), Relaxed Arakawa-Schubert: A parameterization of moist convection for general circulation models, *Mon. Wea. Rev.*, *120*, 978–1002.

Moxim, W. J., H. Levy, II, and P. S. Kasibhatla (1996), Simulated global tropospheric PAN: Its transport and impact on NO_x, *J. Geophys. Res.*, *101*(D7), 12,621–12,638.

Murray, L. T., D. J. Jacob, J. A. Logan, R. C. Hudman, and W. J. Koshak (2012), Optimized regional and interannual variability of lightning in a global chemical transport model constrained by LIS/OTD satellite data, *J. Geophys. Res.*, *117*, D20307, doi:10.1029/2012JD017934.

Nag, A., et al. (2011), Evaluation of U.S. National Lightning Detection Network performance characteristics using rocket-triggered lightning data acquired in 2004-2009, *J. Geophys. Res.*, *116*, D02123, doi:10.1029/2010JD014929.

Nassar, R., et al. (2008), Validation of Tropospheric Emission Spectrometer (TES) nadir ozone profiles using ozonesondes measurements, *J. Geophys. Res.*, *113*, D15S17, doi: 10.1029/2007JD008819.

Olivier, J. G. J., and J. J. M. Berdowski (2001), Global emissions sources and sinks, in *The Climate System*, edited by J. Berdowski, R. Guicherit, and B. J. Heij, pp. 33–77, Swets & Zeitlinger Publishers, Lisse, The Netherlands.

Oltmans, S. J., et al. (2006), Long-term changes in tropospheric ozone, *Atmos. Environ.*, *40*, 3156–3173.

Ordóñez, C., D. Brunner, J. Staehelin, P. Hadjinicolaou, J. A. Pyle, M. Jonas, H. Wernli, and A. S. H. Prévôt (2007), Strong influence of lowermost stratospheric ozone on lower tropospheric background ozone changes over Europe, *Geophys. Res. Lett.*, *34*, L07805, doi:10.1029/2006GL029113.

Osborn, T. J. (2006), Recent variations in the winter North Atlantic Oscillation: the roles of internal variability and greenhouse gas forcing, *Weather*, *61*, 353–355.

Ott, L. E., K. E. Pickering, G. L. Stenchikov, H. Huntrieser, and U. Schumann (2007), Effects of lightning NO_x production during the 21 July European Lightning Nitrogen Oxides Project storm studied with a three-dimensional cloud-scale chemical transport model, *J. Geophys. Res.*, *112*, D05307, doi:10.1029/2006JD007365.

Ott, L. E., K. E. Pickering, G. L. Stenchikov, D. J. Allen, A. J. DeCaria, B. Ridley, R.-F. Lin, S. Lang, and W.-K. Tao (2010), Production of lightning NO_x and its vertical distribution calculated from three-dimensional cloud-scale chemical transport model simulations, *J. Geophys. Res.*, *115*, D04301, doi:10.1029/2009JD011880.

Pak, B. C., and M. J. Prather (2001), CO_2 source inversions using satellite observations of the upper troposphere, *Geophys. Res. Lett.*, *28 (24)*, 4571–4574.

Palmer, P. I., D. J. Jacob, A. M. Fiore, R. V. Martin, K. Chance, and T. P. Kurosu (2003), Mapping isoprene emissions over North America using formaldehyde column observations from space, *J. Geophys. Res.*, *108*(D6), 4180–4205, doi:10.1029/2002JD002153.

Park, R. J., D. J. Jacob, B. D. Field, and R. M. Yantosca (2004), Natural and transboundary pollution influences on sulfate-nitrate-ammonium aerosols in the United States: Implications for policy, *J. Geophys. Res.*, *109*, D15204, doi:10.1029/2003JD004473.

Parrington, M., D. B. A. Jones, K. W. Bowman, L. W. Horowitz, A. M. Thompson, D. W. Tarasick, and J. C. Witte (2008), Estimating the summertime tropospheric ozone distribution over North America through assimilation of observations from the Tropospheric Emission Spectrometer, *J. Geophys. Res.*, *113*, D18307, doi:10.1029/2007JD009341.

Parrington, M., et al. (2009), Impact of the assimilation of ozone from the Tropospheric Emission Spectrometer on surface ozone across North America, *Geophys. Res. Lett.*, *36*, L04802, doi:10.1029/2008GL036935.

Parrington, M., D. B. A. Jones, T. W. Walker, K. W. Bowman, L. Lamsal, R. V. Martin, and D. B. Millet (2013), Evaluating uncertainties in modelled surface ozone abundances across North America through exploitation of satellite datasets, *in preparation*.

Paulot, F., J. D. Crounse, H. G. Kjaergaard, J. H. Kroll, J. H. Seinfeld, and P. O. Wennberg (2009), Isoprene photooxidation: new insights into the production of acids and organic nitrates, *Atmos. Chem. Phys.*, *9*, 1479–1501.

Paulot, F., D. K. Henze, and P. O. Wennberg (2012), Impact of the isoprene photochemical cascade on tropical ozone, *Atmos. Chem. Phys.*, *12*, 1307–1325.

Peeters, J., T. L. Nguyen, and L. Vereecken (2009), HO_x radical regeneration in the oxidation of isoprene, *Physical Chemistry Chemical Physics*, *11*, 5935–5939.

Pfister, G. G., L. K. Emmons, P. G. Hess, J.-F. Lamarque, A. M. Thompson, and J. E. Yorks (2008), Analysis of the Summer 2004 ozone budget over the United States using Intercontinental Transport Experiment Ozonesonde Network Study (IONS) observations and Model of Ozone and Related Tracers (MOZART-4) simulations, *J. Geophys. Res.*, *113*, D23306, doi:10.1029/2008JD010190.

Pfister, G. G., et al. (2011), Characterizing summertime chemical boundary conditions for airmasses entering the US West Coast, *Atmos. Chem. Phys.*, *11*, 1769–1790.

Pickering, K. E., Y. Wang, W.-K. Tao, C. Price, and J.-F. Müller (1998), Vertical distributions of lightning NO_x for use in regional and global chemical transport models, *J. Geophys. Res.*, *103*(D23), 31,203–31,216.

Pour-Biazar, A., M. Khan, L. Wang, Y.-H. Park, M. Newchurch, R. T. McNider, X. Liu, D. W. Byun, and R. Cameron (2011), Utilization of satellite observation of ozone and aerosols in providing initial and boundary condition for regional air quality studies, *J. Geophys. Res.*, *116*, D18309, doi:10.1029/2010JD015200.

Price, C., and D. Rind (1992), A simple lightning parametrization for calculating global lightning distributions, *J. Geophys. Res.*, *97*(D9), 9919–9933.

Price, C., and D. Rind (1994), Possible implications of global climate change on global lightning distributions and frequencies, *J. Geophys. Res.*, *99*(D5), 10,823–10,831.

Quinn, P. K., G. Shaw, E. Andrews, E. G. Dutton, T. Ruoho-Airola, and S. L. Gong (2007), Arctic haze: current trends and knowledge gaps, *Tellus B*, *59B*, 99–114.

Quinn, P. K., et al. (2008), Short-lived pollutants in the Arctic: their climate impact and possible mitigation strategies, *Atmos. Chem. Phys.*, *8*, 1723–1735.

Reidmiller, D. R., et al. (2009), The influence of foreign vs. North American emissions on surface ozone in the US, *Atmos. Chem. Phys.*, *9*, 5027–5042.

Rex, M., et al. (1998), In-situ measurements of stratospheric ozone depletion rates in the Arctic winter 1991/92: A Lagrangian approach, *J. Geophys. Res.*, *103*(D5), 5843–5853.

Richards, N. A. D., G. B. Osterman, E. V. Browell, J. W. Hair, M. A. Avery, and Q. Li (2008), Validation of Tropospheric Emission Spectrometer ozone profiles with aircraft observations during the Intercontinental Chemical Transport Experiment-B, *J. Geophys. Res.*, *113*, D16S29, doi:10.1029/2007JD008815.

Richter, A., J. P. Burrows, H. Nüß, C. Granier, and U. Niemeier (2005), Increase in tropospheric nitrogen dioxide over China observed from space, *Nature*, *437*, 129–132.

Rienecker, M., et al. (2008), File Specification for GEOS-5 DAS Gridded Output, *Tech. rep.*, Global Modeling and Assimilation Office, GMAO-1001v6.4.

Rodgers, C. D. (2000), *Inverse Methods for Atmospheric Sounding*, World Scientific Publishing, Singapore.

Rotman, D. A., et al. (2004), IMPACT, the LLNL 3-D global atmospheric chemical transport model for the combined troposphere and stratosphere: Model description and analysis of ozone and other trace gases, *J. Geophys. Res.*, *109*, D04303, doi:10.1029/2002JD003155.

Sander, S. P., et al. (2011), Chemical Kinetics and Photochemical Data for Use in Atmospheric Studies, Evaluation No. 17, *Tech. rep.*, Jet Propulsion Laboratory, Pasadena, CA, jPL Publication 10-6.

Sandu, A., D. N. Daescu, and G. R. Carmichael (2003), Direct and Adjoint Sensitivity Analysis of Chemical Kinetic Systems with KPP: I - Theory and Software Tools, *Atmos. Environ.*, *37*, 5083–5096.

Sandu, A., D. N. Daescu, G. R. Carmichael, and T. Chai (2005), Adjoint sensitivity analysis of regional air quality models, *J. Computat. Phys.*, *204*, 222–252.

Sauvage, B., R. V. Martin, A. van Donkelaar, and J. R. Ziemke (2007), Quantification of the factors controlling tropical tropospheric ozone and the South Atlantic maximum, *J. Geophys. Res.*, *112*, D11309, doi:10.1029/2006JD008008.

Schmidt, H., and D. Martin (2003), Adjoint sensitivity of episodic ozone in the Paris area to emissions on the continental scale, *J. Geophys. Res.*, *108*(D17), 3561–3577, doi:10.1029/2001JD001583.

Schumann, U., and H. Huntrieser (2007), The global lightning induced nitrous oxides source, *Atmos. Chem. Phys.*, *7*, 3823–3907.

Schwede, D., L. Zhang, R. Vet, and G. Lear (2011), An intercomparison of the deposition models used in the CASTNET and CAPMoN networks, *Atmos. Environ.*, *45*, 1337–1345.

Segers, A. J., H. J. Eskes, R. J. van der A, R. F. van Oss, and P. F. J. van Velthoven (2005), Assimilation of GOME ozone profiles and a global chemistry-transport mode, using a Kalman Filter with anisotropic covariance, *Quart. J. Roy. Meteorol. Soc.*, *131*, 477–502.

Shindell, D. T., G. Faluvegi, and N. Bell (2003), Preindustrial-to-present-day radiative forcing by tropospheric ozone from improved simulations with the GISS chemistry-climate GCM, *Atmos. Chem. Phys.*, *3*, 1675–1702.

Shindell, D. T., et al. (2008), A multi-model assessment of pollution transport to the Arctic, *Atmos. Chem. Phys.*, *8*, 5353–5372.

Sickles, J. E., II., and D. S. Shadwick (2002), Precision of atmospheric dry deposition data from the Clean Air Status and Trends Network, *Atmos. Environ.*, *36*, 5671–5686.

Simpson, D., et al. (1999), Inventorying emissions from nature in Europe, *J. Geophys. Res.*, *104*(D7), 8113–8152.

Singh, H. B. (1987), Reactive nitrogen in the troposphere - chemistry and transport of NO_x and PAN, *Envir. Sci. Technol.*, *21*, 320–327.

Singh, H. B., D. Herlth, D. O'Hara, K. Zahnle, J. D. Bradshaw, S. T. Sandholm, R. Talbot, P. J. Crutzen, and M. Kanakidou (1992), Relationship of Peroxyacetyl Nitrate to Active and Total Odd Nitrogen at Northern High Latitudes: Influence of Reservoir Species on NO_x and O_3, *J. Geophys. Res.*, *97*(D15), 16,523–16,530.

Singh, K., A. Sandu, K. W. Bowman, M. Parrington, D. B. A. Jones, and M. Lee (2011), Ozone data assimilation with GEOS-Chem: a comparison between 3-D-Var, 4-D-Var, and suboptimal Kalman filter approaches, *Atmos. Chem. Phys. Disc.*, *11*, 22,247–22,300.

Smit, H. G. J., et al. (2007), Assessment of the performance of ECC-ozonesondes under quasi-flight conditions in the environmental simulation chamber: Insights from the Jülich Ozone Sonde Intercomparison Experiment (JOSIE), *J. Geophys. Res.*, *112*, D19306, doi:10.1029/2006JD007308.

Solomon, S., et al. (Eds.) (2007), *Climate Change 2007: The Physical Science Basis. Intergovernmental Panel on Climate Change*, Cambridge University Press, New York.

Stajner, I., et al. (2008), Assimilated ozone from EOS-Aura: Evaluation of the tropopause region and tropospheric columns, *J. Geophys. Res.*, *113*, D16S32, doi: 10.1029/2007JD008863.

Staudt, A. C., et al. (2003), Sources and chemistry of nitrogen oxides over the tropical Pacific, *J. Geophys. Res.*, *108*(D2), 8239–8266, doi:10.1029/2002JD002139.

Stavrakou, T., and J.-F. Müller (2006), Grid-based versus big region approach for inverting CO emissions using Measurement of Pollution in the Troposphere (MOPITT) data, *J. Geophys. Res.*, *111*, D15304, doi:10.1029/2005JD006896.

Stavrakou, T., J.-F. Müller, K. F. Boersma, I. De Smedt, and R. J. van der A (2008), Assessing the distribution and growth rates of NO_x emission sources by inverting a 10-year record of NO_2 satellite columns, *Geophys. Res. Lett.*, *35*, L10801, doi:10.1029/2008GL033521.

Stavrakou, T., J.-F. Müller, K. F. Boersma, R. J. van der A, J. Kurokawa, T. Ohara, and Q. Zhang (2013), Key chemical NO_x sink uncertainties and how they influence top-down emissions of nitrogen oxides, *Atmos. Chem. Phys.*, *13*, 9057–9082.

Steinbacher, M., C. Zellweger, B. Schwarzenbach, S. Bugmann, B. Buchmann, C. Ordóñez, A. S. H. Prévôt, and C. Hueglin (2007), Nitrogen oxide measurements at rural sites in Switzerland: Bias of conventional measurement techniques, *J. Geophys. Res.*, *112*, D11307, doi:10.1029/2006JD007971.

Stevenson, D. S., et al. (2004), Radiative forcing from aircraft NO_x emissions: mechanisms and seasonal dependance, *J. Geophys. Res.*, *109*, D17307, doi:10.1029/2004JD004759.

Stocks, B. J., et al. (1998), Climate change and forest fire potention in Russian and Canadian boreal forests, *Climatic Change*, *38*(1), 1–13.

Stohl, A. (2001), A 1-year Lagrangian "climatology" of airstreams in the Northern Hemisphere troposphere and lowermost stratosphere, *J. Geophys. Res.*, *106*(D7), 7263–7279.

Stohl, A. (2006), Characteristics of atmospheric transport into the Arctic troposphere, *J. Geophys. Res.*, *111*, D11306, doi:10.1029/2005JD006888.

Stohl, A., et al. (2007), Arctic smoke - record high air pollution levels in the European Arctic due to agricultural fires in Eastern Europe in spring 2006, *Atmos. Chem. Phys.*, *7*, 511–534.

Streets, D. G., et al. (2003), An inventory of gaseous and primary aerosol emissions in Asia in the year 2000, *J. Geophys. Res.*, *108*(D21), 8809–8824, doi:10.1029/2002JD003093.

Streets, D. G., Q. Zhang, L. Wang, K. He, J. Hao, Y. Wu, Y. Tang, and G. R. Carmichael (2006), Revisiting China's CO emissions after TRACE-P: Synthesis of inventories, atmospheric modeling, and observations, *J. Geophys. Res.*, *111*, D14306, doi:10.1029/2006JD007118.

Sudo, K., M. Takahashi, and H. Akimoto (2002), CHASER: A global chemical model of the troposphere 2. Model results and evaluation, *J. Geophys. Res.*, *107*(D21), 4586–4624.

Talbot, R. W., et al. (1994), Summertime distribution and relations of reactive odd nitrogen species and NO_y in the troposphere over Canada, *J. Geophys. Res.*, *99*(D1), 1863–1885.

Tang, X., J. Zhu, Z. F. Wang, and A. Gbaguidi (2011), Improvement of ozone forecast over Beijing based on ensemble Kalman filter with simultaneous adjustment of initial conditions and emissions, *Atmos. Chem. Phys.*, *11*, 12,901–12,916.

Tang, Y., et al. (2007), Influence of lateral and top boundary conditions on regional air quality prediction: A multiscale study coupling regional and global chemical transport models, *J. Geophys. Res.*, *112*, D10S18, doi:10.1029/2006JD007515.

Tang, Y., et al. (2009), The impact of chemical lateral boundary conditions on CMAQ predictions of tropospheric ozone over the continental United States, *Environ. Fluid Mech.*, *9*, 43–58.

Taraborrelli, D., M. G. Lawrence, T. M. Butler, R. Sander, and J. Lelieveld (2009), Mainz Isoprene Mechanism 2 (MIM2): an isoprene oxidation mechanism for regional and global atmospheric modelling, *Atmos. Chem. Phys.*, *9*, 2751–2777.

Tarasick, D. W., and R. Slater (2008), Ozone in the Troposphere: Measurements, Climatology, Budget, and Trends, *Atmosphere Ocean*, *46*(1), 93–115.

Tarasick, D. W., V. E. Fioletov, D. I. Wardle, J. B. Kerr, and J. Davies (2005), Changes in the vertical distribution of ozone over Canada from ozonesondes: 1980-2001, *J. Geophys. Res.*, *110*, D02304, doi:10.1029/2004JD004643.

Terao, Y., J. A. Logan, A. R. Douglass, and R. S. Stolarski (2008), Contribution of stratospheric ozone to the interannual variability of tropospheric ozone in the northern extratropics, *J. Geophys. Res.*, *113*, D18309, doi:10.1029/2008JD009854.

Thomas, J. L., J. Stutz, B. Lefer, L. G. Huey, K. Toyota, J. E. Dibb, and R. von Glasow (2011), Modeling chemistry in and above snow at Summit, Greenland - Part 1: Model description and results, *Atmos. Chem. Phys.*, *11*, 4899–4914.

Thompson, A. M., et al. (2003), Southern Hemisphere Additional Ozonesondes (SHADOZ) 1998-2000 tropical ozone climatology: 1. Comparison with Total Ozone Mapping Spectrometer (TOMS) and ground-based measurements, *J. Geophys. Res.*, *108*(D2), 8238–8265, doi:10.1029/2001JD000967.

Thompson, A. M., et al. (2007), Intercontinental Chemical Transport Experiment Ozonesonde Network Study (IONS, 2004): 2. Tropospheric Ozone Budgets and Variability over Northeastern North America, *J. Geophys. Res.*, *112*, D12S13, doi: 10.1029/2006JD007670.

Thompson, A. M., J. E. Yorks, S. K. Miller, J. C. Witte, K. M. Dougherty, G. A. Morris, D. Baumgardner, L. Ladino, and B. Rappenglück (2008), Tropospheric ozone sources and wave activity over Mexico City and Houston during Milagro/Intercontinental Transport Experiment (INTEX-B) Ozonesonde Network Study, 2006 (IONS-06), *Atmos. Chem. Phys.*, *8*, 5113–5126.

Thornton, J. A., L. Jaeglé, and V. F. McNeill (2008), Assessing known pathways for HO_2 loss in aqueous atmospheric aerosols: Regional and global impacts on tropospheric oxidants, *J. Geophys. Res.*, *113*, D05303, doi:10.1029/2007JD009236.

Thouret, V. A., A. Marenco, J. A. Logan, and P. Nédélec (1998), Comparisons of ozone measurements from the MOZAIC airborne program and the ozone sounding network at eight stations, *J. Geophys. Res.*, *103*(D19), 25,695–25,720.

Thurston, G. D., and K. Ito (2001), Epidemiological studies of acute ozone exposures and mortality, *Journal of Exposure Analysis and Environmental Epidemiology*, *11*, 286–294.

Tian, W., M. P. Chipperfield, D. S. Stevenson, R. Damoah, S. Dhomse, A. Dudhia, H. Pumphrey, and P. Bernath (2010), Effects of stratosphere-troposphere chemistry coupling on tropospheric ozone, *J. Geophys. Res.*, *115*, D00M04, doi:10.1029/2009JD013515.

Tilmes, S., et al. (2010), An aircraft-based upper troposphere lower stratosphere O_3, CO, and H_2O climatology for the Northern Hemisphere, *J. Geophys. Res.*, *115*, D14303, doi: 10.1029/2009JD012731.

Tørseth, K., W. Aas, K. Breivik, A. M. Fjæraa, M. Fiebig, A. G. Hjellbrekke, C. Lund Myhre, S. Solberg, and K. E. Yttri (2012), Introduction to the European Monitoring and Evaluation Programme (EMEP) and observed atmospheric composition change during 1972-2009, *Atmos. Chem. Phys.*, *12*, 5447–5481.

Tuazon, E. C., W. P. L. Carter, and R. Atkinson (1991), Thermal decomposition of peroxyacetyl nitrate and reactions of acetyl peroxy radicals with nitric oxide and nitrogen dioxide over the temperature range 283-313 K, *J. Phys. Chem*, *95*(6), 2434–2437.

U.S. Environmental Protection Agency (2012), Our Nation's Air: Status and Trends through 2010, *Tech. rep.*, Research Triangle Park, North Carolina, EPA-454/R-12-001.

van Aardenne, J. A., F. J. Dentener, J. G. J. Olivier, C. G. M. Klein Goldewijk, and J. Lelieveld (2001), A $1^\circ \times 1^\circ$ resolution data set of historical anthropogenic trace gas emissions for the period 1890-1990, *Global Biogeochem. Cycles*, *15 (4)*, 909–928.

van der Werf, G. R., J. T. Randerson, L. Giglio, G. J. Collatz, P. S. Kasibhatla, and A. F. A. Jr. (2006), Interannual variability in global biomass burning emissions from 1997 to 2004, *Atmos. Chem. Phys.*, *6*, 3423–3441.

van der Werf, G. R., et al. (2010), Global fire emissions and the contribution of deforestation, savanna, forest, agricultural, and peat fires (1997-2009), *Atmos. Chem. Phys.*, *10*, 11,707–11,735.

van Donkelaar, A., et al. (2008), Analysis of aircraft and satellite measurements from the Intercontinental Chemical Transport Experiment (INTEX-B) to quantify long-range transport of East Asian sulfur to Canada, *Atmos. Chem. Phys.*, *8*, 2999–3014.

Vautard, R., M. Beekmann, and L. Menut (2000), Applications of adjoint modelling in atmospheric chemistry: sensitivity and inverse modelling, *Environ. Modell. Software*, *15*, 703–709.

Vestreng, V., and H. Klein (2002), Emission data report to UN-ECE/EMEP: quality assurance and trend analysis and presentation of WebDab, *Tech. rep.*, Norwegian Meteorological Institute, Oslo, Norway, MSC-W Status Report EMEP/MSC-W Note 1/02.

Vingarzan, R. (2004), A review of surface ozone background levels and trends, *Atmos. Environ.*, *38*, 3431–3442.

Von Kuhlmann, R., M. G. Lawrence, P. J. Crytzen, and P. J. Rasch (2003), A model for studies of tropospheric ozone and nonmethane hydrocarbons: model description and ozone results, *J. Geophys. Res.*, *108*(D9), 4294, doi:10.1029/2002JD002893.

Voulgarakis, A., N. H. Savage, O. Wild, P. Braesicke, P. J. Young, G. D. Carver, and J. A. Pyle (2010), Interannual variability of tropospheric composition: the influence of changes in emissions, meteorology and clouds, *Atmos. Chem. Phys.*, *10*, 2491–2506.

Walker, K. A., C. E. Randall, C. R. Trepte, and C. D. Boone (2005), Initial validation comparisons for the Atmospheric Chemistry Experiment (ACE-FTS), *Geophys. Res. Lett.*, *32*, L16S04, doi:10.1029/2005GL022388.

Walker, K. A., et al. (2009), Solar Occultation for Atmospheric Research (SOAR) Mission Concept, *Tech. rep.*, Canadian Space Agency, SOAR-PT-003-UoT-9F028-070111.

Walker, T. W., et al. (2010), Trans-Pacific transport of reactive nitrogen and ozone to Canada during spring, *Atmos. Chem. Phys.*, *10*, 8353–8372.

Walker, T. W., et al. (2012), Impacts of midlatitude precursor emissions and local photochemistry on ozone abundances in the Arctic, *J. Geophys. Res.*, *117*, D01305, doi:10.1029/2011JD016370.

Wang, S. W., Q. Zhang, D. G. Streets, K. B. He, R. V. Martin, L. N. Lamsal, D. Chen, Y. Lei, and Z. Lu (2012), Growth in NO_x emissions from power plants in China: bottom-up estimates and satellite observations, *Atmos. Chem. Phys.*, *12*, 4429–4447.

Wang, Y., et al. (2003), Springtime photochemistry at northern mid and high latitudes, *J. Geophys. Res.*, *108*(D4), 8358–8384, doi:10.1029/2002JD002227.

Wang, Y. H., D. J. Jacob, and J. A. Logan (1998), Global simulation of tropospheric O_x-NO_x-hydrocarbon chemistry 1. Model formulation, *J. Geophys. Res.*, *103*(D9), 10,713–10,725.

Wang, Y. X., M. B. McElroy, D. J. Jacob, and R. M. Yantosca (2004), A nested grid formulation for chemical transport over Asia: applications to CO, *J. Geophys. Res.*, *109*, D22307, doi:10.1029/2004JD005237.

Weaver, C. P., et al. (2009), A preliminary synthesis of modeled climate change impacts on U.S. regional ozone concentrations, *B. Am. Meteorol. Soc.*, *90*, 1843–1863.

Wesely, M. L. (1989), Parameterization of surface resistances to gaseous dry deposition in regional-scale numerical models, *Atmos. Environ.*, *23*, 1293–1304.

Wesely, M. L., and B. B. Hicks (1977), Some factors that ffect the deposition rtes of sulfur dioxide and similar gases on vegetation, *Journal of the Air Pollution Control Association*, *27*, 1110–1116.

Wesely, M. L., and B. B. Hicks (2000), A review of the current status of knowledge on dry deposition, *Atmos. Environ.*, *34*, 2261–2282.

West, J. J., S. Szopa, and D. A. Hauglustaine (2007), Human mortality effects of future concentrations of tropospheric ozone, *Comptes Rendus Geoscience*, *339*, 775–783.

Wild, O., and H. Akimoto (2001), Intercontinental transport of ozone and its precursors in a three-dimensional global CTM, *J. Geophys. Res.*, *106*(D21), 27,729–27,744.

Wild, O., P. Pochanart, and H. Akimoto (2004), Trans-Eurasian transport of ozone and its precursors, *J. Geophys. Res.*, *109*, D11302, doi:10.1029/2003JD004501.

Wolfe, G. M., et al. (2007), Influence of trans-Pacific pollution transport on acyl peroxy nitrate abundances and speciation at Mount Bachelor Observatory during INTEX-B, *Atmos. Chem. Phys.*, *7*, 5309–5325.

Wolfe, G. M., J. A. Thornton, R. L. N. Yatavelli, M. McKay, A. H. Goldstein, B. LaFranchi, K.-E. Min, and R. C. Cohen (2009), Eddy covariance fluxes of acyl peroxy nitrates (PAN, PPN, and MPAN) above a Ponderosa pine forest, *Atmos. Chem. Phys.*, *9*, 615–635.

Worden, H. M., et al. (2007), Comparisons of Tropospheric Emission Spectrometer (TES) ozone profiles to ozonesondes: Methods and initial results, *J. Geophys. Res.*, *112*, D03309, doi:10.1029/2006JD007258.

Worden, J., S. S. Kulawik, M. W. Shephard, S. A. Clough, H. Worden, K. Bowman, and A. Goldman (2004), Predicted errors of Tropospheric Emission Spectrometer nadir retrievals from spectral window selection, *J. Geophys. Res.*, *109*, D09308, doi:10.1029/2004JD004522.

Worden, J., et al. (2009), Observed vertical distribution of tropospheric ozone during the Asian summertime monsoon, *J. Geophys. Res.*, *114*, D13304, doi:10.1029/2008JD010560.

Wu, Z., et al. (2011), Evaluating the calculated dry deposition velocities of reactive nitrogen oxides and ozone from two community models over a temperate deciduous forest, *Atmos. Environ.*, *45*, 2663–2674.

Yevich, R., and J. A. Logan (2003), An assessment of biofuel use and burning of agricultural waste in the developing world, *Global Biogeochem. Cycles*, *17*(4), 1095–1136, doi:10.1029/2002GB001952.

Yienger, J. J., and H. Levy, II (1995), Empirical model of global soil-biogenic NO_x emissions, *J. Geophys. Res.*, *100*, 1447–1464.

Yoshida, S., T. Morimoto, T. Ushio, and Z. Kawasaki (2009), A fifth-power relationship for lightning activity from Tropical Rainfall Measuring Mission satellite observations, *J. Geophys. Res.*, *114*, D09104, doi:10.1029/2008JD010370.

Zel'dovich, Y. B., and Y. P. Raizer (1967), *Physics of Shock Waves and High Temperature Hydrodynamic Phenomena*, Academic, San Diego, California.

Zhang, G. J., and N. A. McFarlane (1995), Sensitivity of climate simulations to the parameterization of cumulus convection in the Canadian Climate Centre general circulation model, *Atmos. Ocean*, *33 (3)*, 407–446.

Zhang, L., J. R. Brook, and R. Vet (2002), On ozone dry deposition - with emphasis on non-stomatal uptake and wet canopies, *Atmos. Environ.*, *36*, 4787–4799.

Zhang, L., et al. (2008), Transpacific transport of ozone pollution and the effect of recent Asian emission increases on air quality in North America: an integrated analysis using satellite, aircraft, ozonesonde, and surface observations, *Atmos. Chem. Phys.*, *8*, 6117–6136.

Zhang, L., D. J. Jacob, M. Kopacz, et al. (2009), Intercontinental source attribution of ozone pollution at western US sites using an adjoint method, *Geophys. Res. Lett.*, *36*, L11810, doi:10.1029/2009GL037950.

Zhang, L., et al. (2011), Improved estimate of the policy-relevant background ozone in the United States using the GEOS-Chem global model with $1/2^\circ \times 2/3^\circ$ horizontal resolution over North America, *Atmos. Environ.*, *45*, 6769–6776.

Zhang, L., D. J. Jacob, X. Yue, N. V. Downey, D. A. Wood, and D. Blewitt (2013), Sources contributing to background surface ozone in the US Intermountain West, *Atmos. Chem. Phys. Disc.*, *13*, 25,871–25,909.

Zhang, Q., et al. (2007), NO_x emission trends for China, 1995-2004: The view from the ground and the view from space, *J. Geophys. Res.*, *112*, D22306, doi:10.1029/2007JD008684.